UC Berkeley
UC Berkeley Electronic Theses and Dissertations

Title
Optical Spectroscopy of Two Dimensional Graphene and Boron Nitride

Permalink
https://escholarship.org/uc/item/5p08d84q

Author
Ju, Long

Publication Date
2015

Peer reviewed|Thesis/dissertation

eScholarship.org Powered by the California Digital Library
University of California

Optical Spectroscopy of Two Dimensional Graphene and Boron Nitride

by

Long Ju

A dissertation submitted in partial satisfaction of the
requirements for the degree of
Doctor of Philosophy

in

Physics

in the

Graduate Division

of the

University of California, Berkeley

Committee in charge:

Professor Feng Wang, Chair
Professor Joseph W. Orenstein
Professor Xiang Zhang

Fall 2015

Optical Spectroscopy of Two Dimensional Graphene and Boron Nitride

Copyright 2015
by
Long Ju

Abstract

Optical Spectroscopy of Two Dimensional Graphene and Boron Nitride

by

Long Ju

Doctor of Philosophy in Physics

University of California, Berkeley

Professor Feng Wang, Chair

This dissertation describes the use of optical spectroscopy in studying the physical properties of two dimensional nano materials like graphene and hexagonal boron nitride. Compared to bulk materials, atomically thin two dimensional materials have a unique character that is the strong dependence of physical properties on external control. Both electronic band structure and chemical potential can be tuned in situ by electric field–which is a powerful knob in experiment. Therefore the optical study at atomic thickness scale can greatly benefit from modern micro-fabrication technique and electric control of the material properties. As will be shown in this dissertation, such control of both gemometric and physical properties enables new possibilities of optical spectroscopic measurement as well as opto-electronic studies. Other experimental techniques like electric transport and scanning tunneling microscopy and spectroscopy are also combined with optical spectroscopy to reveal the physics that is beyond the reach of each individual technique.

There are three major themes in the dissertation. The first one is focused on the study of plasmon excitation of Dirac electrons in monolayer graphene. Unlike plasmons in ordinary two dimensional electron gas, plasmons of 2D electrons as in graphene obey unusual scaling laws. We fabricate graphene micro-ribbon arrays with photolithography technique and use optical absorption spectroscopy to study its absorption spectrum. The experimental result demonstrates the extraordinarily strong light-plasmon coupling and its novel dependence on both charge doping and geometric dimensions. This work provides a first glance at the fundamental properties of graphene plasmons and forms the basis of an emerging subfield of graphene research and applications such as graphene terahertz metamaterials.

The second part describes the opto-electronic response of heterostructures composed of graphene and hexagonal boron nitride. We found that there is a charge transfer process between graphene and BN when the exposure of visible light is introduced. We show this photo-induced doping in graphene resembles the modulation doping technique in traditional semiconductor heterojunctions, where a charge doping is introduced while the high mobility

is maintained. This work reveals importance of interactions between stacked 2D materials on the overall properties and demonstrate a repeatable and convenient way of fabricating high quality graphene devices with active control of doping patterning. Along this direction, we did further STM experiment to visualize and manipulate charged defects in boron nitride with the help of graphene.

The last theme is about the interesting properties of bilayer graphene, which is to some extent more interesting than monolayer graphene due to its electric-field dependent band structures. Firstly, we visualized the stacking boundary within exfoliated bilayer graphene by near field infrared microscopy. In dual-gated field-effect-transistor devices fabricated on the boundaries, we demonstrated the existence of topologically protected one dimensional conducting channels at the boundary through electric transport measurement. The 1D boundary states also demonstrated the first graphene-based valleytronic device.

The topics we are going to talk about in this thesis are quite diversified. Just like the versatile nature of optical spectroscopy, we never limit ourself to a specific technique and do incremental things. Most of the experiments are driven by the important and interesting problems in the two dimensional materials field and we chose the right tool and conceive the right experiment to answer that question. Both pure optical methods and combinations with electric transport and STM measurements were used. I believe the flexibility of optical spectroscopy and its compatibility with other experimental techniques provide a powerful toolbox to explore many possibilities beyond the reach of a single experimental approach. And such a way of doing experiments is very much enjoyable for me.

To my parents,

Xiling Cui
and
Tongxun Ju

Contents

Contents **ii**

List of Figures **iv**

1 Introduction **1**
1.1 Basics of Monolayer graphene 1
1.2 Bandstructure of Bilayer Graphene 3
1.3 Optical Transitions in Graphene 5
1.4 Outline of the Thesis 8

2 Plasmon Excitations in Monolayer Graphene **9**
2.1 Introduction to Plasmons in Two Dimensional Systems 10
2.2 Fabrication of the Dual-Gated Graphene Micron-Ribbon Array 11
2.3 Basics of Fourier Transform Infrared Spectroscopy 13
2.4 Absorption Spectrum of Free Carriers and Plasmons of Graphene in the Far-Infrared Range 16
2.5 Tuning of Plasmon Resonance by Electrical Gating and Structure Engineering 18
2.6 Scaling Laws and Numerical Simulation of Plasmon Modes in Graphene Ribbon Array 20
2.7 Comparison to Plasmons in Other 2D Electron Gas Systems 23
2.8 Potential Applications of Graphene as Terahertz Metamaterials 25
2.9 Summary 26

3 Photo-induced Doping in Heterostructures of Graphene and Boron Nitride **27**
3.1 Physical Properties of Graphene on Hexagonal Boron Nitride 27
3.2 Fabrication of the Graphene/Boron Nitride Heterostructure 28
3.3 Experimental Observation of Photo-Induced Doping in Graphene/Boron nitride 30
3.4 Microscopic Mechanism of Photo-Induced Doping 33
3.5 Similarity to Modulation Doping Technique 37
3.6 Potential Applications of Photo-Induced Doping 37
3.7 Summary 38

4 STM Study of Defect States in Boron Nitride **40**
4.1 Basics of Scanning Tunneling Microscopy/Spectroscopy 40
4.2 Extending the Scope of STM Study 41
4.3 Imaging of Charged Defects in Boron Nitride Through Graphene 42
4.4 Determination of Charge Types of the Dot-like Defects 44
4.5 Determination of Energy Levels of the Ring-like Defects 45
4.6 Manipulation of Defect States in Boron Nitride 47
4.7 Summary 50

5 Topological Valley Transport at Bilayer Graphene Domain Walls **52**
5.1 Topologically Protected Boundary States at Electrically-Induced and Structurally-Induced Bilayer Graphene Domain Walls 53
5.2 Introduction to Near Field Infrared Nanoscopy 54
5.3 Near Field Nanoscopic Imaging of Domain Walls in Bilayer Graphene 55
5.4 Near Field Nanoscopic Imaging of Monolayer and Trilayer Graphene 56
5.5 Fabrication of Dual-gated Field-Effect-Transistor Devices on Bilayer Domain Walls 58
5.6 Electric Transport Measurement of the One Dimensional Conducting Channels at Bilayer Domain Walls 60
5.7 Temperature Dependence of Electrical Transport of AB-BA Domain Walls . 65
5.8 Topological Understanding of The 1D Boundary States at Bilayer Domain Walls 66
5.9 Summary 67

Bibliography **68**

List of Figures

1.1 Lattice structure of monolayer graphene and its first Brillouin Zone 2
1.2 Bandstructure of monolayer graphene 3
1.3 Atomic structure of AB-stacked bilayer graphene 4
1.4 Bandstructure of bilayer graphene 5
1.5 Optical transitions in monolayer graphene 7
1.6 Gate-tunable optical transitions in bilayer graphene 7

2.1 Illustration of plasmon in a ribbon of material 10
2.2 Dispersion relation of photons and plasmons 12
2.3 Experimental approaches to solve momentum mismatch between photons and plasmons 13
2.4 Topview and sideview of graphene micro-ribbon array device 14
2.5 Illustration of fourier transform spectroscopy 15
2.6 Absorption spectrum of graphene-ribbon array under parallel and perpendicular polarized light illumination 17
2.7 Mid-infrared transmission spectra of the graphene ribbon array at different gate voltages 18
2.8 Control of terahertz resonance of plasmon excitations through electrical gating . 19
2.9 Change of transmission spectra with different graphene micro-ribbon widths . . 20
2.10 Plasmon frequency with different doping and ribbon width 21
2.11 Scaling laws of graphene plasmon resonance frequency 22
2.12 Simulated transmission spectrum change of graphene plasmon for 4μm ribbon width 24
2.13 Simulated current density amplitude and phase 25

3.1 Schematic of the transfer process of graphene onto BN 29
3.2 Optical microscope image of exfoliated graphene transferred on exfoliated hBN . 31
3.3 Experimental observation of photo-induced modulation doping effect in G/BN heterostructures 32
3.4 Charge distribution in the G/BN device when light is and on 33
3.5 Dynamics of photo-induced modulation doping effect 34

3.6 Schematics of the band structure of the graphene/BN heterostructure and illustration of the photo-doping mechanism. 35
3.7 Optical absorption spectrum of defect states in h-BN 36
3.8 Transport characteristics of G/BN after photo-induced modulation doping . . . 38
3.9 Optical absorption spectrum of defect states in h-BN 39

4.1 A schematic demonstration of the structure and working principle of an STM . 42
4.2 STM topography and corresponding dI/dV map for a graphene/BN device . . . 43
4.3 dI/dV maps and spatially dependent dI/dV spectroscopy determines defect charge state 46
4.4 dI/dV maps of the ring defect at different measurement conditions 47
4.5 Ring radius R for different V_s and V_g 48
4.6 Schematic model for ring formation due to charge transfer between graphene and a defect in the top layer of BN 49
4.7 Manipulating defects in BN with an STM tip 51

5.1 Illustration of a domain wall between AB- and BA-stacked BLG domains 53
5.2 Illustration of the near-field infrared nanoscopy measurement of graphene on a SiO_2/Si substrate 55
5.3 IR nanoscopy imaging of AB-BA domain walls in exfoliated bilayer graphene . . 57
5.4 IR nanoscopy imaging of exfoliated monolayer and bilayer graphene 58
5.5 IR nanoscopy imaging of exfoliated trilayer graphene and its Raman spectrum . 59
5.6 Dual-gated field effect transistor (FET) devices on bilayer graphene with AB-BA domain walls 60
5.7 Electric transport behaviours of dual-gated FET devices on bilayer graphene with AB-BA domain walls 61
5.8 Conductance of topologically protected chiral modes at AB-BA domain walls . . 62
5.9 Electronic band structure of stacking domain walls and the valley polarized electrical current 64
5.10 Length dependence of the bilayer graphene domain wall conductance. 65
5.11 Temperature-dependent electrical transport through bulk bilayer graphene and through the AB-BA domain wall. 66

Acknowledgments

First I would like to thank my advisor Prof. Feng Wang for the key role he has played during my Ph.D. study. It is a great pleasure and honor to work with Feng, who is not only a great scientist but also an excellent educator. His ability of explaining things in a neat and clear way really re-defined my interpretation of 'understanding something'. I also benefit from Feng's broad picutre of the whole field and unique scientific taste, which allowed me to focus on the most important problems. I should also thank him for the initial decision of throwing me (as a member of an optics group) into cleanroom that not only enriched my experimental toolbox, but also shaped my way of thinking scientific problems. Together with many enlightening discussions, his support and encouragement makes this six years a wonderful experience.

I am in debt to Prof. Ron Shen for his guidance through my years in graduate school. Albeit very busy, Ron was always ready for discussions and his questions constantly pushed me to learn more and understand things better. Ron's suggestions on my career development is unique and invalueable.

I am deeply grateful to my colleages in the Wang group for their help. My collaboration with Baisong Geng in the graphene plasmonics study and Zhiwen Shi in the experiment of topological boundary states in bilayer graphene have been wonderful and fruitful experiences. Tom Tang, Sufei Shi and Huiling Han who were postdocs in the group have taught me optical and electric transport experimental techniques. Sufei also provided very helpful advices on my career development. Frank Chen, Kaihui Liu, Steve Byrnes, Jason Horng, Jonghwan Kim, Yaqing Bie, Xiaoping Hong, Bo Zeng, Chenhao Jin and Yu-Chied Wen were great labmates who were always ready for help. Special thanks goes to undergrad student Edwin Huang, Casey Nosiglia and Yinchuan Lv, who contributed a lot to sample fabrications and realizing my crazy ideas of making various heterostructure samples.

It is a fortune to be able to work with wonderful colleagues in other groups. I had long term collaboration with Jairo Velasco Jr. and Dillon Wong in Prof. Mike Crommie's group on electric transport and STM experiments. Their knowledge and expertise proved to be a great complement to mine. Our effort of combining different techniques resulted in many new possibilities in experimental studies. Qin Zhou in Prof. Zettl's group offered a lot of help during my early days in Nanolab. Considering I was the only physics guy in Nanolab, Qin's help made my life much easier.

Finally I woud like to thank staff in our department, Anne Takizawa and Anthony Vitan for their support in many non-academic aspects. Whenever I had problems that I don't know how to solve, I know that Anne will figure it out. Anthony's effort on lab construction and maintainece provided me a great environment to do research.

Chapter 1

Introduction

Most of the topics we are going to talk about in this thesis are related to graphene, which has been intensively studied by condensed matter researchers since its discovery in 2005[1][2]. It has fascinating electronic, optical and mechanical properties that attract attention from both scientific research side and engineering applications side. We will mainly focus on the optical properties of graphene in this dissertation. But before that, I will describe some basic properties of graphene in this chapter.

1.1 Basics of Monolayer graphene

Monolayer graphene has a honeycomb lattice structure that is solely composed of carbon atoms as illustrated in Fig. 1.1a. There are two inequivalent atoms in each unit cell (the enclosed area by dashed lines) and are named as A atom anb B atom. There are two primitive lattice vectors forming an angle of 60 degree. Based on these two primitive lattice vectors, one can derive the first Brillouin zone in momentum space as shown by Fig. 1b. Three of the six corners in the first Brillouin zone are connected by reciprocal wave vectors so they are equivalent and named as K point. The other three equivalent corners are named as K$'$ point.

The most interesting physics happen around K and K$'$ points. The band structure of monolayer graphene was first calculated by Wallace [3] using the tight-binding approximation, which revealed the linear dispersion relation as shown in Fig. 1.2. The highest valence band and the lowest conduction bands are degenerate at K and K$'$ points. In the neighborhood of these two points, the electronic states have a linear relation between energy and momentum. Such dispersion relation is similar to the dispersion relation of photons except for the speed of light is replaced by the Fermi velocity $v_F \sim c/300$. The linear band structure and zero bandgap also indicate that the mass of electrons is zero.

By choosing the quasi-plane wavefunctions composed of orbitals from A and B sublattices

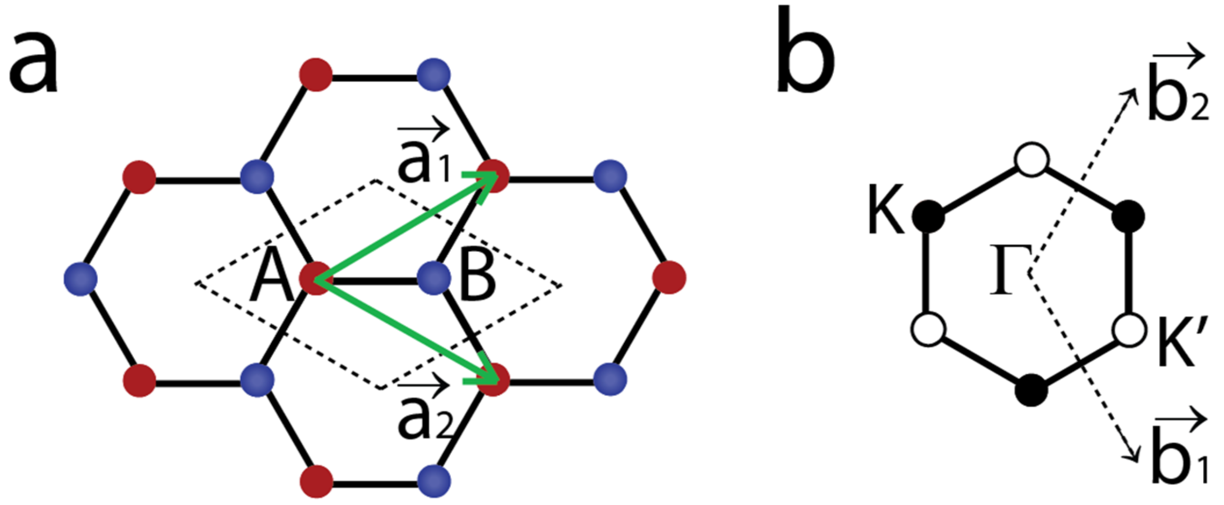

Figure 1.1: Lattice structure of monolayer graphene and its first Brillouin Zone. a, The honeycomb lattice of monolayer graphene. Red atoms are belonged to A sublattice while blue atoms are belonged to B sublattice. Green arrows represent the primitive lattice vectors. b, First Brillouin Zone of monolayer graphene. Dashed arrows represent the reciprocal wave vectors derived from the primitive lattice vectors in a. Filled and hollow dots represent the two inquivalent points at the corner of the first Brillouin Zone.

as the basis functions, one can write down the Hamiltonian as[4]

$$H = \hbar v_F \sigma \cdot \vec{p} \tag{1.1}$$

where σ is the Pauli matrices and $\vec{p}$ is the momentum operator. This Hamiltonian has the same form as the Dirac equation so electrons in graphene are also called as massless Dirac Fermions. With the same logic, K/K′ points are called Dirac points while the linear bandstructure is called Dirac cone. The eigen-wavefunction can be written as

$$\Phi_K(\mathbf{q}) = \frac{1}{\sqrt{2}} e^{i\mathbf{q}\cdot\mathbf{r}} \begin{pmatrix} e^{-i\theta_q/2} \\ \pm e^{i\theta_q/2} \end{pmatrix} \tag{1.2}$$

where θ_q is the angle between the direction of wavevector $\mathbf{q}$ and k_x, and +/- sign corresponds to conduction/valence band respectively. This two-component wavefunction has exactly the same form as the wavefunction of spin confined in the xy plane and pointing to the direction θ_q from the x-axis. Therefore this orbital degree-originated degree of freedom is called pseudo-spin. And for conduction band in K valley, this pseudo-spin direction is parallel to momentum while it is anti-parallel to momentum for the valence band. Since electrons feel the same potential at A and B sublattices, the two components in the pseudospin have

the same amplitude. Thus the pseudospin is confined in the 2D plane. However, if the inversion symmetry is broken and A, B sublattices are no longer symmetric, the wavefunction component at the higher energy site will be small than that at the lower energy site. Thus the pseudospin will develop an out-of-plane component.

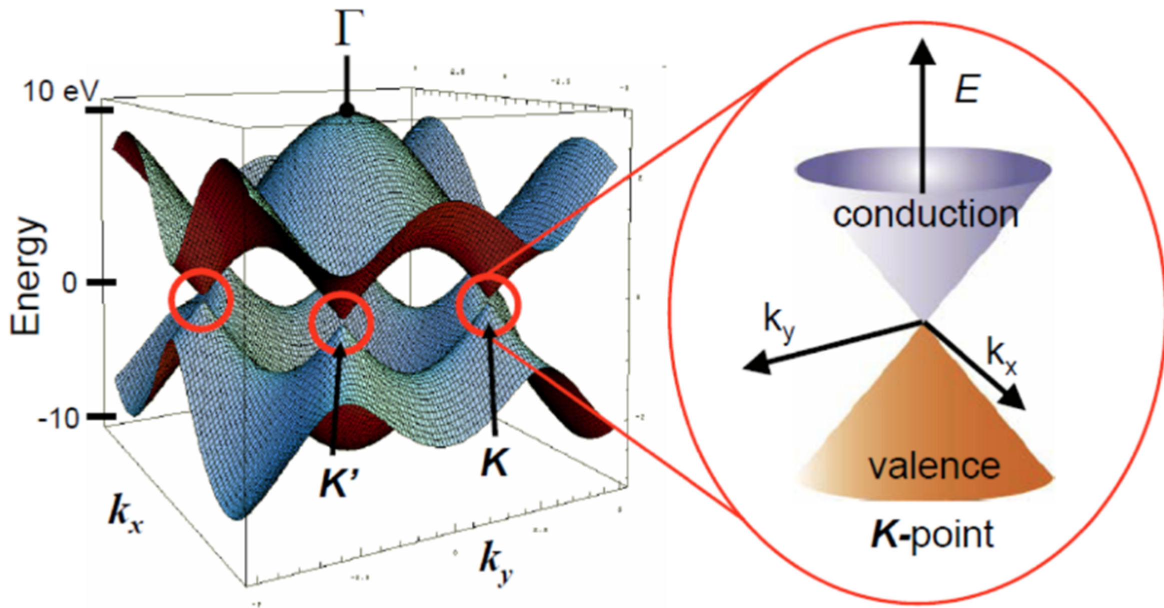

Figure 1.2: Bandstructure of monolayer graphene. The zoomed-in image on the right shows the linear band structure near the Dirac point, which is known as Dirac cone. Adapted from Ref. [5]

1.2 Bandstructure of Bilayer Graphene

When two monolayer graphene are stacked together, the most stable stacking order is the so-called AB stacking (or Bernal stacking). Fig. 1.3a presents the side view of the AB-stacked bilayer, where the A sublattice in the top layer directly overlay on the B sublattice of the bottom layer. In Fig. 1.3b one can see the top view of such a registry between the two layers. Among the total of four sublattices, the two directly overlay with each others interact strongly while the other two interact indirectly. The band structure of AB-stacked bilayer graphene can be qualitatively understood as the following: the two overlaid sublattices interact strongly so the electronic states originated from these two sublattices are pushed away from the Dirac point; wavefunction from the other two sublattices (we call as new A and B sublattices of the whole system) form the low energy states around the Dirac

point. Due to the inversion symmetry of the bilayer graphene (also of the new A and B sublattices), the conduction band and valence band are still degenerate at the Dirac point. The resulted band structure of intrinsic AB-stacked bilayer graphene is shown in Fig. 1.4a. The bands around the degenerate point have parabolic shape and an effective mass of 0.036 electron mass.

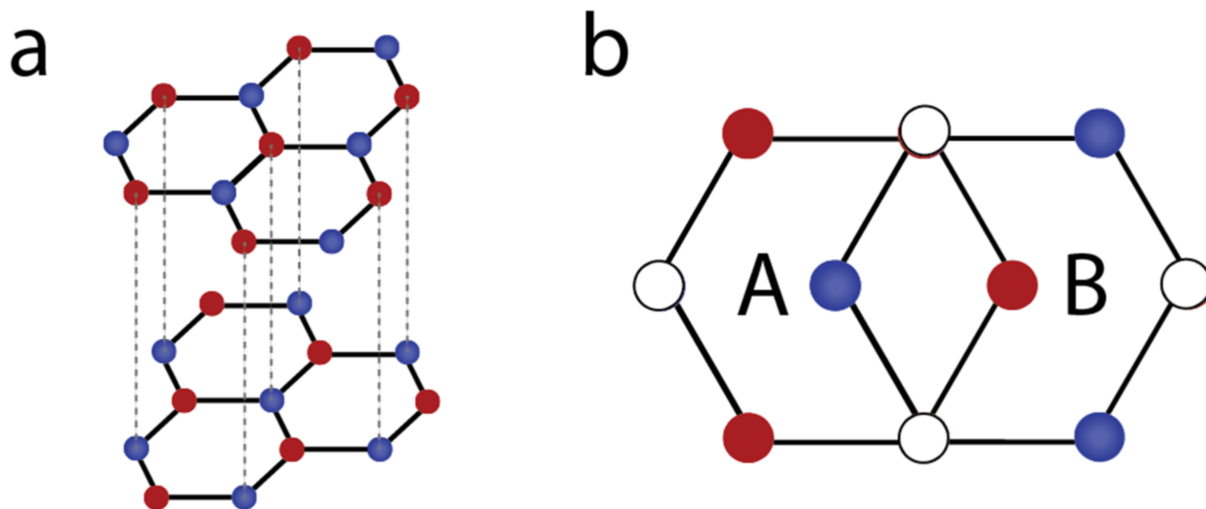

Figure 1.3: Atomic structure of AB-stacked bilayer graphene. a, Side view of the atomic structure of bilayer graphene. A sublattice in the top layer is directly on top of the B sublattice of the bottom layer. b, Top view of the bilayer graphene lattice. Hollow dots represent the sites shared by atoms from both top and bottom layers. The other sublattice from the top/bottom layer is named as the A/B sublattice of the whole system.

Compared to monolayer graphene, bilayer graphene has a unique feature: external gate electric field can dramatically modify the band structure of bilayer graphene[6][7][8]. Qualitatively speaking, if the two layers are put at different electrostatic potential, then the new A and B sublattices are no longer equally favorable to electrons. Therefore a finite bandgap will be opened at the Dirac point as can be seen in Fig. 1.4b. The states above the bandgap mostly reside at the higher potential energy layer while states below the bandgap mostly reside at the lower potential energy layer.

Such tunability of band structure from zero-bandgapped semimetal to finite bandgapped semiconductor is unique for graphene compared to bulk materials. One immediate application is to build field-effect-transistor (FET) on bilayer graphene, where the bandgap and

thus on/off ratio can be tuned at will. Such bilayer graphene FET has much higher on/off ratio[9] than that based on monolayer graphene while it still preserves the high mobility in graphene system. It has been shown that by using two gates on top and below the bilayer graphene, one can independently control the bandgap size and the charge doping level[10]. For us physicist, this additional knob of controlling material band structures opens a new door to various fascinating physical phenomena. We will describe one of them in Chapter 5.

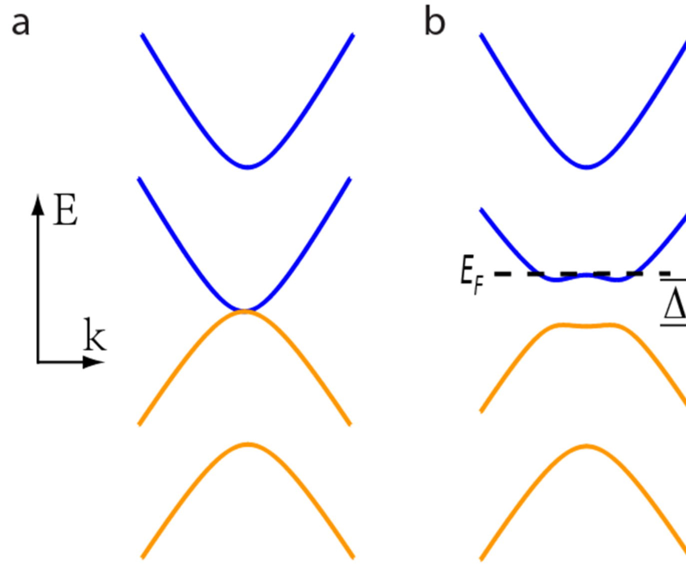

Figure 1.4: Bandstructure of bilayer graphene. a, Bandstructure of intrinsic bilayer graphene, where the highest valence band and the lowest conduction band are degenerate at the Dirac point. b, Bandstructure of bilayer graphene under external electric field perpendicular to the graphene plane. Δ is the induced bandgap while E_F represents the Fermi level. By tuning the top and bottom gate voltages, Δ and E_F can be independently controlled.

1.3 Optical Transitions in Graphene

With the aforementioned band structures of both monolayer and bilayer graphene, we are ready to discuss the basic optical transitions in both cases. There are two basic single particle optical excitations in graphene as shown in Fig. 1.5. The first one is called interband transition where an electron in the valence band absorbs photon and end up at a state in the conduction band. Since the speed of light is much larger than the Fermi velocity in graphene, such interband transitions are connecting two states with almost the same momentum. Obviously the position of Fermi level determines whether interband transition of specific energy is allowed or forbidden. By tuning the Fermi lebel by electrostatic gating,

the threshold energy of interband transition ($2|E_F|$) can be continuously tuned. The optical properties of graphene in mid-infrared to visible and ultraviolet range is mainly determined by the intreband transition.

The interesting fact about interband transition in monolayer graphene is that, at zero temperature, the optical conductivity is defined by fundamental constant as $\sigma(\omega) = \pi e^2/2h$ [11][12][13] which is independent of frequency ω. As a result, the corresponding absorbance is $A(\omega) = \pi\alpha \approx 2.3\%$, where α is the fine structure constant. This frequency-independent universal optical conductance is not totally unexpected since there is no characteristic energy scale in the linear band structure.

The other basic optical transition is the intraband transition as shown in Fig. 1.5b. Such transitions connect the initial state and final state within the same band. Due to the large mismatch between speed of light and Fermi velocity, intraband transition happens only with the momentum contributed by defects and impurities. The intraband transitions can be described by the Drude model where the conductivity is [14][15]

$$\sigma(\omega) = \frac{D\tau}{\pi}\frac{1}{1 + i\omega\tau} \tag{1.3}$$

The Drude weight $D = e^2 v_F \sqrt{\pi n}$ depends on the carrier density n and thus is tunable through gating. The scattering time τ is determined by the impurities and defects in the sample and can be extracted by measuring the DC conductivity. The optical properties of graphene in Terahertz and far-infrared range is dominated by the intraband transition. It has been shown that a monolayer graphene can absorb up to 30% [16] in the Terahertz range, which is about one order of magnitude stronger than in mid-infrared and visible range. We will revisit the intraband transition in Chapter 2.

Now we focus on the interband transitions in bilayer graphene. As mentioned in the previous section, intrinsic bilayer graphene has zero bandgap while a tunable bandgap can be induced by applying electric field. This bandgap can be directly visualized by measuring the absorption spectrum. Fig. 1.6a shows all possible interband transitions in gapped bilayer graphene when the sample is slightly doped into conduction band. The transistion energy of transition II and IV are almost degenerate at (350 meV-$\Delta/2$) while transition energy of III and V are almost degenerate at (350meV+$\Delta/2$). Transition I excites electrons across the bandgap Δ and gives a resonance peak in absorption spectrum due to parallel bands around the bandgap. Y. Zhang et al[10] for the first time demonstrated this tunable bandgap by infrared absorption measurement as shown in Fig. 1.6b and c. Peaks in Fig. 1.6b indicates a tunable bandgap up to 250 meV. More than a simple bandgap, transition I is associated with valley-dependent circular polarization selection rules that is determined by the non-zero Berry curvatures of electronic bands. One of the effects associated with the valley physics in bilayer graphene will be discussed in Chapter 5.

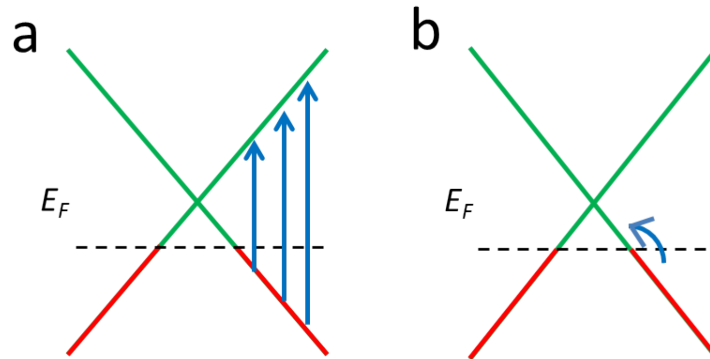

Figure 1.5: Optical transitions in monolayer graphene. a, Interband transitions from filled state (red line) in the valence band to empty states (green line) in the conduction band. b, Intraband transitions from states below the Fermi level to above the Fermi level in the same band.

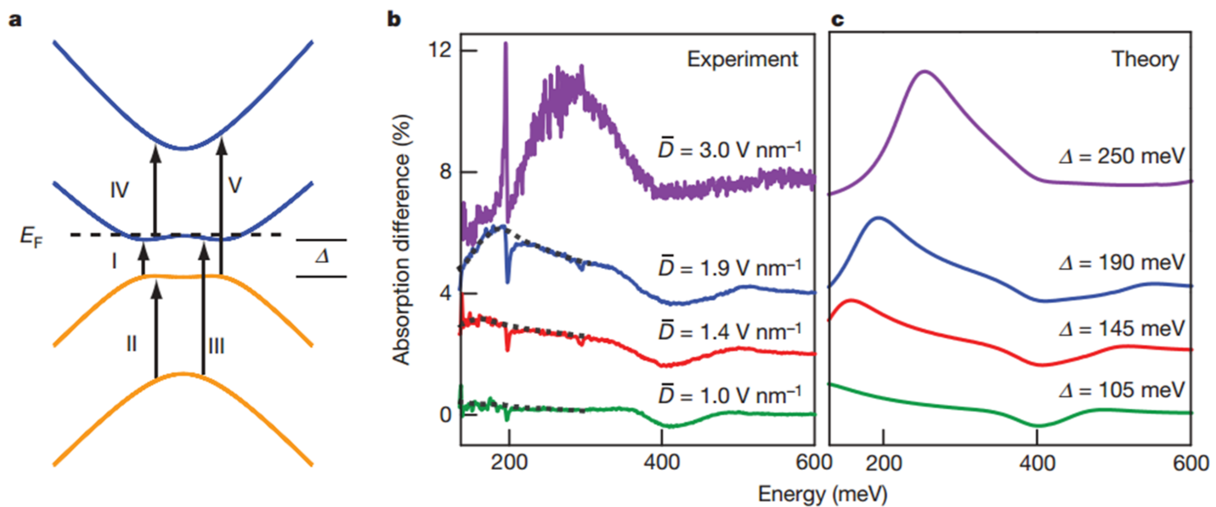

Figure 1.6: Gate-tunable optical transitions in bilayer graphene. a, Possible interband transitions in bilayer graphene. Transition II and IV are almost degenerate while transition III and V are almost degenerate. Transition I across the bandgap is most sensitive to external electric field. b, Experimental absorption spectrum for bilayer graphene at different bandgap size. The absorption peak position corresponds to the bandgap energy. c, Theoretically calculated absorption spectrum at different bandgap sizes. Adapted from Ref. [10]

1.4 Outline of the Thesis

This dissertation is organized as follows.

Chapter 2 describes an optical spectroscopy study of plasmon excitations in monolayer graphene.

Chapter 3 presents an opto-electronic phenomenon, named as photo-induced doping, in heterostructures of graphene and hexagonal boron nitride. This phenomenon originated from the defect states in boron nitride.

And as a natural extension of the optical study of defect states in boron nitride, Chapter 4 is an STM study of the defect states in boron nitride on the same sample as used in experiment presented in Chapter 3.

Chapter 5 describes a combination of electric transport and near field infrared nanoscopy to reveal the topological boundary states at the domain walls of exfoliated bilayer graphene.

Chapter 2

Plasmon Excitations in Monolayer Graphene

Plasmons are collective electron oscillations resulting from the Coulomb interaction. Such collective excitations play a fundamental role in dynamic responses of electron systems, and they form the basis of the thriving research field of metal plasmonics and optical metamaterial[17][18][19]. Plasmons of two-dimensional massless electrons, as present in graphene, can exhibit unusual behavior[20][21][22][23] that is different from their conventional counterpart, which can enable novel tunable plasmonic metamaterials[24][25][26] and have been proposed for exciting optoelectronic applications in the terahertz (THz) frequency range[24][25][27][28]. In this chapter I will describe our study of light-plasmon coupling in graphene and demonstrate strong plasmon resonances in engineered graphene micro-ribbon arrays. We demonstrate that graphene plasmon resonances can be tuned over a broad terahertz frequency range by changing the micro-ribbon width and in situ electrostatic doping. The ribbon width and carrier doping dependences of graphene plasmon frequency exhibit power law behavior characteristic of two-dimensional massless Dirac electrons[20][21][22]. The plasmon resonances have remarkably large oscillator strengths, as manifested in prominent room-temperature plasmon absorption peaks. In comparison, plasmon absorption in a conventional two-dimensional electron gas was observed only at 4.2 K (Ref. 29, 30). The strong and tunable plasmon excitations in graphene are promising for graphene-based THz metamaterials.

This chapter is adapted with permission from L. Ju et al., "Graphene plasmonics for tunable terahertz metamaterials", Nature nanotechnology **6**, 630 (2011). Copyright 2011 Nature Publishing Group.

2.1 Introduction to Plasmons in Two Dimensional Systems

Plasmon is the quanta of oscillation formed when an emsemble of electrons and positive charges (known as plasma) is excited by electromagnetic waves. The physical origin of this oscillation mode is the Coulomb interaction between electrical charges. Lets consider a ribbon of 2 dimensional material in general as depicted in Fig. 2.1. When linear polarized light perpendicular to the ribbon is introduced, electrons will oscillate under this external stimuli and accumulate at the ribbon edge. Correspondingly, positive charges will accumulate at the opposite edge due to conservation of total charge in the ribbon. These two charged lines will attract each other by Coulomb interaction and form an oscillation mode under this restoring force. This oscillation mode is plasmon. In contrast, when the light is polarized parallel to the ribbon, electrons will move freely due to the lack of physical confinement and the restoring force. Thus the motion of electrons are described by the free electron model which has a resonance frequency at zero.

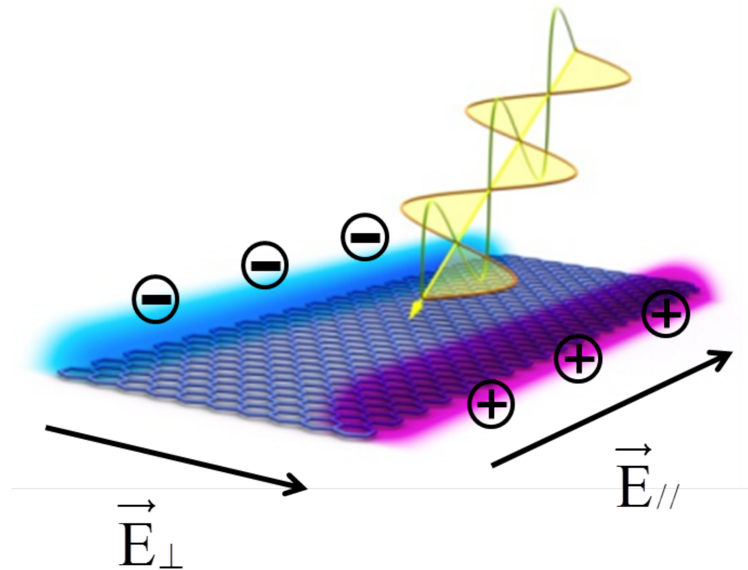

Figure 2.1: Illustration of plasmon in a ribbon of material. Under illumination with light polarized perpendicular to the ribbon, electrons oscillate across the ribbon width and accumulate at the edge. The Coulomb interaction between charged lines provides a restoring force to establish the plasmon mode. In contrast, the parallel polarization light only excites the free carrier oscillation due to no physical confinement along the ribbon direction.

The details of both oscillation modes will be described later in this chapter. Nevertheless,

some basic characteristic can still be extracted from this simple model. It is easy to see that the plasmon resonance frequency depends on the geometric shape (the ribbon width in this case). If we push to the limit where the ribbon width is infinite as in the parallel polarization case, the plasmon frequency goes to zero. This is distinct from the senario in a 3D material where the plasmon frequency is largely independent of the distance between the two charged planes. Such character holds generally true for 2D systems regardless of the materials properties.

We just considered the plasmon in a 2D ribbon where physical confinement is important. The plasmons can also exist in a homogeneous layer of 2D materials. Once the plasmon mode is excited, the system will develop a periodic charge distribution similar to the charged lines in the ribbon case. So the physical origins of plasmon in both cases are the same, and they obey the same scaling laws as we will talk about later in this chapter.

2.2 Fabrication of the Dual-Gated Graphene Micron-Ribbon Array

In general, the dispersion relation of photons and 2D plasmons are different as shown in Fig. 2.2. Photons have a linear dispersion defined by the speed of light c that's way higher than the phase/group velocity of 2D plasmons. As a result, the two dispersion curves intersect each other at very low frequencies that cannot be detected by experiment. Therefore to excite the plasmon oscillation in graphene is an experimental problem due to the momentum mismatch between photons and plasmons.

Figure 2.3 shows a few ways to reconcile this momentum mismatch. The first one as shown in Fig. 2.3a is to engineer graphene into an array of ribbons, which has a well-defined period. The second method is shown in Fig. 2.3b where the evanescent wave at an total internal reflection interface is utilized. The third experimental scheme is to change the local field distribution by shining far-field radiation to a metal tip, as shown in Fig. 2.3c. The spirit of all these experimental approaches is to create an extra in-plane momentum for the photons so it can match that of the plasmon with the same frequency. The momentum of photons or electromagnetic field is characterizing the periodicity of the field distribution. In the ribbon array case, the array period defines the period of electric field distribution when plane wave is incident on the 2D plane. In the case of total internal reflection, a real in-plane momentum larger than the total momentum is accompanied by a imaginery out-of-plane momentum, and the in-plane mementum matches the plasmon momentum. The tip enhanced near-field scheme basically introduces many momentum components (basically fourier transforming a delta function-like field distribution).

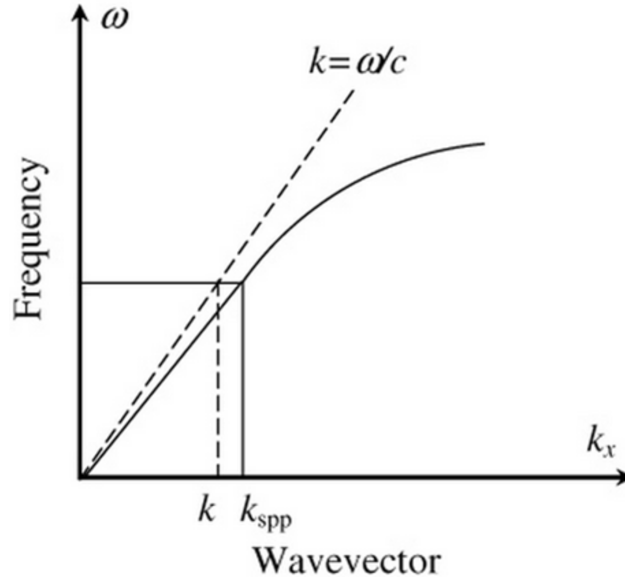

Figure 2.2: Dispersion relation of photons and plasmons. The dash line represents the linear dispersion relation of photons in homogeneous media. The solid line represents the dispersion relation of 2D plasmons, which intersects the dash line at very low frequencies. The momentum mismatch between the two dispersions at the same frequency forbids direct excitation of plasmon by electromagnetic radiation.

In our study we used a graphene micro-ribbon arrays illustrated in Fig. 2.1 (not to scale) for THz plasmon excitations. The ribbon width varied from 1 to 4 μm and the gap and ribbon width ratio was kept at 1:1. We grew large-area graphene using chemical vapor deposition on copper and transferred the graphene sheet onto a Si/SiO_2 wafer following ref. Au/Cr electrodes of 50 nm thickness were deposited onto the graphene sheet in vacuum using stencil masks. Micro-ribbon arrays were fabricated in a 2.5x2.5 mm^2 area at the center of the graphene sheet using standard optical lithography followed by oxygen plasma etching.

We used CVD graphene for this study because of an experimental consideration. To do reflection or transmission spectroscopy, the sample has to be larger than the light beam spot size which is determined by the wavelength and the effective numerical aperture. This is described by the diffraction limit of electromagnetic wave through equation:

$$D = \frac{1.22\lambda}{N.A.} \tag{2.1}$$

λ is the wavelength of light. The numerical aperture (N.A.) is usually on the order of 0.1 and in the terahertz range this would set a spot diameter of 1 mm for frequency of 3 THz. Thus a sample size on the order of mm is required for such measurement. This can only be satisfied by graphene grown by the CVD method since exfoliated monolayer graphene flakes

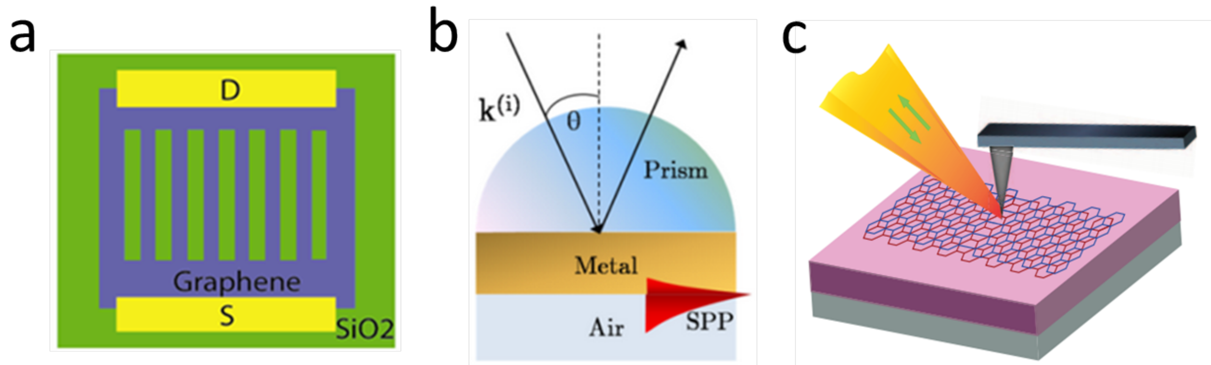

Figure 2.3: Experimental approaches to solve momentum mismatch between photons and plasmons. a, Engineered 2D ribbon array where the period defines an in-plane momentum for light. b, Evanescent wave existing at the interface between prism and metal due to total internal reflection. The evanescent wave carries an in-plane momentum larger than the total momentum which allows it to couple to plasmons. c, Near-field enhancement of electric field around the metal tip provides many momentum components to match the plasmon momentum.

are usually ∼10 μm big.

The ribbon array can be operated as a field-effect-transistor since the carrier concentration in graphene is controlled by an ion-gel[32] top gate, which allows for a large doping range (10^{13} - 10^{14} cm^{-2}). This doping level is about one order of magnitude higher than that can be achieved by gating through oxide dielectrics, where the electrical breakdown limits the applied electric field. Figure 2.1b shows the schematic side view of a typical gated device. Usually the device has a charge neutral point (CNP) within 0.5V of top gate voltage (V_g), and the typical electron mobility is our sample is $\sim$ 1000 cm^2/V.s.

2.3 Basics of Fourier Transform Infrared Spectroscopy

We studied plasmon resonances and the light-plasmon coupling in graphene micro-ribbon arrays using polarized Fourier Transform Infrared (FTIR) spectroscopy, which is a powerful and commonly used tool in infrared range. Here I want to talk about the basic working principles of FTIR.

To do optical spectroscopy on materials is basically collecting light with different frequencies seperately. Usually people send in light with all different frequency together rather

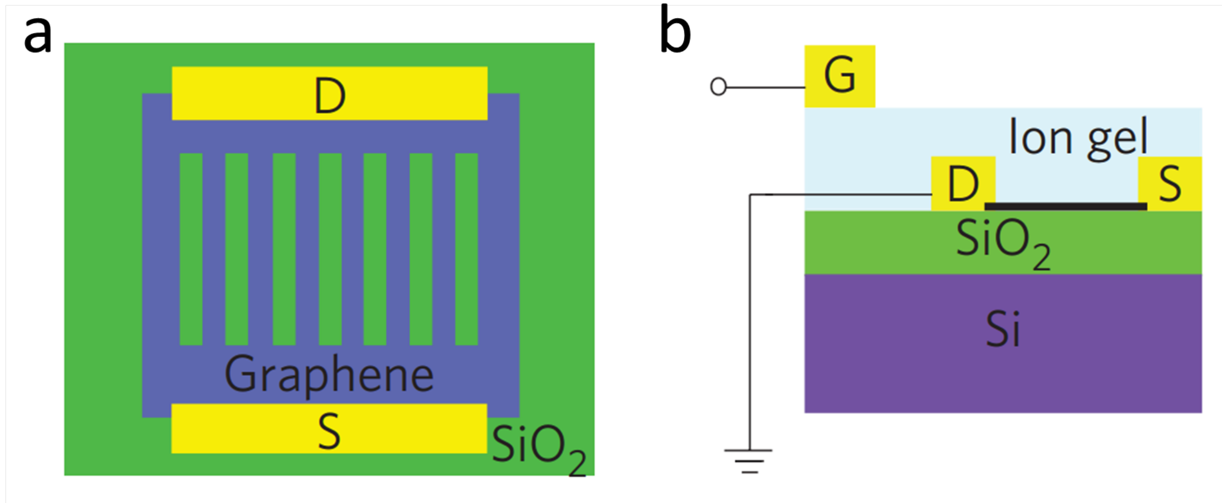

Figure 2.4: Topview and sideview of graphene micro-ribbon array device. a. Topview of graphene micro-ribbon device. A CVD-grown graphene layer is transferred onto a SiO_2/Si substrate. The graphene is etched into an array of ribbons with width of micrometers. Souce and drain electrodes are deposited in the direction perpendicular to ribbons. b. Topview of graphene micro-ribbon array device. Ion gel covers graphene and the top gate electrodes. Graphene is grounded and a voltage is applied between top gate and graphene.

than one by one. To seperate them before the detector, one can use a dispersive media like a grating to direct light with different frequency to an array of detectors like in a charge coupled detector (CCD) camera. Alternatively, one can make use of the time domain instead of space domain to achieve seperation of different frequency. The basic idea is to utilize the relation between frequency and time of electromagnetic oscillation. We collect light intensity signal as a function of time and use fourier transform to project it into frequency domain. The experimental setup for this measurement is illustrated in Fig. 2.5. The beam is first splitted into two and go through different path before they meet again to propogate to the detector. The mirror on one arm will be scanned to tune the time delay between the two beams.

Assume the electric field of the initial beam is

$$E_{inc}(t) = \int_0^\infty E(\omega) \times e^{-i\omega t} d\omega \tag{2.2}$$

Now we can write down the electric field of the beam at the detector

$$E_{detector}(t) = \int_0^\infty (\alpha_1(\omega) E(\omega) \times e^{-i\omega t} + \alpha_2(\omega) E(\omega) \times e^{-i\omega t} e^{-i\omega t_0}) d\omega \tag{2.3}$$

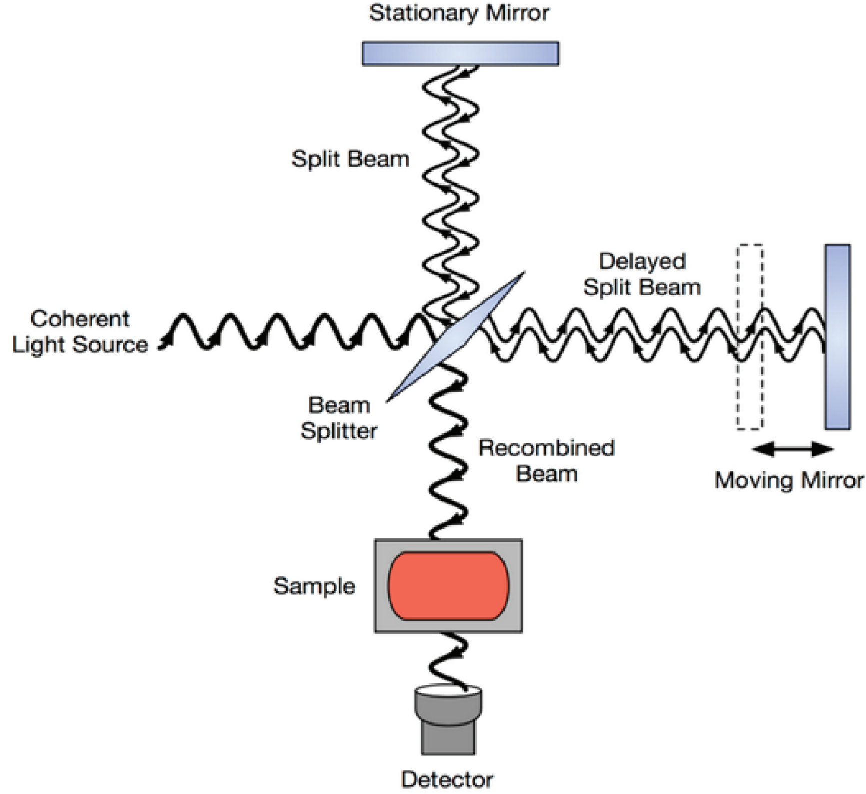

Figure 2.5: Illustration of fourier transform spectroscopy. The light is splitted into two beams that will be recombined later by the same beamsplitter. The moving mirror tune the delay between the two beams and result in interference at the detector.

where $\alpha_1(\omega)$ and $\alpha_2(\omega)$ accounts for the amplitude change of beam 1 and beam 2 introduced by the setup and t_0 represents the time delay introduced by the moving mirror. The detector reads the averaged intensity (here we neglect the constant terms that is independent of t_0) with a frequency dependent response coeffient $C(\omega)$

$$|E_{detector}(t)|^2_{avg} = \int_0^\infty (|C(\omega)|^2 \alpha_1(\omega)\alpha_2(\omega) |E(\omega)|^2 \times e^{-i\omega t_0})d\omega \tag{2.4}$$

where the cross-term of different frequency is averaged out due to the oscillating phase. By doing fourier transform of t_0 we can extract the component of specific ω:

$$P(\omega) = |C(\omega)|^2 \alpha_1(\omega)\alpha_2(\omega) |E(\omega)|^2 \tag{2.5}$$

Usually the measurement is done by choosing a reference with known optical properties. For example when there's no sample in Fig. 2.5, we get:

$$P(\omega)_{reference} = |C(\omega)|^2 \alpha_1(\omega)\alpha_2(\omega) |E(\omega)|^2 \tag{2.6}$$

while its counterpart when the sample is inserted in is

$$P(\omega)_{sample} = |C(\omega)|^2 \alpha_1(\omega)\alpha_2(\omega) |E_{sample}(\omega)|^2 \tag{2.7}$$

Therefore by doing normalization we can get the transmission coefficient of the sample as:

$$T = P(\omega)_{sample}/P(\omega)_{reference} = |E_{sample}(\omega)|^2 / |E(\omega)|^2 \tag{2.8}$$

Based on the relation between frequency and time delay we know that the frequency resolution obtained in this way is determined by the travelling length of the moving mirror:

$$\delta\omega = 1/t_{scan} \tag{2.9}$$

2.4 Absorption Spectrum of Free Carriers and Plasmons of Graphene in the Far-Infrared Range

Infrared absorption from doped charge carriers is directly related to $-\Delta T/T_{CNP}$, the gate-induced decrease of transmission through the graphene micro-ribbon arrays. Here T_{CNP} is transmission coefficient at CNP and $\Delta T = T - T_{CNP}$. The $-\Delta T/T_{CNP}$ spectra of a gated 4 μm sample (V_g= -2.0 V) for THz radiation polarized parallel and perpendicular to the ribbons are displayed in Fig. 2.6a and b, respectively.

For incident light polarized along the ribbons the electrical response of charge carriers is similar to that of free electrons in a homogeneous graphene sheet, and the spectral shape is well described by the Drude model as $\mathrm{Im}(-1/(\omega + i\Gamma_D))$ (black dash line in Fig. 2.6a) with a scattering rate Γ_D of 4 THz. This Drude absorption decreases monotonically with frequency ω. For incident light polarized perpendicular to the ribbon the resulting spectrum is completely different: an absorption peak arising from plasmon oscillation dominates the optical response (Fig. 2.6b). This plasmon absorption lineshape can be described by a damped oscillator as $\mathrm{Im}(-\omega/(\omega^2 - \omega_p^2 + i\omega\Gamma_p))$ (blue dash line) with a plasmon resonance ω_p at 3 THz and a spectral width Γ_p of 4 THz. There is also a small background contribution from the free carrier absorption (magenta dashed line) because part of the infrared beam transmits through unpatterned graphene around the micro-ribbon array. The light-plasmon coupling in graphene is remarkably strong, with over 13 % absorption at the plasmon resonance for half of one doped carbon monolayer. The observed plasmon resonance linewidth is similar to the Drude scattering rate for parallel light polarization, suggesting that the plasmon broadening is largely limited by the same scattering processes affecting electrical transport.

The light-plasmon coupling in graphene is remarkably strong compared with that in conventional 2DEGs in semiconductors. It arises both from the small effective electron mass and the efficient electrical gating in graphene. In conventional 2DEGs the field-induced carrier

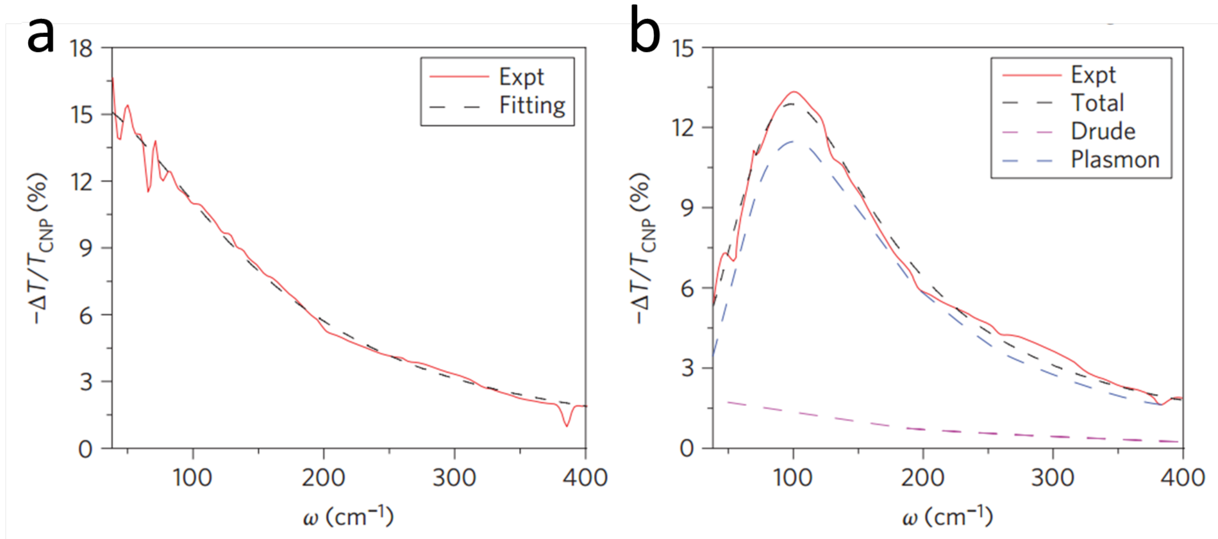

Figure 2.6: Absorption spectrum of graphene-ribbon array under parallel polarized light illumination. a. Absorption spectrum of parallel light polarization. The gate voltage was set at V_g= -2.0 V. The response originates from free carrier oscillation and can be well reproduced by a Drude fit (black dashed line). b. Absorption spectrum of perpendicular light polarization. The spectrum shows a prominent absorption peak at 3 THz (1 THz = 33.3 cm$^{-1)}$) because of plasmon excitation. Plasmon resonance is characterized by a Lorentzian lineshape (blue dashed line). A small free carrier contribution described by Drude absorption (magenta dashed line) is also present as a result of graphene absorption outside the fabricated micro-ribbon array area.

concentration is limited to $\sim 10^{12}$ cm^{-2} to avoid semicondcutor dielectric breakdown. At this carrier density, effective mass of electron at Fermi energy is 0.02 in graphene. This electron effective mass is 3.5 (13) times smaller than that in GaAs (Si), and the integrated plasmon oscillator strength is correspondingly larger. In addition, graphene can be gated much more efficiently to over 10^{13} cm^{-2} because of its excellent chemical stability and compatibility with different gating configurations. The resulted light-plasmon coupling in graphene can be an order of magnitude stronger than that achieved in conventional 2DEGs, and enabled us to observe the THz plasmon resonance for the first time at room temperature.

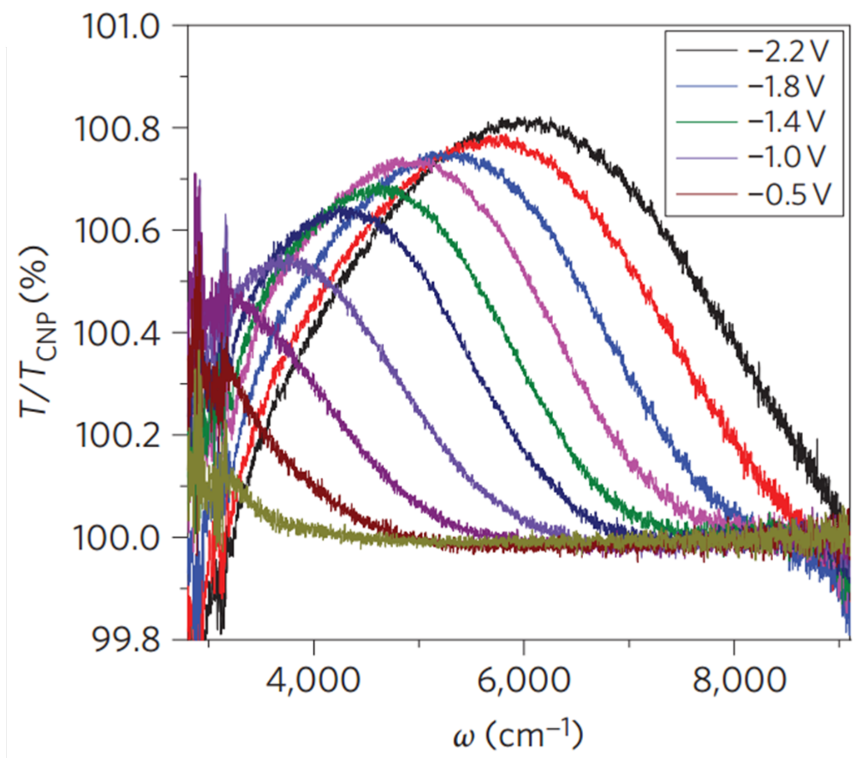

Figure 2.7: Mid-infrared transmission spectra, T/T_{CNP}, of the graphene ribbon array as gate voltage V_g - V_{CNP} varies from -0.3 to -2.2 V. The voltages corresponding to the unlabelled lines, starting with the red line and alternating downwards, are: -2.0 V, -1.6 V, -1.2 V, -0.7 V and -0.3 V. On electrical gating, optical transmission is increased up to a threshold energy of $2|E_F|$ as a result of blocked interband optical transitions.

2.5 Tuning of Plasmon Resonance by Electrical Gating and Structure Engineering

The plasmon resonance in graphene micro-ribbon arrays can be tuned in situ by electrostatic doping. For simplicity we will focus on the hole-doping regime. We determine the gate-induced Fermi energy shift and carrier concentration in graphene through interband optical transitions[33][34]. This is based on the effect that interband transitions can be blocked up to $2|E_F|$ energy in hole-doped graphene due to empty initial states. Fig. 2.7 shows gate-induced changes of interband transmission spectra in the 3000-9000 cm^{-1} spectral range at different gate biases. Increased infrared transmission is observed up to a threshold energy that shifts to higher values with increased doping. This threshold energy is at $2|E_F|$ (Ref. 1,2), from which carrier concentration can be deduced by

$$n = (E_F/\hbar v_F)^2)/\pi \tag{2.10}$$

as in ref. 1 and 2. Plasmon excitations in the graphene micro-ribbon array can be varied by electrical gating, as shown in Fig. 2.8 for absorption of perpendicularly polarized light. Prominent plasmon absorption peaks are observed, which shift to higher energies and gain oscillator strength with increased carrier concentration. For comparison we show in the inset of Fig. 2.8 free carrier absorption spectra at different gate voltages (probed with light polarized parallel to micro-ribbons). The spectral shape remains the same in all spectra, although the oscillator strength increases with the carrier concentration.

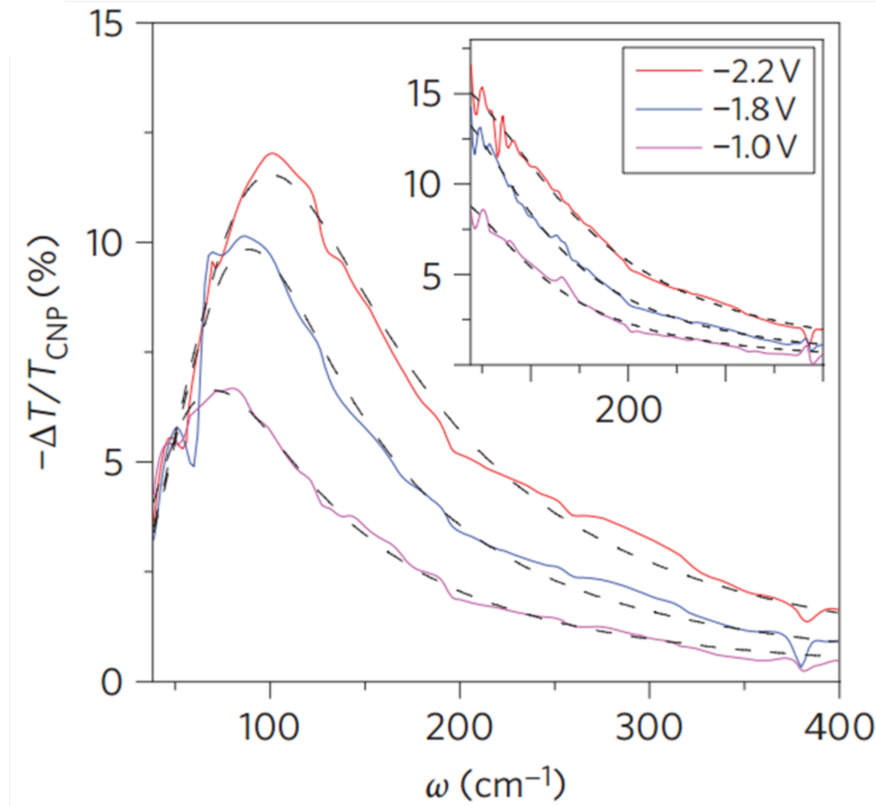

Figure 2.8: Control of terahertz resonance of plasmon excitations through electrical gating. Terahertz radiation was polarized perpendicular to the graphene ribbons. The plasmon resonance shifts to higher energy and gains oscillator strength with increased carrier concentration. For comparison, the inset shows corresponding spectra due to free carrier absorption for terahertz radiation polarized parallel to the ribbons. For this polarization, absorption strength increases with carrier concentration, but spectral shape remains the same.

Plasmon excitations in graphene micro-ribbon arrays can also be controlled by engineering the ribbon width. We show in Fig. 2.9 -$\Delta T/T_{CNP}$ spectra of three micro-ribbon arrays with 1, 2, and 4 μm ribbon width. All spectra were taken at the same hole doping concentration and they have been normalized by the respective peak values for convenience of

comparison. The plasmon resonance clearly shifts to higher energy with decreasing ribbon widths: resonance frequencies are at 3, 4.1, and 6 THz for ribbon arrays of 4, 2, and 1 μm ribbon width, respectively. Using nano- and micro-ribbon arrays with larger range of ribbon widths, THz resonance from 1-10 THz could be straightforwardly engineered.

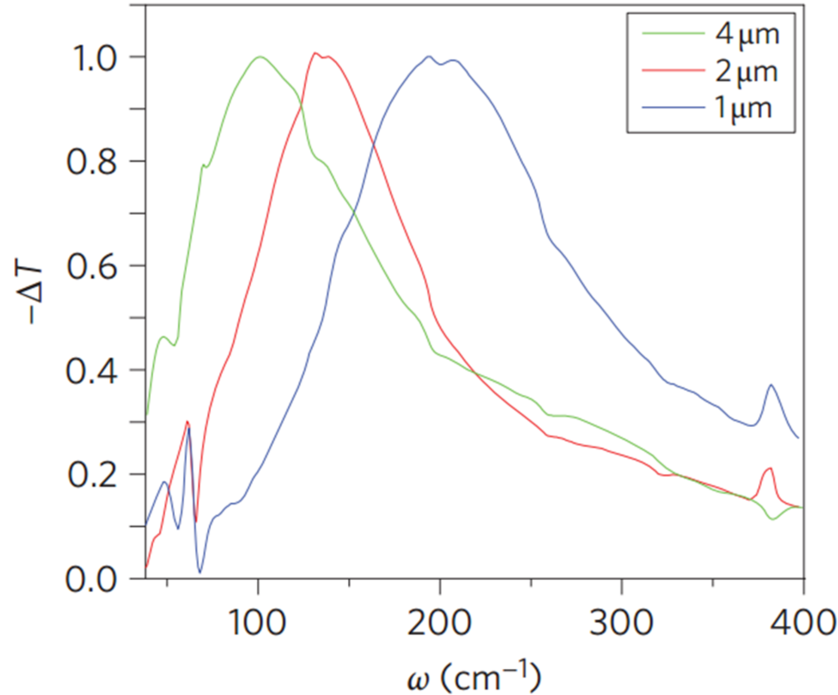

Figure 2.9: Change of transmission spectra with different graphene micro-ribbon widths for the same doping concentration of 1.5×10^{13} cm^{-2}. All spectra were normalized by their respective peak values for convenience of comparison. Plasmon resonance frequency vp shifts from 3 to 6 THz when micro-ribbon width decreases from 4 to 1 μm.

2.6 Scaling Laws and Numerical Simulation of Plasmon Modes in Graphene Ribbon Array

Next we examine quantitative scaling behavior of plasmon resonance frequency with the carrier concentration and ribbon width. In Fig. 2.10 we plot plasmon resonance frequencies as a function of $|E_F|$ (or equivalently $|n|^{1/2}$ in the top label) for different micro-ribbon widths. For a given carrier concentration, the plasmon resonance frequencies in different graphene micro-ribbon arrays are described by a scaling behavior of $\omega_p \propto w^{-\frac{1}{2}}$. This is best shown in Fig. 2.11, where all data in Fig. 2.10 collapse into a universal curve once

the plasmon resonance frequencies are rescaled by $w^{-\frac{1}{2}}$. This scaling of ω_p with inverse square root of the relevant spatial dimension is characteristic of 2D electron gases[21][22], in contrast to a constant plasmon resonance frequency in bulk plasmons. The universal relation between ω_p and $|E_F|$ in Fig. 2.10 can also be described by a power law scaling with $\omega_p \propto |E_F|^{1/2} \propto n^{1/4}$. This power law dependence of plasmon frequency is a signature of massless Dirac electrons[20][21][22], which is in contrast to scaling (dashed line) in conventional semiconductors.

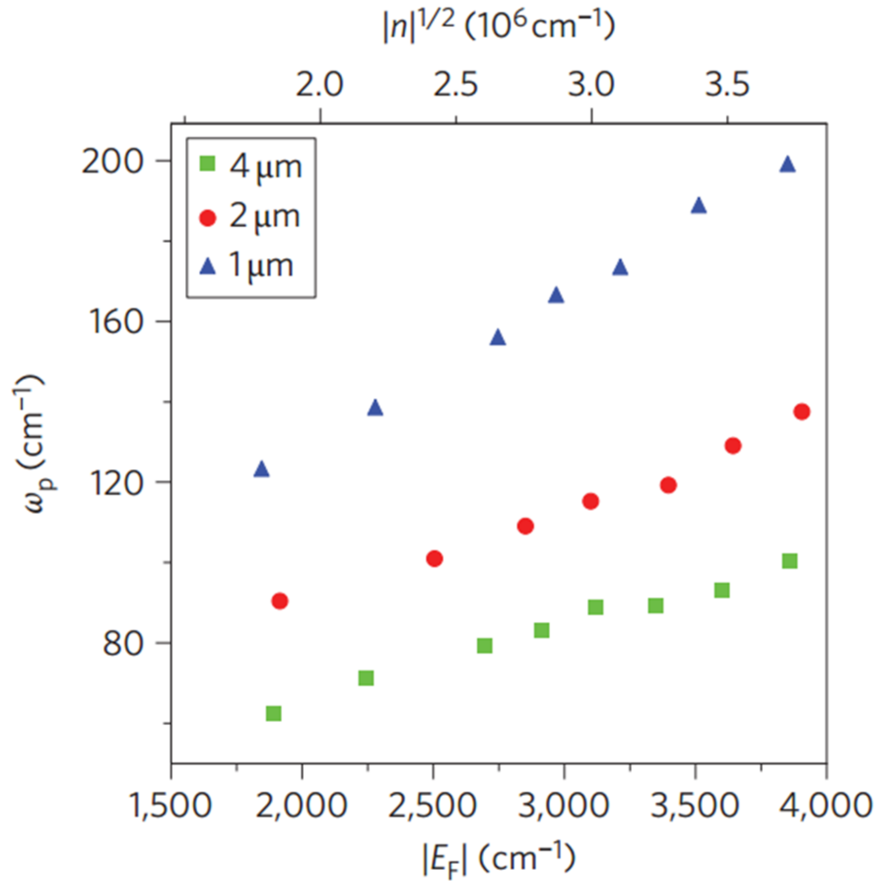

Figure 2.10: Plasmon resonance frequency ω_p as a function of $|E_F|$ (or equivalently $|n|^1/2$ in the top label) for micro-ribbon arrays of different widths.

A theoretical understanding of the scaling behavior of plasmon resonance in micro-ribbon arrays can be achieved using the quasi-static description, which is a good approximation for ribbon widths (∼1 μm) much smaller than photon wavelengths (∼100 μm). The Maxwell

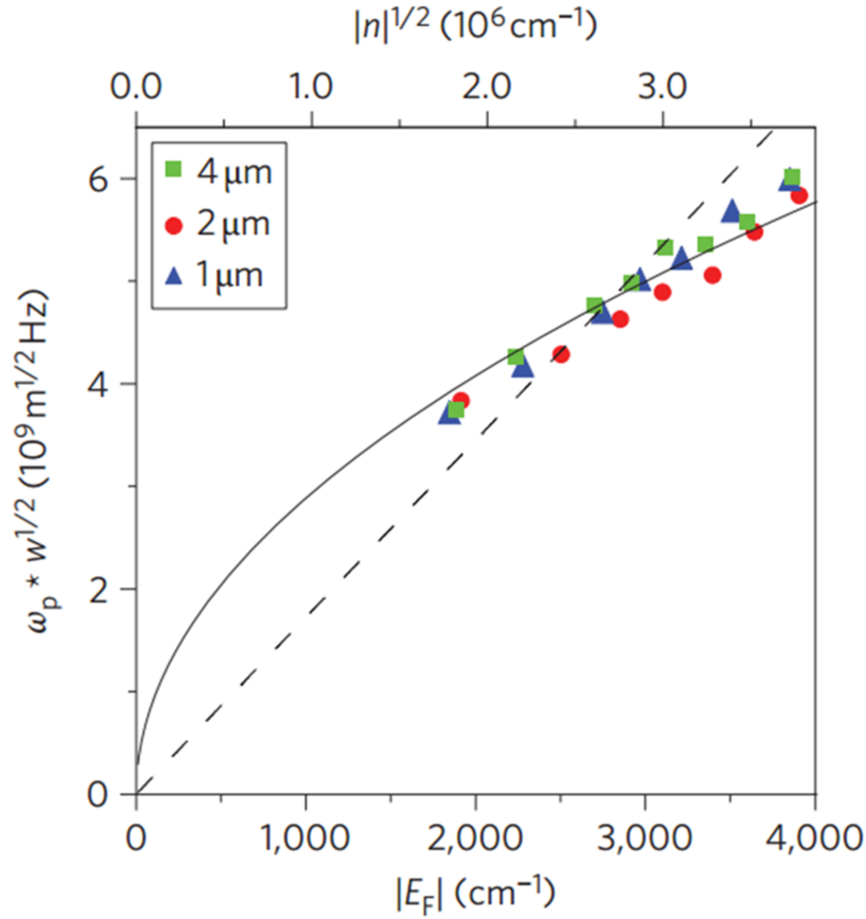

Figure 2.11: Scaling laws of graphene plasmon resonance frequency. Plasmon excitation ω_p was normalized by $w^{-\frac{1}{2}}$ for micro-ribbon arrays of different widths, which fits all data points (symbols) into a universal curve (solid line). This $w_{1/2}$ scaling of vp is characteristic of 2D electron systems. The universal doping dependence of plasmon resonances is described by a scaling law of $\omega_p \propto |E_F|^{1/2} \propto n^{1/4}$. This $n^{1/4}$ scaling law is a signature of massless Dirac fermions. In comparison, ω_p scales as $n^{1/2}$ (dashed line) in conventional semiconductors.

equations satisfying the 2D ribbon array boundary conditions can be simplified to

$$\frac{\partial \Phi}{\partial y} = \frac{-2\pi i}{\kappa \omega} \frac{\partial}{\partial x}(\sigma^{2D} F(x) \frac{\partial \Phi}{\partial x}) \tag{2.11}$$

where κ is the effective dielectric screening constant, σ^{2D} is the 2D high-frequency conductivity at carrier concentration n, and *F(x)* is a square function with *F(x)*=1 at ribbon positions and *F(x)*=0 in the gap. By introducing dimensionless parameters X=x/w and Y=y/w and using the expression of σ^{2D} for massless Dirac electrons, the above equation can also be

expressed as

$$\frac{\partial \Phi}{\partial Y} = \eta \frac{\partial}{\partial X}(F(x)\frac{\partial \Phi}{\partial X}) \tag{2.12}$$

with the dimensionless parameter

$$\eta = \frac{2\pi^{1/2}}{\omega(\omega + i\Gamma)} \frac{v_F e^2}{\hbar} \frac{n^{1/2}}{\kappa w} \tag{2.13}$$

Electrodynamic responses of a micro-ribbon array are uniquely determined by the dimensionless parameter η. Maximum absorption of the incident light takes place at a specific η value, which determines the plasmon resonance frequency for given w and n. When either ribbon width or carrier concentration changes, the plasmon frequency will change accordingly following the scaling behavior of $\omega \propto n^{1/4} \propto w^{-1/2}$ (for weak damping rate Γ as we observed experimentally).

Although the differential equation readily explains the scaling behavior of the plasmon resonance frequency, it cannot be solved analytically for a quantitative value of ω_p. Instead we use numerical calculations based on finite element methods to simulate this system, which has only one unknown parameter, namely the dielectric constant κ. Using a κ value of 5, the simulation (dash line in Fig. 2.12) reproduces nicely the observed -$\Delta T/T_{CNP}$ spectrum for a ribbon width of 4 μm and doping concentration of 1.5×10^{13} cm^{-2} (solid line in Fig. 2.12). The κ value of 5 is reasonable in our devices given that THz dielectric constants of ion gel, SiO2 and silicon are 3 (ref. 35), 4, and 11 (ref. 36), respectively. Such a dielectric screening constant will lead to an electron-electron interaction strength of α_G=$e^2/\kappa\hbar v_F$ $\approx$0.4.

We plot in Fig. 2.13a, b, and c simulation results for current density amplitudes (upper panels) and phases (lower panels) in the same micro-ribbon array for frequencies below resonance (1 THz), at resonance (3 THz), and above resonance (5 THz), respectively. The current distribution describes electrons oscillating back and forth across the width of graphene micro-ribbons upon THz radiation. The oscillating current amplitude is the largest at the plasmon resonance frequency. Simultaneously the phase of current oscillation relative to that of incident electric field varies quickly and changes its sign across the resonance frequency. Both behaviors are typical characteristics of a resonance excitation.

2.7 Comparison to Plasmons in Other 2D Electron Gas Systems

Experimentally we observed a plasmon absorption resonance more than an order of magnitude stronger than that achieved preciously in conventional two-dimensional electron systems. This strong light-plasmon coupling in graphene originates from two contributions.

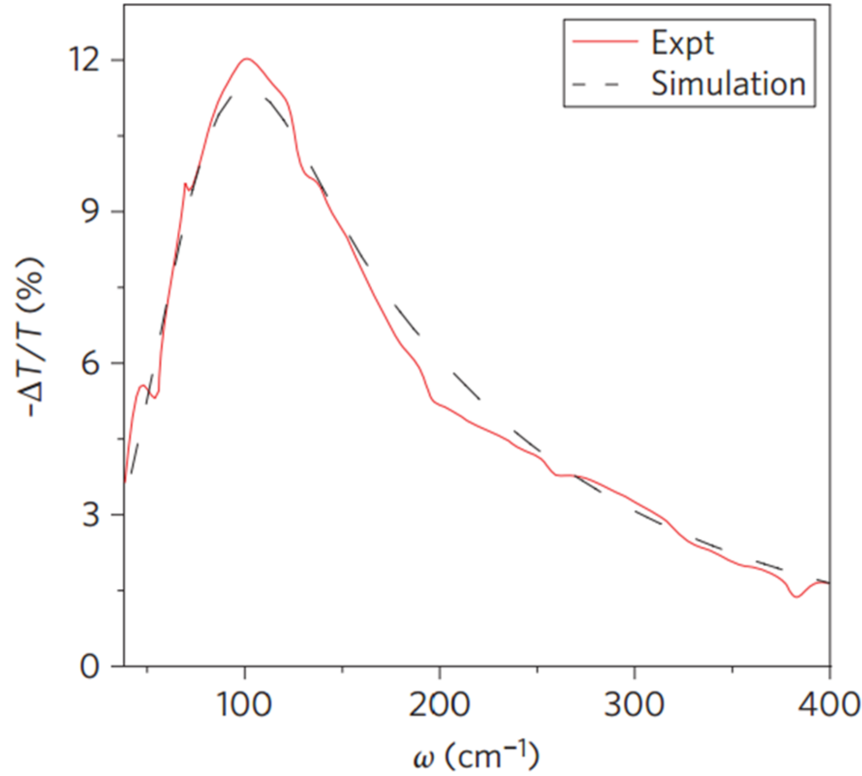

Figure 2.12: Transmission change spectrum -$\Delta T/T_{CNP}$ simulated by finite element analysis (dashed line) at carrier concentration of 1.5 $\times$ 10^{13} cm^{-2}. It reproduces well the experimentally observed spectrum (solid line) when the effective environment dielectric constant κ was set as 5, and corresponds to an electron−electron interaction strength of α_G=$e^2/\kappa\hbar v_F$ ≈0.4

(1) Because plasmon resonances in graphene and conventional 2DEGs have different dependence on carrier concentration, we need to specify a carrier density to start our comparison. Here lets use a carrier concentration of $n = 10^{12}\ cm^{-2}$, which is the highest field-induced electron density achieved in previous plasmonic studies (Ref. 13 and 14).

The integrated oscillator strengths of plasmon resonance is inversely proportional to the effective electron mass. For graphene, the Dirac electrons have an effective mass proportional to the Fermi energy, which has a value 0.02 m_0 at $n = 10^{12}\ cm^{-2}$. This is 3.5 (13) times smaller than the electron effective mass in GaAs (Si), which give rise to a light-plasmon coupling 3.5 (13) times stronger than that in GaAs (Si).

(2) For conventional 2DEGs, gate-tunable electron density is usually limited to $\sim 10^{12}$ cm^{-2} because these 2DEGs have to be imbedded in other semiconductors which has a relatively low electric breakdown field. In contrast, graphene has superior chemical stability and

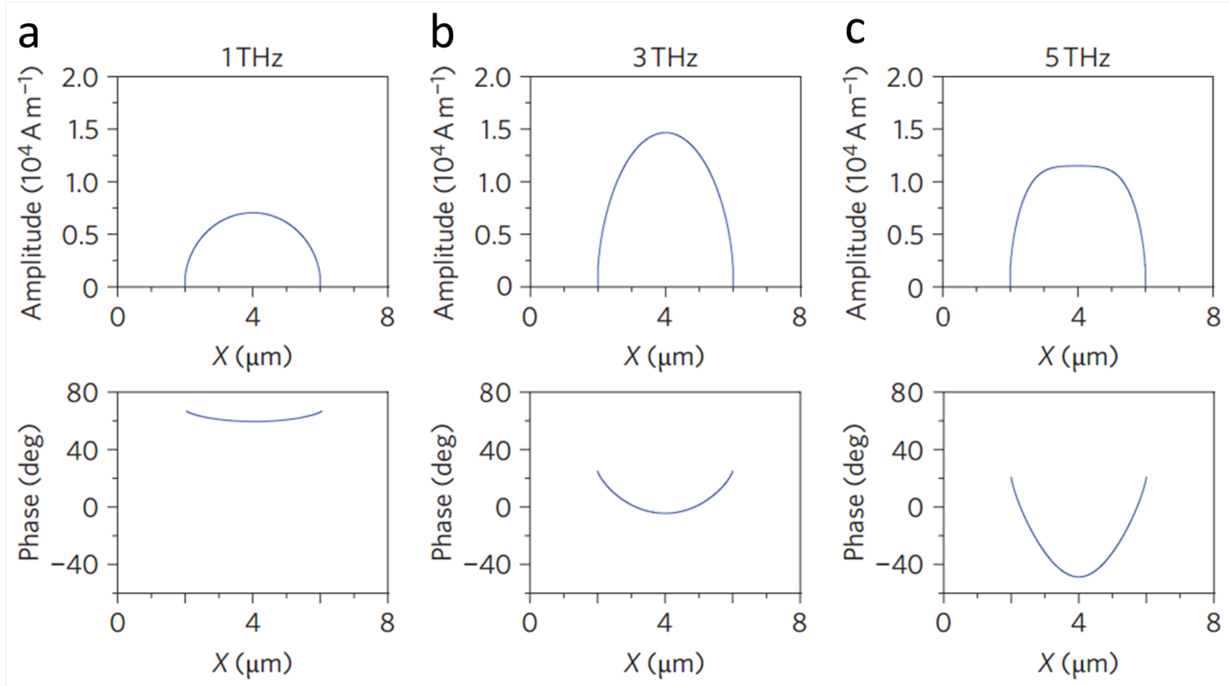

Figure 2.13: Simulation results for current density amplitude (upper panel) and phase (lower panel) of the device at frequencies below resonance (1 THz, a), at resonance (3 THz, b) and above resonance (5 THz, c). The charge carriers oscillate perpendicular to the graphene ribbons on terahertz irradiation. The oscillating current is highest at the plasmon resonance frequency. The relative phase of the oscillating current with reference to the incident electrical field also varies quickly and changes sign at the resonance frequency. Both are characteristics of a resonant excitation.

can be easily integrated with different gating configurations. In this study our gate-induced carrier concentration can be over 10^{13} cm^{-2} , and carrier concentration exceeds 10^{14} cm^{-2} has also been demonstrated by other researchers[37].

Combining these two effects, graphene provides a practical material to obtain strong light-plasmon coupling for room-temperature THz plasmonics.

2.8 Potential Applications of Graphene as Terahertz Metamaterials

In the broad definition, an optical metamaterial consists of structures with dimension much smaller than the relevant wavelength and exhibits optical properties distinctly different

from bulk materials. We believe that graphene microribbon array satisfy this definition, in that the ribbon width is much smaller than the THz wavelength, and unlike pristine graphene sheet, its plasmon resonance couples directly to free space THz radiation. Therefore, the graphene microribbon array studied here can be considered as the simplest form of graphene THz metamaterial, and the results demonstrated here can be generalized for designing more sophisticated metamaterials based on graphene for THz and far-infrared radiation.

Traditionally, meta materials are mostly made of metal to utilize its high charge density. However, the metal-based materials lack tunability since the charge density of metal cannot be tuned in a large range. This means once the structure is determined the properties of meta materials are determined. As we shown in this chapter, graphene as a 2D semimetal has great tunability of charge density by simply applying a gate voltage. Therefore graphene-based metamaterials has an advantage of in situ tunability compared to metal-based structure and holds great promise for meta material applications.

2.9 Summary

Our studies show that plasmon resonances in graphene can be controlled by both structural engineering and by electrostatic gating. The plasmons have remarkably strong coupling to electromagnetic radiations, absorbing over 13 % at the plasmon resonance for half a monolayer material at room temperature. The peak absorption at resonance can become even stronger with reduced plasmon linewidth, which is currently limited by the scattering rate as in the Drude conductivity. We expect that in higher quality graphene samples, the plasmon linewidth will be reduced in proportion to the increase in mobility. Given that our devices have mobility around 1000 $cm^2/V.s$, an order of magnitude improvement in mobility and plasmon resonance width should be achievable. Such plasmon resonances will be remarkably sharp, and a monolayer metamaterial will be able to absorb almost 100 % of THz radiation at the resonance frequency. The extraordinarily strong and broadly tunable plasmon resonances in graphene are promising for THz metamaterial devices, such as field-tunable THz modulators, filters, polarizers, and retarders using graphene micro-ribbon arrays. With novel metamaterial designs combined with electrical and optical excitations, even more exciting passive and active THz devices based on graphene could become possible.

Chapter 3

Photo-induced Doping in Heterostructures of Graphene and Boron Nitride

The design of stacks of layered materials in which adjacent layers interact by van der Waals forces[38] has enabled the combination of various two-dimensional crystals with different electrical, optical and mechanical properties, and the emergence of novel physical phenomena and device functionality[39][40][41][42][43][44][45]. In this chapter I will describe a photo-induced doping phenomenon in van der Waals heterostructures (VDHs) consisting of graphene and boron nitride layers. It enables flexible and repeatable writing and erasing of charge doping in graphene with visible light. We demonstrate that this photo-induced doping maintains the high carrier mobility of the graphene-boron nitride (G/BN) heterostructure, which resembles the modulation doping technique used in semiconductor heterojunctions, and can be used to generate spatially-varying doping profiles such as p-n junctions. We show that this photo-induced doping arises from microscopically coupled optical and electrical responses of G/BN heterostructures, which includes optical excitation of defect transitions in boron nitride, electrical transport in graphene, and charge transfer between boron nitride and graphene.

This chapter is adapted with permission from L Ju et al., “Photoinduced doping in heterostructures of graphene and boron nitride”, Nature nanotechnology **9**, 348 (2014). Copyright 2014 Nature Publishing Group.

3.1 Physical Properties of Graphene on Hexagonal Boron Nitride

Hexagonal boron nitride(BN) is a layered material that has similar structure to graphene. A single layer of BN can be obtained by replacing the two carbon atoms in graphene unit cell

by a boron atom and a nitrogen atom, preserving the honeycomb lattice. BN has a lattice constant that is 1.8 % larger than that of graphene. The inequivalence between boron and nitrogen atoms results in a bandgap of 6.4 eV[47] in hexagonal BN, thus high purity BN is transparent and sometimes called 'white graphene'.

Hexagonal boron nitride was introduced into the graphene community in 2010 by researchers at Columbia University[48]. They showed that mobility of graphene transferred to BN substrate has about one order of magnitude higher mobility than that of graphene on SiO_2 substrate. This is due to the atomic flat nature of exfoliated hBN surface and the suppression of dangling bond-induced electron hole puddles in graphene[41]. Therefore the incorporation of hBN into graphene devices brought graphene research to a new era where many intrinsic properties of graphene can be studied.

Recent scanning probe and electrical transport studies have revealed moiré patterns[39][40][41], new Dirac points[42] and the Hofstadter butterfly[43][44][45] in graphene/boron nitride (G/BN) heterostructures, hence convincingly demonstrating that the interaction between the constituents of van der Waals heterostructures (VDHs) plays a key role in their properties. Light matter interactions in VDHs can also exhibit new phenomena arising from the coupling between the layered constituents. A recent work exploited the strong optical absorption of WS_2 and the tunability of graphene electrodes to engineer graphene/WS_2/graphene heterostructures for flexible photovoltaic devices with high quantum efficiency[49]. The photo-induced modulation doping effect that will be presented later in this chapter is another example of the interesting interactions between graphene and boron nitride.

3.2 Fabrication of the Graphene/Boron Nitride Heterostructure

Most of the samples were fabricated with the transfer technique developed by P.J. Zomer et al (ref. 50) and using standard electron beam lithography. Graphene epitaxially grown on BN flakes[51] are also investigated and they exibited similar photo-induced doping behaviour. The schematic of the transfer process is shown in Fig. 3.1. We employed an h-BN thickness of 10-110 nm and a SiO_2 thickness of 285 nm as the dielectrics for electrostatic gating. The transfer technique for creating graphene-hBN heterostructures involves exfoliation of graphene onto a transparent substrate, exfoliation of hBN onto a SiO_2/Si wafer, alignment and contact of graphene and hBN, and removal of the transparent substrate. The technique generally works for transferring other thin materials from a transparent substrate onto an arbitrary flat substrate. hBN flakes are deposited on SiO_2/Si wafers by exfoliation of high quality hBN crystals. AFM was used to determine the thickness, but after observation of a few samples, it became possible to estimate the thickness just by looking at the color of the BN.

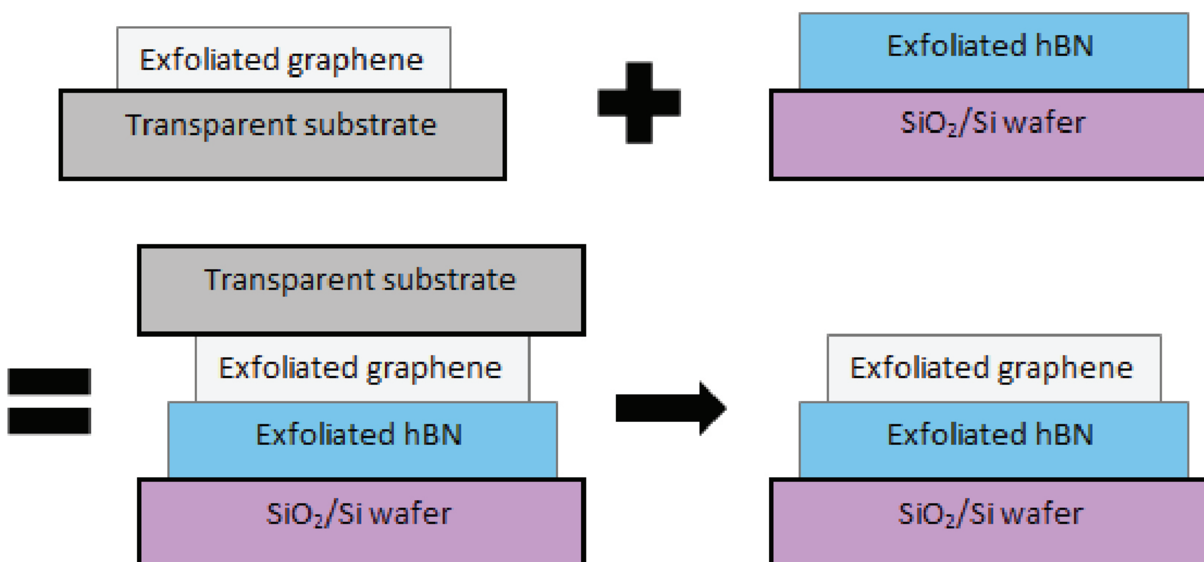

Figure 3.1: Schematic of the transfer process of graphene onto BN. Graphene and BN flakes are exfoliated by the scotch tape method onto a transparent substrate and SiO_2/Si substrate respectively. They are aligned under an optical microscope and made in contact. The transparent substrate is removed by mechanical separation and chemical dissolution.

After exfoliation and identification of hBN flakes, the sample is annealed with air in a quartz tube furnace at 500 °C for 3 hours. The annealing completely removes adhesive residue left by the exfoliation tape without damaging the hBN surface, as confirmed by AFM. The active reactant in the annealing is the oxygen in the air, which has been shown to be effective for cleaning adhesive residue.

The transparent substrate is prepared from a glass slide, transparent scotch tape, and a layer of methyl methacrylate monomer (MMA), also named as acrylic resin. Scotch tape is carefully pressed onto a glass square (i.e. adhesive in contact with the glass). After cutting off the excessive tape draging over the edge of the square, the top surface of the tape is washed with acetone followed by IPA. A 10 % solution of acrylic resin (Elvacite 2550) in MIBK is spin-coated at 1300 rpm for 1 minute onto the tape surface, covering the tape with a uniform layer of acrylic with thickness around 1 μm.

Graphene is exfoliated onto the acrylic face of the transparent substrate. For the searching of graphene, an optical microscope in reflection mode is used with the graphene surface upwards. An especially important technique for the searching of graphene was the application of black tape on the bottom glass surface of the substrate in order to reduce the amount of scattered light entering the microscope. This increased the contrast of graphene by nearly

2 times and allowed for the search and identification of monolayer graphene flakes. After selection of an appropriate graphene flake, a razor blade is used cut a small 2-3 mm square island of tape/acrylic with the selected graphene in the center.

We use a micromanipulator microscope stage with a bottom stage that can move in the horizontal plane and a top stage that can be moved in all three dimensions. A simple resistive heating plate is attached to the bottom stage and held by two screws. The hBN on SiO_2/Si wafer is placed onto the heating plate (not turned on yet). The graphene and hBN is repeatedly aligned and lowered until one corner of the acrylic/tape is in contact with the underlying wafer. The two screws holding the heating plate are carefully adjusted to change the tilt of the wafer until the entire right edge of the acrylic/tape is in contact with the wafer. After a final check of the graphene/hBN alignment, a weight (100 grams) is put onto the left side of the microscope slide and then the height of the top stage is adjusted until the entire acrylic/tape is in contact with the wafer. The heating plate is heated to 110 °C for 8-10 minutes, allowing the acrylic to soften and conform to the shape of the graphite and hBN pieces between the acrylic and the wafer.

A razor blade is wedged between the wafer and the glass base of the transparent substrate. The acrylic glues the tape to the wafer very strongly, and the separation is almost always between the transparent tape and the glass base. Since separation occurs far away from the graphene/hBN, there is very little strain introduced to the sample and as a result, it is very unlikely for samples to crack during the separation process. What remains on top of the hBN and graphene is a small square of acrylic and transparent tape. After immersing the sample in methylene chloride for 30 minutes, the layer of acrylic dissolves, leaving the transparent tape to float away. The sample is then immersed in acetone followed by IPA, and then gently blown dry with a nitrogen gun.

E-beam lithography is used to deposit gold electrodes on the graphene. After completion of the lithography, the sample is annealed in a 350 °C Ar/H_2 environment for 3 hours to remove any organic residues left by the transfer process and the lithography. An example of finished sample is shown in Fig. 3.2.

3.3 Experimental Observation of Photo-Induced Doping in Graphene/Boron nitride

Experimentally we found that graphene electric transport in the G/BN heterostructure can be modified upon illumination even with an incandescent lamp, as we show in Fig. 3.3. We monitor the graphene resistance R while sweeping the bottom gate voltage V_g with different optical excitation conditions. The graphene resistance shows a sharp peak at the charge neutral point (CNP) with $V_g \sim 0$ V and has little hysteresis in the absence of

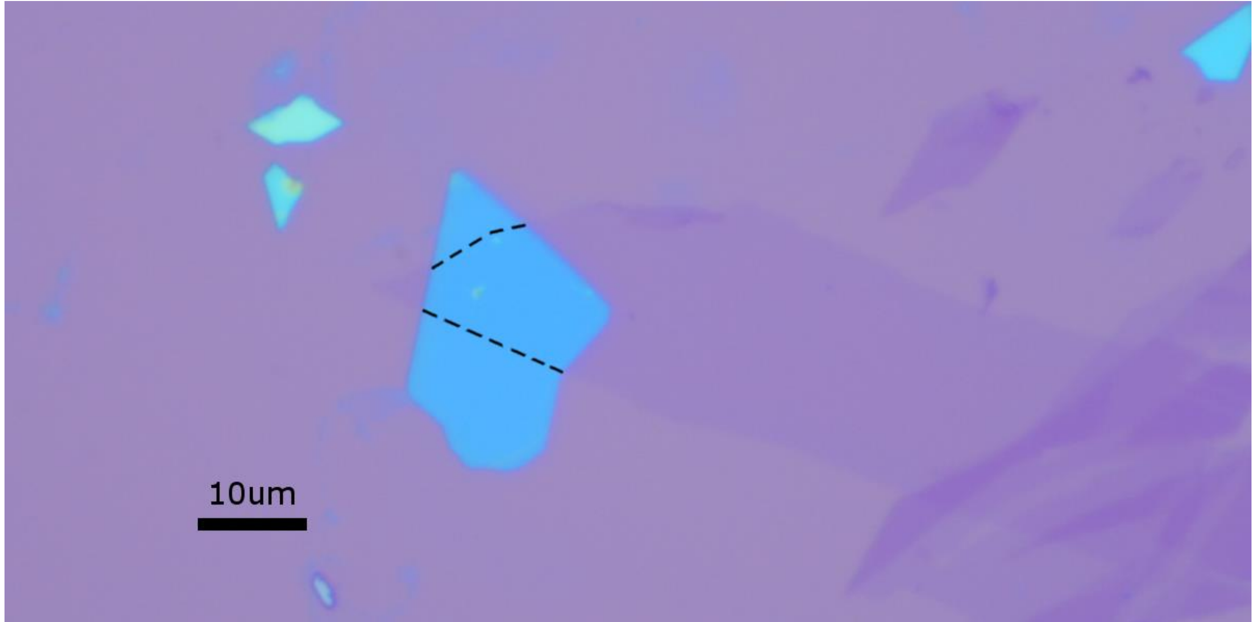

Figure 3.2: Optical microscope image of exfoliated graphene transferred on exfoliated hBN. The blue flake is exfoliated BN while the faint semi-transparent flakes are monolayer and few layer graphene. Dashed lines on BN indicate borders of monolayer graphene area.

light exposure (Fig. 3.3a), similar to that observed in many graphene field-effect-transistor devices[48][50][1][2]. The transport behavior becomes completely different, however, when the device is exposed to moderate optical illumination.

In Fig. 3.3b, we plot the gate-dependent graphene resistance when the device is under the illumination of an incandescent lamp. V_g is swept from 70 V to -70 V and then back to 70 V. We observe that R increases initially until it reaches the CNP at V_g=0 V. Afterwards, R remains constant when V_g sweeps to negative voltages, as if the gating is not working. This is in striking contrast to the behavior without light illumination (Fig. 3.3a). When the V_g sweep is reversed, R drops quickly as if the reversal point (rather than V_g=0 V) is the CNP.

To further investigate this intriguing photo-induced response, we measured $R(V_g)$ with the light switched off and on alternately as V_g sweeps from 20 V to -50 V at a constant rate of 0.05 V/s (Fig. 3.3c). We observed conventional $R(V_g)$ behaviour when the light is off (with V_g= 20 V to -5 V), and R increases quickly and becomes pinned at the CNP value whenever light is switched on. Once the light is switched off, R decreases from the CNP value with more negative V_g.

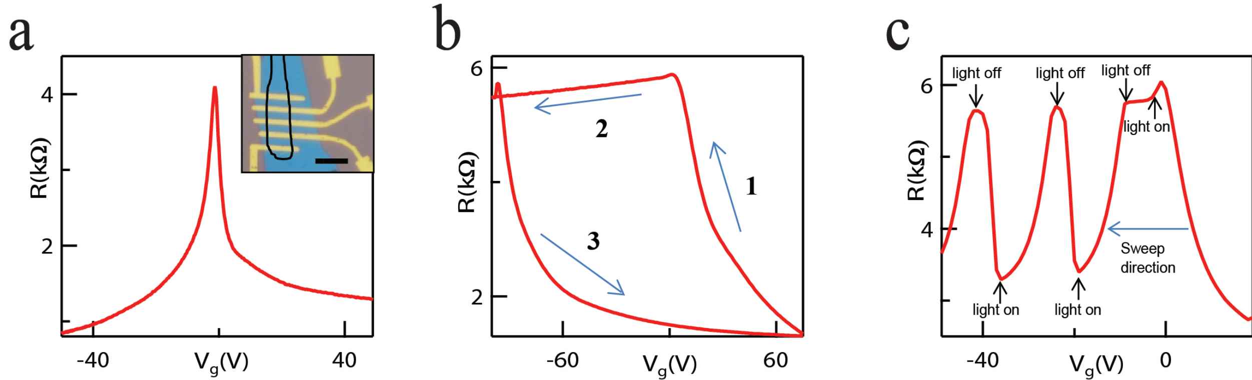

Figure 3.3: Experimental observation of photo-induced modulation doping effect in G/BN heterostructures. a, Representative $R(V_g)$ data in a G/BN device showing a sharp resistance peak at V_g =0 V without light exposure. Inset: Optical micrograph of device, with graphene (outlined by the solid line) on a BN flake (blue, 18 nm thick) and contacted by chrome/gold electrodes. Scale bar, 8 μm. b, $R(V_g)$ trace as V_g sweeps from 70 V to -70 V and then back to 70 V with the device exposed to light. Light illumination changed the gating behaviour in the graphene, with negative gating becoming ineffective and the graphene resistance remaining at the CNP value. The BN flake here and in c is 100 nm thick. c, $R(V_g)$ trace when V_g sweeps from 20 V to -50 V and the light illumination is alternately switched on and off. Graphene resistance is pinned at CNP value whenever light is switched on at negative V_g and shows normal gating behaviour when light is switched off.

Although the photo-induced responses at different illumination conditions seem quite complicated, they can be understood with a very simple phenomenological model illustrated in Fig. 3.4. In this model, visible light induces a positive charge distribution in BN that completely screens the negative V_g, and the positive charges in BN are fixed when the light is switched off. This model explains qualitatively all of our experimental observations: the backgate is screened and graphene is pinned at CNP with light on and a negative V_g, and this V_g sets the CNP when light is off or V_g becomes less negative. When the V_g is removed, it results in a stable n-type doping in graphene. Although the photo-induced doping in G/BN is not permanent, we found it can last for many days at room temperature when the device is kept in a dark environment. Additionally, it can be easily erased in minutes with light illumination at an intensity $\sim$ 10 μW/μm^2. Further measurements show that a p-type doping can also be induced in G/BN by optical excitation at a positive V_g, but the dynamics is orders of magnitude slower. We have measured 27 G/BN samples and all exhibit the photo-doping effect. However, the exact dynamics of photo-doping can vary significantly upon both the BN flake thickness and the batch of the parent BN crystals.

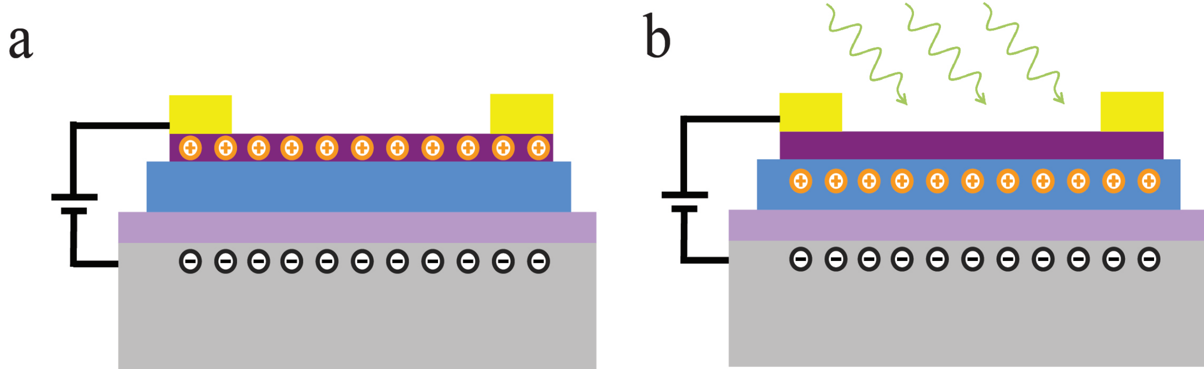

Figure 3.4: Charge distribution in the G/BN device when light (green arrows) is switched off (a) and on (b). Positive charges accumulate in BN under light illumination at negative V_g, which effectively screens the backgate and keeps graphene at the CNP. Yellow, Cr/Au; purple, graphene; blue, BN; violet, SiO_2; grey, Si.

3.4 Microscopic Mechanism of Photo-Induced Doping

Next we study the microscopic processes responsible for the photo-induced modulation doping in G/BN. First, we need to identify the electronic states being excited by photons that lead to photo-doping effects. The initial optical excitation might take place at the G-BN interface (by exciting graphene or special interface states[52][53]) or inside BN. These two cases can be differentiated by examining the photo-doping dynamics with different BN thicknesses, because the photo-doping rate will have a positive correlation with BN thickness if electronic states in BN are excited, and it will be independent of BN thickness if interface states are excited. Figure 3.5 shows the experimental data for G/BN heterostructures with 20 nm and 110 nm BN flakes. These two BN flakes were exfoliated from the same scotch tape to ensure that they have the same physical properties. At t=0 s we set V_g= -30 V for the 20 nm BN sample (-40 V for the 110 nm BN sample to ensure the same doping density) and switch on the light. We observe that the dynamic resistance increase (or the photo-doping rate) is much faster in 110 nm BN sample than that in 20 nm BN sample under the same illumination condition. Results for more samples are plotted in the inset of Fig. 3.5a. We observe a systematic increase of photo-doping rate in thicker BN flakes, although a significant variation of the doping rate is observed. Our results suggest that optical excitation of electronic states inside BN initialises the photo-induced doping in G/BN heterostructures. The typical light power density we used is 0.1-1 μW/μm^2, which is three orders magnitude lower than that required to observe photo-doping originated from interfacial charge traps in SiO_2[52][53].

Previously BN was always considered as an inert substrate because it has a bandgap of

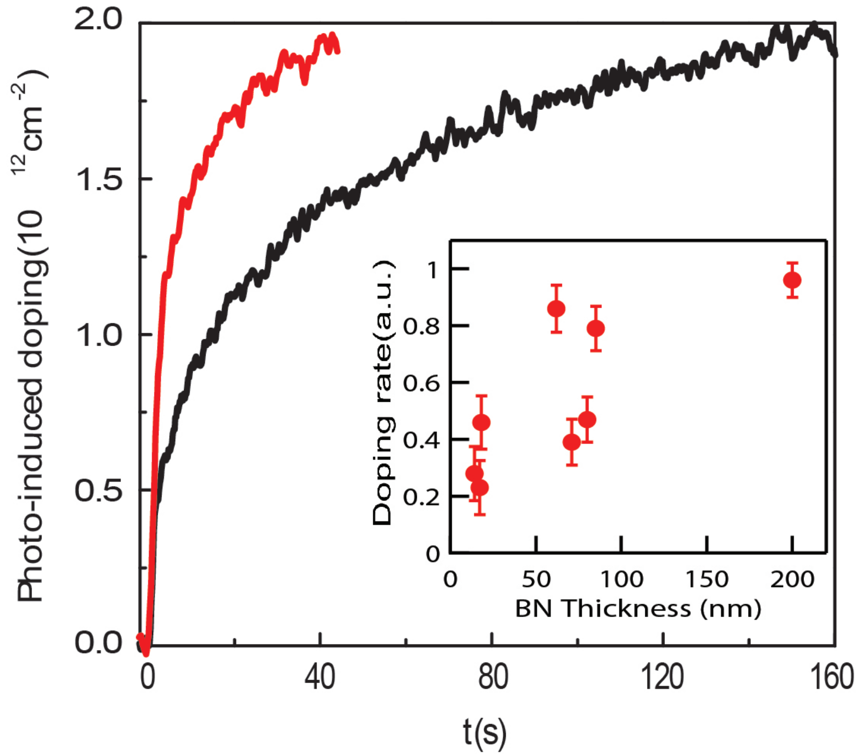

Figure 3.5: Dynamics of photo-induced modulation doping effect. Photo-induced doping density as a function of time in two devices under the same illumination condition and gating electrical field. Black and red traces correspond to BN flake thicknesses of 20 nm and 110 nm, respectively. Evidently, the rate of photo-doping is significantly higher in the G/BN device with a thicker BN flake. Inset: Photo-doping rate in more samples, showing that the rate increases systematically with BN thickness, although it fluctuates significantly from sample to sample. The error bars are defined by the error in determining δV_g, which is within ± 0.2 V.

6.4 eV (ref. 47). Therefore, it is quite surprising that the photo-induced doping in G/BN originates from optical excitation of electronic states in BN. Obviously visible photons used in the experiment cannot excite the bandgap transitions, but they can excite defect states in BN. In Fig. 3.6 we illustrate a physical picture of the photo-induced doping in G/BN starting with defect states in BN. Graphene is initially hole-doped at a negative V_g in the dark environment, and an electric field emanates from graphene to silicon. Upon optical illumination, electrons of donor-like defects in BN are excited by photons to the conduction band. These excited electrons can be mobile and move towards graphene following the existing electrical field and then enter graphene. The ionised defects are positively charged and localised in BN, and they effectively screen the backgate. The process continues until the electric field in BN vanishes and graphene becomes charge neutral, as we observed experimentally. Because

the ionised defects are within the BN flake, which are on average tens of nanometers away from graphene, they introduce minimum extra scattering in graphene[54]. Additionally, correlations between these charged defects can reduce the scattering even more[55]. Negatively charged defects can also be generated in BN if optical excitation excites acceptor-like defects in BN at a positive V_g. However, the process is much slower in our experiment, presumably due to a much lower concentration of acceptor-like defects in BN.

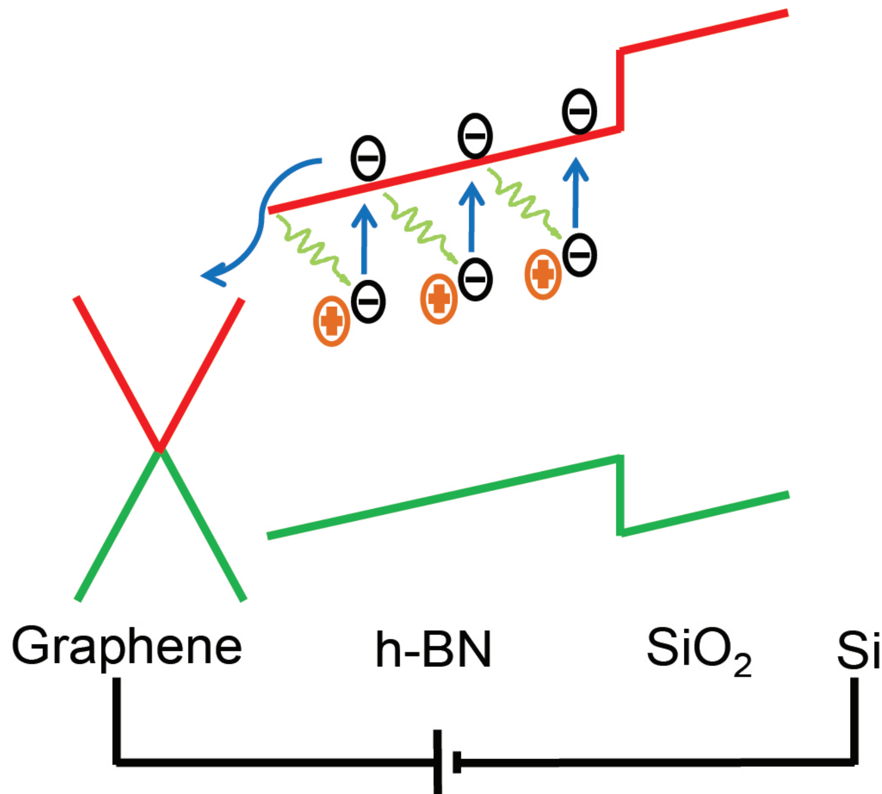

Figure 3.6: Schematics of the band structure of the graphene/BN heterostructure and illustration of the photo-doping mechanism. Optical excitation first excites electrons from defects in BN. Red (green) lines represent the conduction (valence) band. The excited electrons move into the graphene under the applied gate electrical field, and the positively charged defects lead to modulation doping in the graphene when the light and V_g is off.

With this microscopic understanding, we can employ the photo-induced doping in G/BN as a tool to study the nature of the BN defect states. The optical absorption cross-section of defect states in BN is proportional to the generation rate of ionised defects, which can be measured sensitively through their effect on graphene electrical transport. Moreover, we can probe selectively the donor-like defects and acceptor-like defects by setting V_g to be negative and positive, respectively. Figure 3.7 shows the photo-doping rate for acceptor-

like defects (red trace) and donor-like defects (green trace) as a function of photon energy. We found that photo-doping rate, which is proportional to optical absorption of the defect states, varies with the defect type and the excitation energy. For donor-like states, we found that the absorption cross-section keeps increasing in the experimental spectral range (up to 2.6 eV). A similar trend is observed for acceptor-like states, but the photo-doping rate is approximately two orders of magnitude lower. These spectral dependences suggest deep donor and acceptor defect levels close to the middle of BN bandgap. Previous theoretical work found that the dominating donor and acceptor absorption resonance are from nitrogen vacancy at 2.8 eV and carbon impurity (substituting a nitrogen atom) at 2.6 eV[56]. These resonances are slightly beyond our experimental spectral range, but are consistent with the observed strong rise at below 2.6 eV. Greater spectrum range in the higher photon energy regime will be necessary to directly probe the absorption resonances from the defect levels.

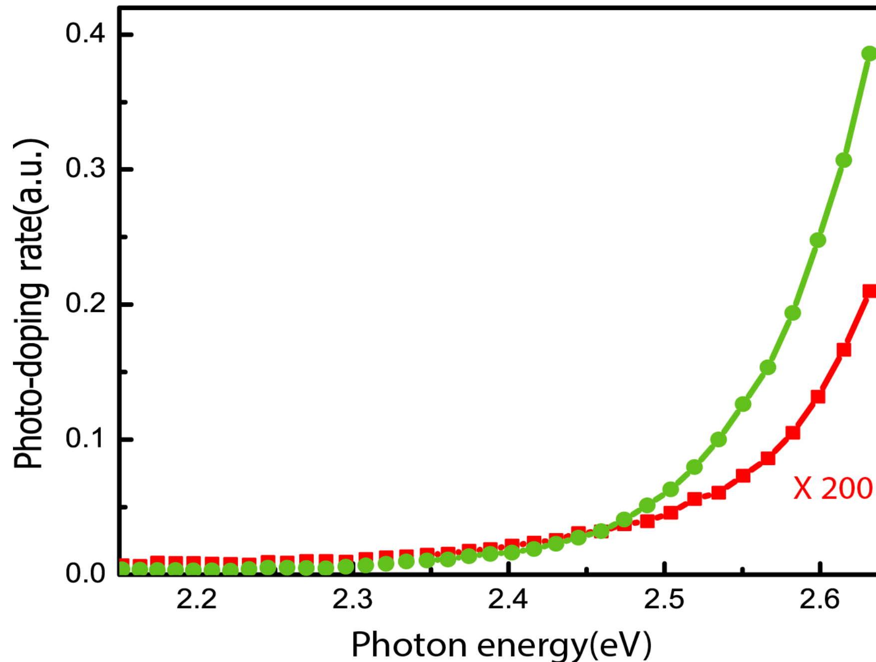

Figure 3.7: Optical absorption spectrum of defect states in h-BN. The green trace shows that the photo-doping rate (and therefore the absorption cross-section) from donor states keeps increasing in the experimental spectral range (up to 2.6 eV). A similar trend is observed for acceptor-like states (red trace), but this photo-doping rate is about two orders of magnitude lower. These spectral dependences suggest deep donor and acceptor defect levels close to the middle of the BN bandgap. The BN flake is 60 nm thick.

3.5 Similarity to Modulation Doping Technique

We show excellent transport properties of graphene with photo-induced doping in Fig. 3.8a and b. We control the doping level by exposing the device to light at fixed V_g until the resistance stabilises and then take an $R(V_g)$ scan with the light off. We used V_g set points at 0(before doping),-10,-20,-30,-40 and -50 V, and plot the resulting $R(V_g)$ traces in Fig. 3.8a. The photo-induced doping leads to a shift of CNP to the V_g set points, corresponding to an n-doping concentration. Remarkably, the peaks of all $R(V_g)$ remain as sharp as the pristine sample. This is in striking contrast to doping induced by adsorbed atoms, where a significant increase of $R(V_g)$ peak width accompanies higher doping concentrations[57][58][59]. Figure 3.8b quantifies the charge transport properties by plotting the charge density fluctuations δn and mobilities μ close to the CNP for different photo-induced doping concentrations. Evidently, the photo-induced doping preserves the excellent electrical transport properties of G/BN. The electron mobility μ remains almost constant over the entire doping concentrations. δn exhibits similar behavior, and increases only marginally while the doping level increased to 3×10^{12} cm^{-2}.

This maintained high mobility is a reminiscent of the modulation doping first developed for high quality semiconductor heterojunctions[60][61], where dopants are separated from the conducting channel to prevent charge scattering. The BN flakes we used are in general tens of nanometers. Thus the positive dopants (in BN) are away from the n-type conducting channel (in graphene), their effect of coulomb scattering on graphene electrons is reduced a lot. This is in substantial contrast to the interface charges in graphene/SiO_2 originated from dangling bonds of SiO_2, which is within 1 nm from graphene. As we mentioned previously at the beginning of this chapter, BN serves as an excellent substrate for graphene transport. Now we demonstrate that the photo-doping maintains such advantage which makes it potentially useful for both scientific research and applications.

3.6 Potential Applications of Photo-Induced Doping

We demonstrate the flexibility of photo-induced doping to control the doping profile in G/BN optically in Fig. 3.9. We create a high quality graphene pn junction by exposing one region of the sample to light with V_g set at -20 V (see inset of Fig. 3.9). The resulting $R(V_g)$ trace taken with light off, is shown in Fig. 3.9 (blue line). Two distinct peaks are observed with similar heights that are separated by -16 V. This transport behaviour is characteristic of a graphene pn junction[62][63][64]. This photo-induced doping can last for days if the device is kept in a dark environment, or it can be erased by exposing the sample to white light while V_g=0 V. The erasure process usually requires 50 times higher illumination dosage (power density $\times$ exposure time) than the doping process. The red trace in Fig. 3.9 shows the $R(V_g)$ curve after the erasing process, and it exhibits a single sharp peak centred at V_g=0 V as in the pristine device.

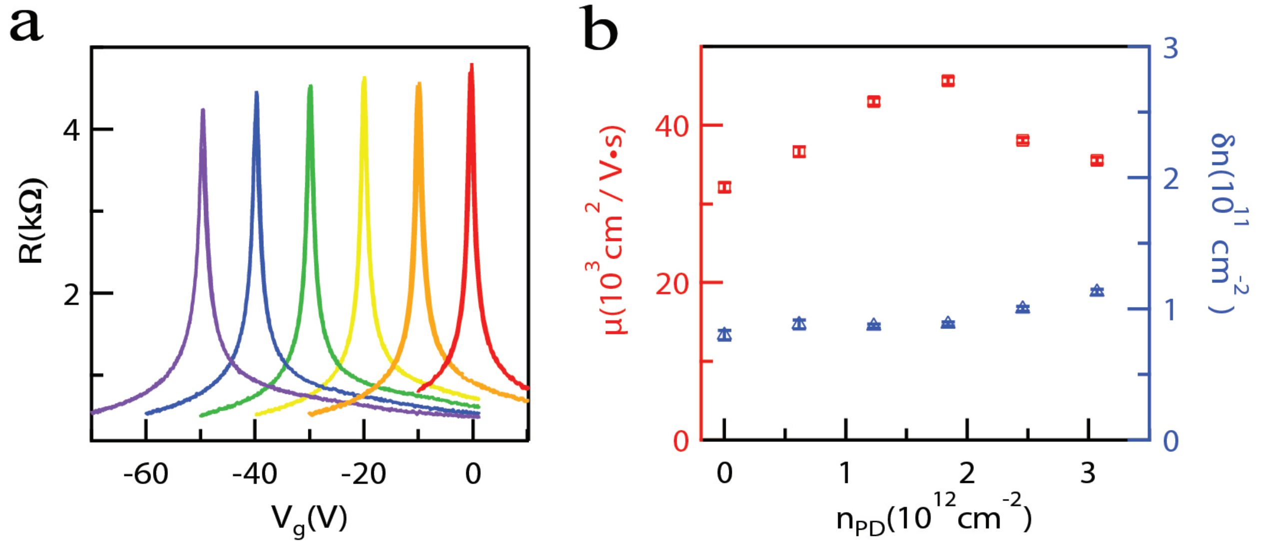

Figure 3.8: Transport characteristics of G/BN after photo-induced modulation doping. a, $R(V_g)$ traces displaying high-mobility charge transport in G/BN devices with photo-induced modulation doping. Red trace: Behaviour of a pristine sample. The other traces were acquired after photo-doping, with the graphene CNP set at V_g = -10, -20, -30, -40 and -50 V, respectively (from right to left). b, Quantitative determination of electron mobility μ (squares, left axis) and charge density fluctuation δn at the CNP (triangles, right axis) from $R(V_g)$ traces in a, at different photo-induced doping density n_{PD}. Error bars represent $\pm$ 1 s.d.

Combining the photo-induced modulation doping with photolithography techniques can enable scalable fabrication of high mobility graphene devices with arbitrary doping pattern. This fabrication scheme does not require any photoresist because G/BN itself is the photo-sensitive media. Additionally, the device is rewritable by controlling light illumination. It offers distinct advantages over alternative techniques in creating graphene pn junctions that require nontrivial multi-step fabrication process that reduces sample quality[62][63] and/or generates irreversible doping[65].

3.7 Summary

In this chapter, I demonstrated an unexpected strong photo-induced doping effect in G/BN heterostructures and provide a microscopic description of its origin. This phenomenon manifests the importance of coupling between different components of van der Vaals heterostructures. Technologically, the photo-induced doping effect resembles the modulation doping technique in modulating the carrier concentration without sacrificing the high elec-

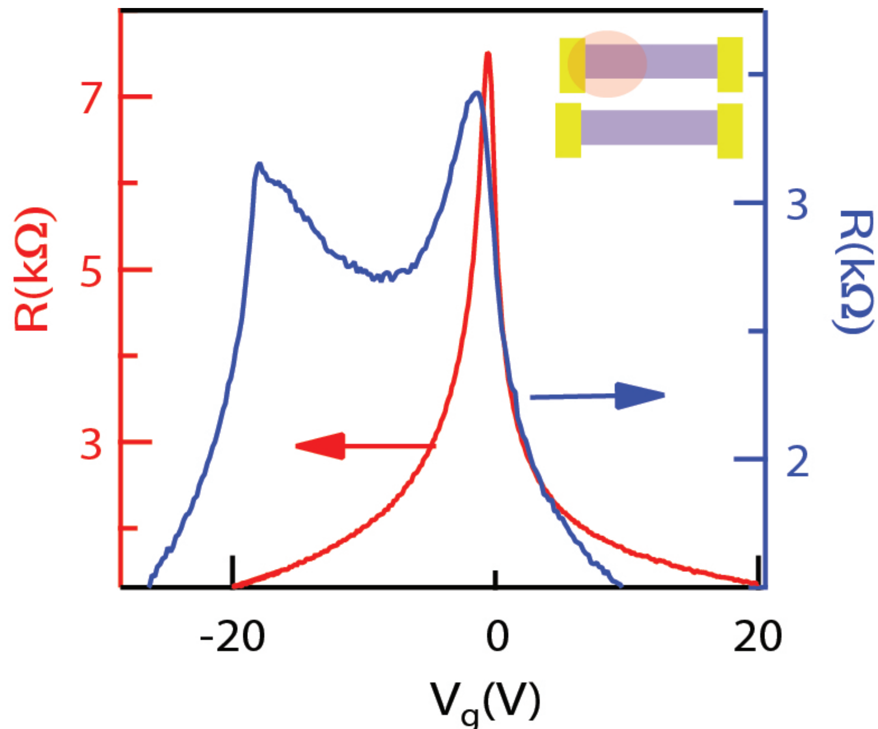

Figure 3.9: Generation and erasure of a pn junction in a G/BN heterostructure with light. Inhomogeneous photo-doping can be established by illuminating part of the G/BN device with light at V_g = -20 V (inset), which results in an $R(V_g)$ response typical of a graphene pn junction (blue trace). Subsequent exposure of the device to light at $V_g = 0$ V erases the inhomogeneous doping and recovers the $R(V_g)$ response of pristine graphene (red trace).

trical mobility. Such technique can enable flexible fabrication of graphene devices through controlled light exposure as in photolithography. Moreover, it allows for repeatable writing and erasing of the doping features, and preserves the very high mobility of G/BN. This new and simple technique of creating inhomogeneous doping in a high mobility graphene device opens the door for novel scientific studies and applications.

Chapter 4

STM Study of Defect States in Boron Nitride

In Chapter 3 we described the photo-induced doping in graphene/boron nitride heterostructures and conclude that defect states in boron nitride is the origin of this photo-induced charge transfer. The measurement we did previously is electron transport, which is basically a global measurement of the material properties. Although we have gained pretty good sense of the charge transfer process as an emsemble effect of defect states at different locations, local information of individual defects is also very important for the understanding of boron nitride. Considering the trend of using 2D materials as building blocks for materials engineering of controlled properties, understanding defects in boron nitride, as the only large band gapped 2D insulators, is particularly important for the 2D materials community. Scanning tunneling microscopy and spectroscopy is a powerful experimental approach to study local properties of materials like what is needed in this context.

The work described in this chapter is a natural extension of my collaboration with Jairo Velasco Jr. on the photo-induced doping story. It is also an example of numerous collaborations between the Wang group and the Crommie group. The STM measurement was done by Dillon Wong and Jairo Velasco Jr. in Prof. Crommie's group. The sample fabrication is the same as described in Chapter 3 which was first demonstrated by me and undergrad students in the Wang group, and later broadcasted to the graphene community here in Berkeley. I was involved intellectually in initializing this experiment and providing new points of view throughout the whole project.

4.1 Basics of Scanning Tunneling Microscopy/Spectroscopy

Scanning tunneling microscopy/spectroscopy is a very powerful tool in study the surface properties of materials. It is first demonstrated by researchers of IBM Zürich in 1981[66].

Figure 4.1 [67] illustrates the schematic and working principle of STM. A metal tip is placed a few above a conductive sample surface. When a electrical voltage is applied between the tip and the sample, tunneling current can be induced between them due to the quantum tunneling effect. This tunneling current is determined by two factors and thus result in two typical modes of operation. Firstly, the tunneling current is very sensitive to the spatial seperation between tip and sample. Mathematically tunneling current decays exponentially with tip-sample distance. At the same time, the electronic structure of the material also affects the tunneling current through the local density (LDOS). The tunneling current is proportional to the LDOS thus providing valueable information about the material.

The first function of STM is to do microscopy. The tunneling current can be maintained as a constant with a feedback loop that includes a piezoelectric transducer as shown in Fig. 4.1. In this mode one can map out the surface topography by reading the height of tip as scanning over the surface. Because of the sensitivity of tunneling current to tip-sample distance[68], this microscopy method has sub-nanometer resolution in the z-direction. Since the current is collected/emitted by the lowest atom at the apex of the tip, atomic resolution in lateral directions can be achieved. Thus the imaging of individual atom in a crystal lattice is within the reach of STM. One subtlety in the interpretation of STM topographs is that the tunneling current depends both on the tip-sample distance and the sample density of states. So STM topography is a convolution of geometric and electronic effects when the sample electronic structure is not homogeneous across the surface.

Another function of STM is spectroscopy. The bias voltage determines the relative alignment of tip Fermi level and sample Fermi level, thus blocking/open tunneling channels at specific energy level. By differentiating the tunneling current with tip bias, one can get the differential conductance (dI/dV) which is proportional to the LDOS. dI/dV as a function of bias voltage provides a spectrum of LDOS at different energy levels. Practically, an AC voltage is added on the tip and the induced tunneling current is probed by a lockin amplifier to enhance the signal/noise level. One can also do dI/dV map by scanning over the surface to study the inhomogeneity of samples. The imaging of charged defects in boron nitride we are going to talk about in this chapter is basically achieved in this way.

4.2 Extending the Scope of STM Study

Defects play a key role in determining the properties of most materials, but imaging them at the atomic scale can be difficult. Although scanning tunneling microscopy (STM) has a history of characterizing individual point defects in conductors[69], semiconductors[70][71][72][73][74][75], and ultrathin films[76], such characterization has eluded experimentalists for intrinsic bulk insulators. Here we report the imaging and manipulation

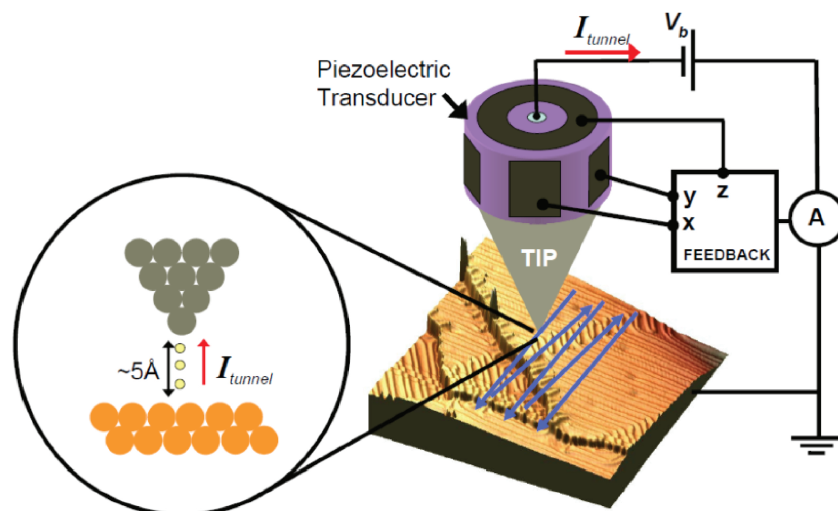

Figure 4.1: A schematic demonstration of the structure and working principle of an STM. This is adapted from Ref. 67.

.

of native defects in an intrinsic bulk boron nitride (BN) insulator via STM. Normally, this would be impossible due to the lack of a conducting drain path for electrical current.

We overcome this problem by employing a graphene/boron nitride heterostructure, which exploits the atomically thin nature of graphene to allow visualization of defect phenomena in the underlying bulk hexagonal boron nitride. Basically the graphene capping layer serves as a sensing media, where the electronic stucture is a manifestation of the charged defects embedded in the boron nitride substrate. This allows for the imaging of charged defects. Moreover, graphene can have charge exchange with the closest defects in certain conditions, which allows for the determination of the defect energy levels and manipulation of defect states. In this sense, what is going to be shown later in this chapter presents a new functionality of STM and enable the study of local properties of individual defects in a bulk insulator. Therefore the role of graphene and boron nitride has an interesting twist here: boron nitride was used to modify the electronic properties of graphene and allow for studies of its more intrinsic properties; but in this chapter, the main focus is the properties of BN, while graphene gives us an indispensible hand.

4.3 Imaging of Charged Defects in Boron Nitride Through Graphene

Visualization of individual BN defects was facilitated by capping a BN crystal with a monolayer of graphene. Fig. 4.2a shows a typical STM topographic image of our graphene/BN

heterostructures that is consistent with previous imaging of graphene on BN[40][41] (a 7 nm moiré pattern can be seen, as well as long-range height fluctuations spanning tens of nanometers). Localized shallow dips and protrusion are also visible (Δz < 0.1 $\overset{\circ}{A}$). More revealing, however, are the differential conductance (dI/dV) maps shown in Fig. 4.2b. Striking new phenomena are visible in this data. We observe randomly distributed bright (high dI/dV) and dark (low dI/dV) circular dots 20 nm in diameter that have varying degrees of intensity. Another common feature, as seen in the right edge of the map in Fig. 4.2b, is a sharp ring structure with an interior that does not obscure the moiré pattern. Close-up topographic studies of these defects reveal unblemished atomically resolved graphene honeycomb structure with occasional slight dips or a protrusion having $|\Delta z| < 0.1$ $\overset{\circ}{A}$. Maps obtained at numerous locations with numerous tips across three different devices replicate these observations.

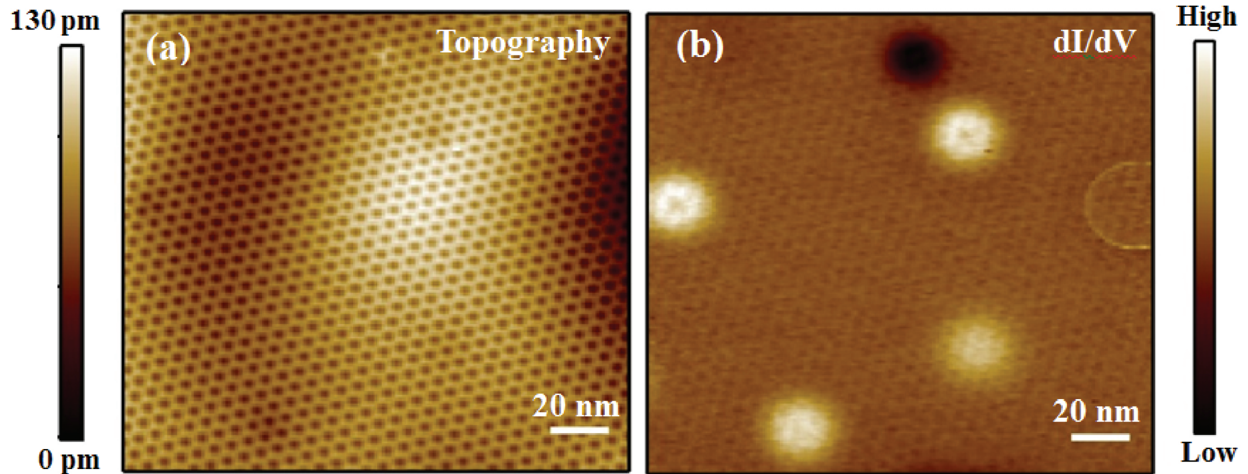

Figure 4.2: STM topography and corresponding dI/dV map for a graphene/BN device. a. STM topographic image of a clean graphene/BN area. b. dI/dV map (I = 0.4 nA, V_s = -0.25 V) acquired simultaneously with (a) exhibiting various new features: bright dots, a dark dot, and a ring.

We now discuss the origin of the dot and ring defects observed in our dI/dV maps. Three general scenarios are possible: (i) Adsorbates bound to the surface of graphene, (ii) adsorbates trapped at the interface between graphene and BN, and (iii) intrinsic defects within the insulating BN substrate. Our data implies that (iii) is the correct scenario, as follows: First we rule out scenario (i) because weakly bound adsorbates would have a higher height profile than the topographically small features observed[77][78], and would also likely get swept away by the STM tip when it is brought close enough to observe the graphene

honeycomb structure. Strongly bound adsorbates in scenario (i) would also likely have taller height profiles as seen for other graphene adsorbates and should disrupt the graphene honeycomb lattice (which was not observed). Also, strongly bound adsorbates should lead to changes in the graphene spectroscopy due to formation of localized bonding states[79], which are not seen. Scenario (ii) can be ruled out because an adsorbate trapped beneath graphene would cause a bump in graphene at least an order of magnitude larger than the $\Delta z < 0.1\ \mathring{A}$ feature observed here[80]. We would also expect a trapped adsorbate to locally delaminate the graphene from the BN substrate, thus disrupting the moiré pattern, which is not seen.

Scenario (iii), intrinsic charged BN defects, is thus the most likely explanation of the defects observed here. Polycrystalline BN has been shown to host several varieties of charged defects, as seen from electron paramagnetic resonance[81] and luminescence experiments[82][83], as well as theoretical investigations[84]. In those studies the most abundantly reported defects were N-vacancies, which were shown to act as donors, and C impurities substituted at N sites, which were shown to act as acceptors. Secondary ion mass spectroscopy studies of single crystal high purity BN synthesized at high pressure and temperature have identified oxygen and carbon impurities[85]. Comparison between optoelectronic experiments[86][46] of high purity single crystal BN and recent theoretical work[87] shows that the nature of the BN crystal defects is consistent with the observations of C impurities and N-vacancies. Such defects, when ionized, could induce the bright and dark dots observed in graphene/BN via a graphene screening response[56] (Figs 4.2 and 4.3). The fact that these defects are embedded in the BN explains why the dots have such small topographic deflection, as well as why the graphene lattice and moiré pattern are not disrupted, and also why no new states arise in the graphene spectroscopy[77][78]. Variations in the intensity of bright and dark defects are explained by BN defects lying at different depths relative to the top graphene layer.

4.4 Determination of Charge Types of the Dot-like Defects

Figs 4.3a and b show higher resolution dI/dV maps of representative bright and dark dot defects. These maps show clearly that the graphene moiré pattern is not obscured by the defects. To determine the effect of these defects on the electronic structure of graphene, we performed dI/dV spectroscopy at varying distances from the dot centers (each spectrum was started with the same tunnel current I and sample bias V_s). These data are plotted in Figs 4.3c and 2d for the bright and dark dots, respectively. The spectra are characteristic of undamaged graphene[88], but show an electron/hole asymmetry that is dependent on the tip position relative to the center of a defect. In Fig. 4.3c, for example, we see that dI/dV ($V_s > 0$) increases as the tip approaches the bright-dot center. Fig. 4.3d shows the opposite trend

as seen by the decrease in dI/dV ($V_s > 0$) as the STM tip approaches the dark-dot center. These basic trends were seen for all bright and dark dot defects, regardless of intensity and tip-height variation. These observations can be understood by recalling that dI/dV reflects the graphene local density of states (LDOS). The distance-dependent enhancement of dI/dV above the Dirac point ($V_s \approx$ -0.17 V) as the tip nears a bright dot in Fig. 4.3c can therefore be interpreted as arising from the attraction of negatively charged Dirac fermions to the dot center. We thus conclude that the bright dot in Fig. 4.3a reflects a positively charged defect in BN[77][89]. Similarly, the distance-dependent reduction of dI/dV above the Dirac point in Fig. 4.3b arises from the repulsion of negatively charged Dirac fermions from the defect. We thus conclude that the dark dots are negatively charged[77][89].

4.5 Determination of Energy Levels of the Ring-like Defects

We now focus on the ring defects, as displayed at the right edge of Fig. 4.2b. We find that the ring radius depends on the values of V_s and back-gate V_g. Fig. 4.4 shows that the ring radius changes from 2 nm to 11 nm as V_g is changed from $V_g = 17$ V to $V_g = 9$ V (for a constant $V_s =$ -0.3 V). Fig. 4.5 shows the dependence of the ring radius on V_g for various V_s values (denoted by distinct symbols). This data was obtained by measuring the ring radius from dI/dV maps taken at the same location as Figs 4.4a and 4.4b, but with different V_s and V_g configurations. Although the precise ring radius depends on the sharpness of the STM tip[72], the qualitative behavior shown in Fig. 4.5 is typical of the vast majority of ring defects observed here. In general, for fixed V_s, the ring radius increases with decreasing V_g until a critical back-gate voltage ($V_c = 6 \pm 1$ V) is reached, upon which the ring vanishes.

It is possible to extract quantitative information regarding the electronic configuration of BN defects from the STM dI/dV signal measured from the graphene capping layer. This can be performed for the ring defects by analyzing the gate (V_g) and bias (V_s) dependent ring radius, shown in Fig. 4.5. Similar rings have been observed in other systems and have been attributed to the charging of an adsorbate or defect[72][78][15][90][91]. Because the ring in Fig. 4.4 is highly responsive to the presence of the STM tip and displays no charge hysteresis, we expect that it lies in the topmost BN layer and is strongly coupled to the graphene electronic structure. The STM tip is capacitively coupled to the graphene directly above the defect through the equation $|e|\,\Delta n = C(r)\,V_{tip}$, where Δn is the local change in graphene electron density, $C(r)$ is a capacitance that increases with decreasing lateral tip-defect distance r, and V_{tip} is the tip electrostatic potential ($V_{tip} = V_s$ + constant). For the dI/dV maps in Fig. 4.4, $V_{tip} < 0$, so the electrostatic gating from the tip lowers the electron density of the (n-doped) graphene directly beneath the tip. Fig. 4.6 schematically depicts the local electronic structure of the graphene immediately above the defect when r is large and V_g is set such that the defect level is filled and carries negative charge. As the

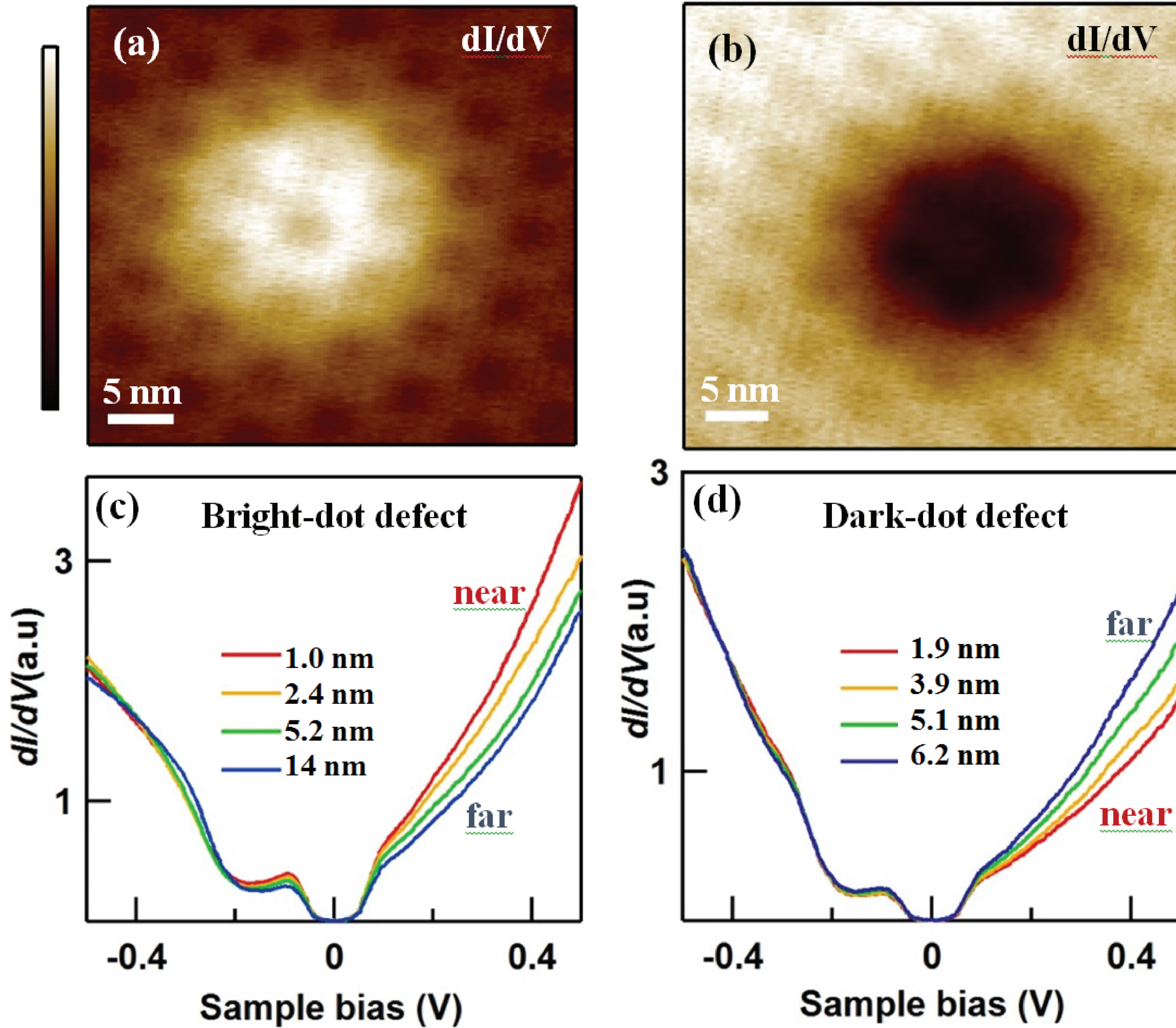

Figure 4.3: dI/dV maps and spatially dependent dI/dV spectroscopy determines defect charge state. a and b, dI/dV maps ($I = 0.4nA$, V_s = -0.3 V, V_g = 5 V) for bright and dark dot defects. c. dI/dV spectroscopy (initial tunneling parameters: I = 0.4 nA, V_s = -0.5 V, V_g = 20 V) measured on graphene at different lateral distances from the center of the bright dot in a. d, same as c, but for the dark dot in b. From the distance-dependent dI/dV spectroscopy, it can be deduced that a and b represent positively and negatively charged defects in BN, respectively.

tip approaches the defect, $C(r)$ increases, and thus Δn becomes more negative. Eventually the defect level crosses the Fermi level (and switches to a neutral state) when the tip is at a distance R away from the defect, thus causing a perturbation in the tunnel current that

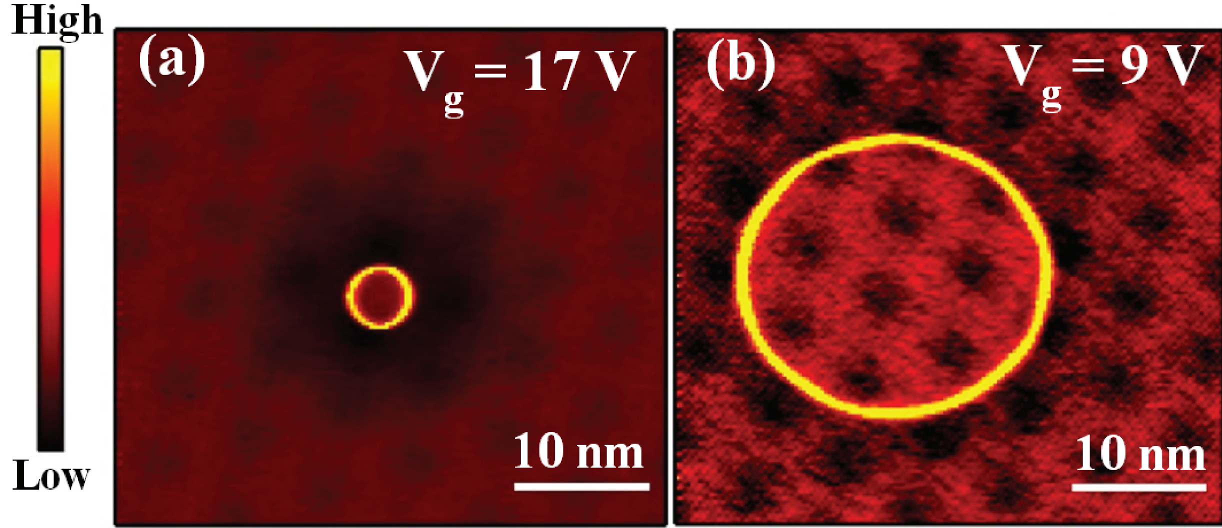

Figure 4.4: dI/dV maps of the ring defect at different measurement conditions. a. dI/dV maps (I = 0.4 nA, V_s = -0.3 V) of a ring defect. b. dI/dV of the same ring defect as in a at back-gate voltages V_g = 17 V and V_g = 9 V.

leads to the observation of a ring of radius R. Fig. 4.6b shows the case ($r < R$) where the defect is in a neutral charge state through interaction with the tip. The energy level of the defect can be found by tuning V_g such that the Fermi level matches the defect level in the absence of the tip. This will cause the radius of the charging ring to diverge. As seen in Fig. 4.5, this occurs for the observed ring defects when $V_g = 6 \pm 1$ V, thus resulting in a defect level approximately 30 ± 10 meV above the graphene Dirac point energy (since the Dirac point energy can be measured with respect to the Fermi level), which is expected to be $\sim$ 4 eV below the BN conduction band edge[92]. Interestingly, this is similar to a previously observed carbon substitution defect level[82], suggesting that the ring defect arises from a carbon impurity.

4.6 Manipulation of Defect States in Boron Nitride

Additional microscopic information regarding the observed BN defects can be obtained by directly manipulating their charge state with the STM tip. Similar manipulation has been performed previously to switch the charge state of defects in semiconductors[93] as well as adatoms on top of ultrathin insulating films[76][94], but this type of STM-based manipulation is unprecedented for defects inside bulk insulators. Fig. 4.7 shows a dI/dV map exhibiting numerous charged defects. In order to manipulate the charge state of the observed BN defects, the STM tip was positioned 1 nm over the center point of this area and

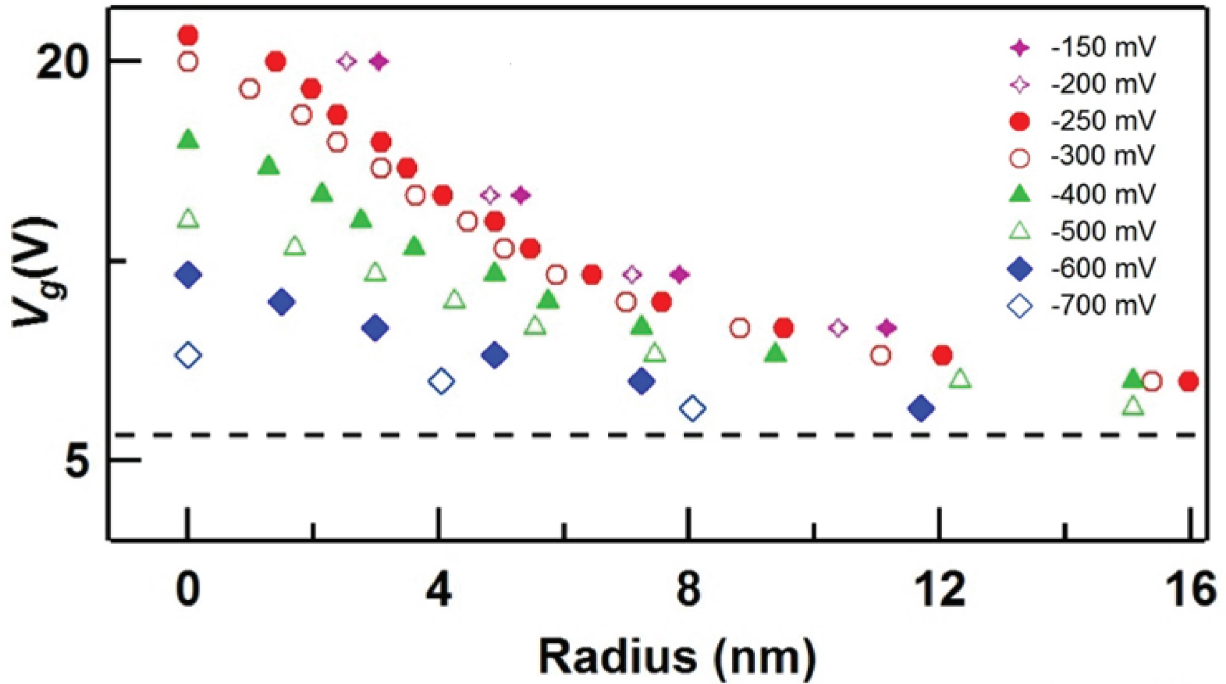

Figure 4.5: Ring radius R for different V_s (denoted by distinct symbols) and V_g.

a bias of $V_s = 5$ V was applied for 10 seconds. After applying this voltage pulse, a dI/dV map was acquired over the same region at low bias, as shown in Fig. 4.7b. Fig. 4.7c shows the same region after similar application of a second pulse. Inspection of Figs 4.7b and c shows that the BN defect configurations are significantly altered by application of such voltage pulses. The defects are seen to reversibly switch between charged and neutral states, as well as between states having opposite charge. To highlight this behavior, we denote changes to defect states (compared to the preceding image) with colored arrows. A red arrow signifies the disappearance of a charged defect, a blue arrow represents the appearance of a charged defect, and a green arrow indicates where a defect has changed the sign of its charge. We find that defects that disappear after a tip pulse always reappear in the same location after subsequent tip pulses. Additionally, dark dots tend to switch into metastable neutral states (i.e. disappear) at a higher rate than bright dots. Ring defects, as well as the darkest and brightest dots, remain unchanged by tip pulses.

This tip-induced manipulation of BN defects can be explained by electric-field-induced emission of charge carriers from BN defect states. By tilting the local potential landscape, the STM tip causes charge carriers to tunnel through the ionization barrier between different defects, charging some while neutralizing others. This accounts for the disappearance and reappearance of the dots in the same location, which cannot be described by defect migration

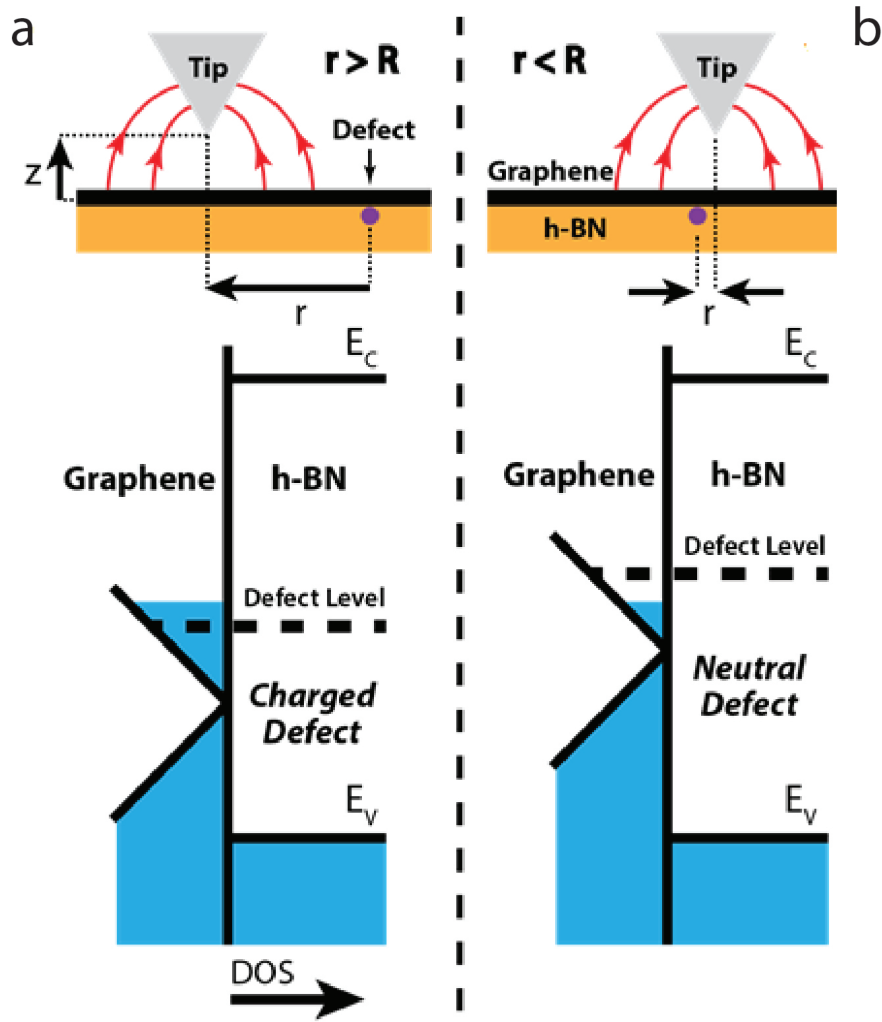

Figure 4.6: Schematic model (energies not to scale) for ring formation due to charge transfer between graphene and a defect in the top layer of BN. When the distance r between the tip and the defect is larger than R, the defect level is filled and negatively charged. When $r < R$, the local gating effect of the tip lowers the local electron density such that the Fermi level is below the defect level, neutralizing the defect. For negative tip potentials and n-doped graphene, R increases as reduced V_g shifts the unperturbed defect level closer to the Fermi energy.

through the BN lattice. In addition, the observation of a higher rate of switching for the dark dots (acceptors) than bright dots (donors) suggests it is more energetically favorable for neutral acceptors to emit holes than for neutral donors to emit electrons; hence the acceptor states are likely closer to the valence band than the donor states are to the conduction band. Since the rings, as well as the darkest and brightest dots, never change under tip pulses, we

surmise that they are in the topmost layer of BN and in direct electrical contact with the graphene. Their charge states thus depend only on graphenes local chemical potential and show no hysteresis with electric field. The defects that switch into new metastable charge states (i.e., exhibit hysteresis) must thus be in lower BN layers, out of direct contact with the graphene.

4.7 Summary

In conclusion, we have shown that a single graphene capping layer enables STM imaging and manipulation of individual point defects in an insulating bulk BN substrate. We are able to identify the charge state of individual defects, and we have quantitatively extracted the energy level location for one species of defect (suggesting that it is a carbon impurity). We find that voltage pulses applied to our STM tip enable ionization, neutralization, and even toggling of the charge state for defects in BN. This new method of using an atomically thin conducting capping layer to probe and control defects in bulk insulators might be extended to other insulator/defect systems previously inaccessible to STM, such as diamond with nitrogen-vacancy centers.

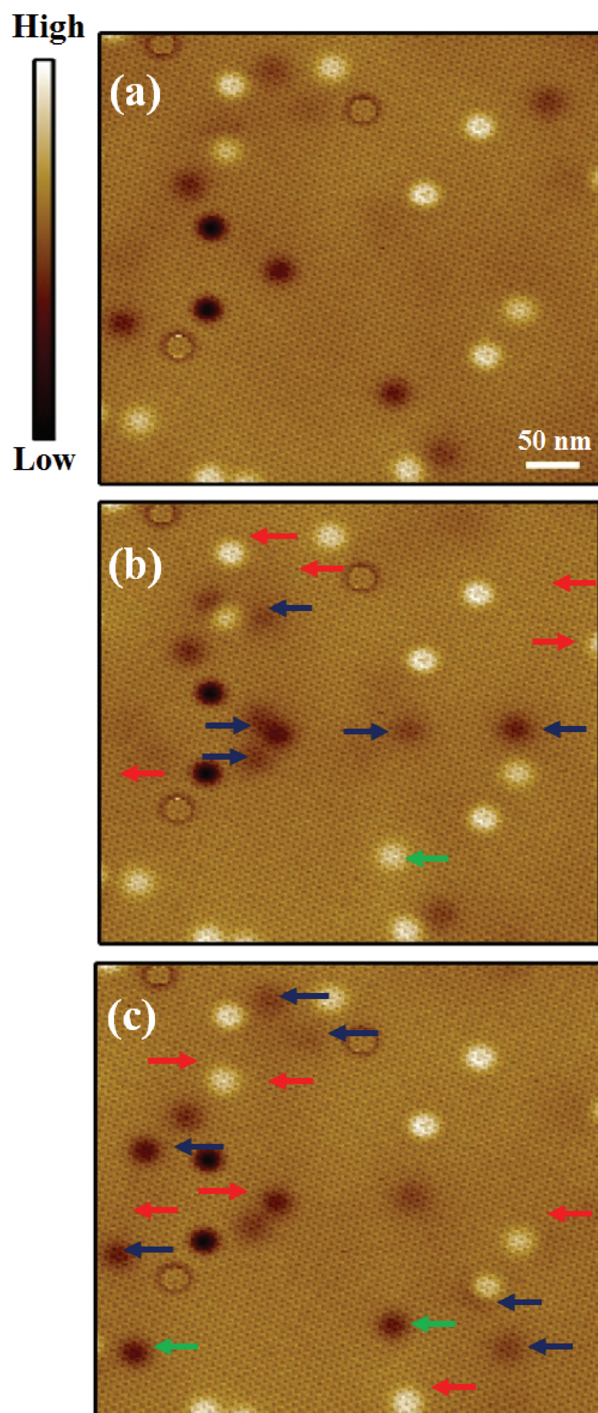

Figure 4.7: Manipulating defects in BN with an STM tip. Tip pulses having $V_s = 5$ V and $\delta t = 10$ seconds are used to toggle the charge states of the dots. a. dI/dV map (tunneling parameters: $I = 0.4$ nA, $V_s =$ -0.25 V) of graphene/BN reveals various dots and rings. b. dI/dV map of same region after a tip pulse is applied at the center of region in a. c. dI/dV map of same region after another tip pulse. Red arrows mark the disappearance of dots relative to the previous image, blue arrows mark the appearance of dots, and green arrows mark dots that have changed their charge signs.

Chapter 5

Topological Valley Transport at Bilayer Graphene Domain Walls

Electron valley, a new degree of freedom analogous to spin, can lead to novel topological phases in bilayer graphene (BLG). A tunable bandgap can be induced in BLG by an external electric field[7][6][8][9][10], and such gapped BLG are predicted to be symmetry-protected topological insulators featuring quantum valley Hall effects and chiral edge states[95][96]. Observation of such chiral edge states, however, is challenging because they are unstable against atomic scale defects at real graphene edges[97]. Recent theories[98][96][99][100] have shown that domain walls between AB and BA stacked BLG can support protected chiral edge states of quantum valley Hall insulators. In this chapter I will show the first experimental observation of nearly ballistic conducting channels at BLG domain walls. We employ near-field infrared (IR) nanoscopy[101][102][103] to image in situ BLG layer-stacking domain walls on device substrates, and incorporate the domain walls into dual-gated field effect transistors. Unlike single-domain BLG that show gapped insulating behavior under a vertical electrical field, BLG domain walls feature one-dimensional (1D) valley-polarized conducting channels with a ballistic length of $\sim$ 400 nm at 4 K. Such topologically protected 1D chiral states at BLG domain walls open up exciting opportunities for exploring unique topological phases and valley physics in graphene.

This chapter is adapted with permission from L. Ju et a, Topological valley transport at bilayer graphene domain walls, Nature (2015). doi:10.1038/nature14364. Copyright 2015 Nature Publishing Group.

5.1 Topologically Protected Boundary States at Electrically-Induced and Structurally-Induced Bilayer Graphene Domain Walls

Hexagonal two-dimensional crystals, such as graphene and transition metal dichalcogenides, exhibit a pair of degenerate bands at the K and K′ valleys in momentum space. The valley electrons are characterized by non-trivial Berry curvatures, which give rise to anomalous quantum Hall states in graphene[104] as well as valley Hall effects, the valley counterpart of spin Hall effects[105][106]. BLG provides an attractive platform to explore topological valley physics[107]: a tunable semiconductor bandgap can be induced in BLG using a vertical electrical field, and different topological phases can exist in gapped BLG[108][95][98][109][110][111]. In particular, BLG with an electric field-induced bandgap are predicted to be quantum valley Hall insulators, where counter-propagating chiral electrons with opposite valley index exist at their boundaries. Such 1D chiral states are topologically protected as long as there are no inter-valley scatterings generated by atomic scale defects.

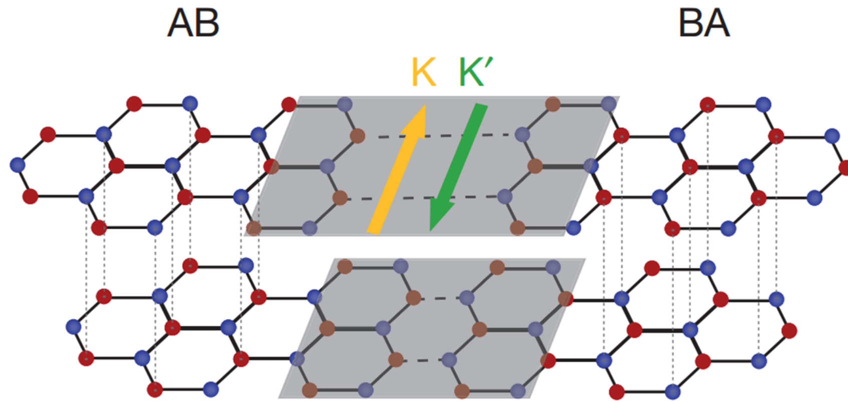

Figure 5.1: Illustration of a domain wall (shaded area) between AB- and BA-stacked BLG domains. The yellow (green) arrow indicates one-dimensional conducting channel at the domain wall from K-valley (K′-valley) electrons.

Domain walls between AB- and BA-stacked BLG provide an attractive platform to realize 1D chiral boundary states of quantum valley Hall insulators. The integrated Berry curvature of BLG valence bands for each valley is characterized by a quantized valley Chern number[98][96][99], the sign of which depends both on the direction of the vertical electrical field and the layer stacking order. Martin et al (Ref. [98]) first proposed topological domain walls between band-inverted BLG insulators generated by opposite vertical electrical fields.

Experimental realization of such electric-field walls, however, is extremely challenging. An alternative approach is to exploit different stacking orders. The AB- and BA-stacked BLG under the same vertical electrical field represent two distinct topological phases with opposite valley Chern numbers. The stacking boundary between AB and BA domains form a layer stacking domain wall (Fig. 5.1). Valley-polarized chiral electrons are predicted to flow along such a domain wall in gapped BLG, where K and K′ valley electrons propagate in opposite directions.

5.2 Introduction to Near Field Infrared Nanoscopy

In optical experiment, usually the beamspot diameter of a focused optical beam is limited by the diffraction limit due to the wave nature of electromagnetic wave. This limit is usually on the order of the wavelength. As a result, one cannot map out the optical conductivity of materials with spatial resolution less than the wavelength. But in many cases, fine structures in the material can result in inhomogeneity of its optical properties on a much small scale like the stacking boundary we are going to talk about later. In order to break the diffraction limit and see finer features of materials, one has to utilize schemes other than using a lens.

One of the sub-diffraction limit imaging techniques is the near field nanoscopy enabled by a metal tip. The experimental scheme is illustrated in Fig. 5.2, where light is focused from far-field onto the tip and backscattered light is collected by a detector. By scanning the tip over the surface of a sample, the optical response is recorded as a function of position thus giving a map of the optical properties.

The imaging process can be decomposed into two steps. First in the excitation step, light is focused onto the metal tip to excite the material. As a result of the high charge density and thus strong plasmon responses in metal, metal has large conductivity for frequency ranging from DC to optical frequencies. When light shines on the metal tip, the electric field is greatly enhanced in space around the tip. This enhancement decays exponentially to the tip radius as one goes away from the tip. Therefore the material right beneath the tip will feel a much stronger electric field than other parts of the sample. The collection step can be thought as a reverse process of the excitation step. The coupling efficiency of radiation from different locations in the sample to the tip is exactly the same as the enhancement factor for excitation. This means only the radiation of local oscillators right next to the tip can be efficiently coupled to far field and collected by the detecor.

Combing these two-fold enhancement of excitaion and collection, the sigal from the vicinity of the tip stands out from the bulk background and makes the sub-diffraction limit imaging possible. In the case of our experiment, the wavelength is $\sim 6\ \mu$m while the tip radius is ~ 25 nm. Thus a spatial resolution 250 times better than the far field focusing is obtained.

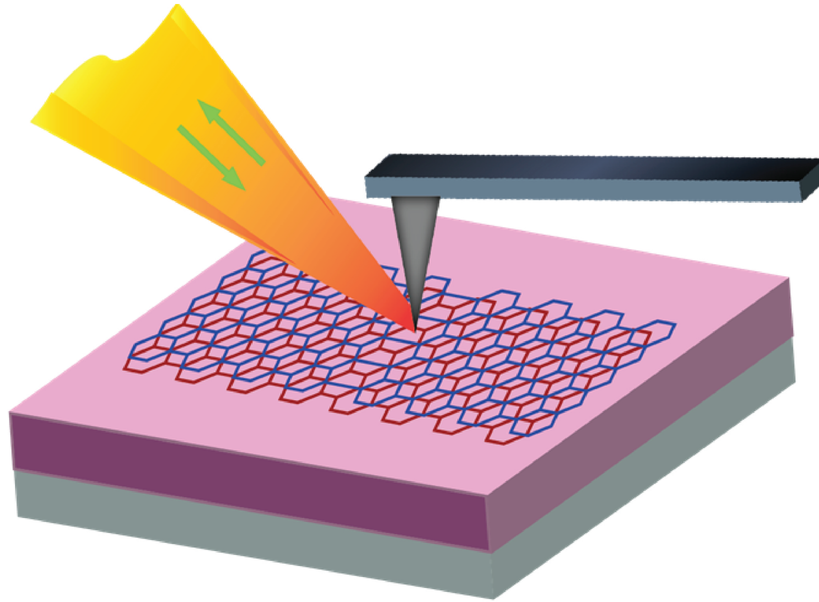

Figure 5.2: Illustration of the near-field infrared nanoscopy measurement of graphene on a SiO_2/Si substrate. IR light at 6.1 μm was focused onto the apex of a metal-coated AFM tip and the backscattered IR radiation was collected and measured by an HgCdTe detector in the far-field.

This is the key to this whole experiment of demonstration of the topological valley transport in bilayer graphene.

5.3 Near Field Nanoscopic Imaging of Domain Walls in Bilayer Graphene

Recent electron microscopy studies show that AB-BA domain walls with a width of several nanometers exist naturally in suspended BLG[112][113], but suspended BLG samples are hardly compatible with bandgap control and transport measurements. Here we use a novel approach to image in situ AB-BA domain walls in exfoliated BLG on SiO_2/Si substrates which allow us to demonstrate topologically protected charge and valley transport along such boundaries for the first time.

Few layer graphene were mechanically exfoliated on 280 nm thick SiO_2/Si substrates[114], and the layer thickness is determined through optical contrast measurements. To identify AB-BA layer stacking domain walls in BLG we employ near-field IR nanoscopy[101], as illustrated in Fig. 5.2. IR light at 6.1 μm was focused onto the apex of a metal-coated atomic force microscope (AFM) tip with radius of curvature r $\approx$ 25 nm, and the scattered

IR radiation was collected and measured by an HgCdTe detector in the far field. The tip-enhanced IR scattering provides a local probe of the material IR responses with ~ 40 nm spatial resolution. The AB and BA stacked BLG, being inversion symmetric to each other, have exactly the same electronic bands and IR absorption. The local bandstructure of the domain wall, however, is strongly modified relative to the bulk and exhibits different IR contrast. Figure 5.3a and b display, respectively, AFM topography and near-field IR nanoscopy images of the same BLG on a SiO_2/Si substrate. The BLG topography shows a step height of ~ 1 nm, consistent with the bilayer thickness. Within the bilayer flake the topography is featureless with a height fluctuation of less than 0.2 nm. In the near-field IR nanoscopy image, however, distinct features appear in the BLG: multiple bright lines extend across the BLG flake and terminate at the edges. These bright lines in the IR image indicate a change of local infrared conductivity in the BLG. No corresponding features can be discerned in the topography image (Fig. 5.3a), which excludes the possibility of surface contaminations or graphene folding along these lines. We attribute these local IR response changes to AB-BA domain walls in BLG.

We further provide a microscopic picture for the contrast we see in Fig. 5.3b in the AB-BA domain wall region. The infrared contrast of the domain wall arises from its different electronic structure and infrared conductivity from the AB-stacked bilayer graphene. I will not go into an exact description of the local band structure of a domain wall. Instead, a qualitative model of the domain wall region can be envisioned by considering it as two randomly stacked monolayers of graphene. Such randomly stacked graphene has electronic structure similar to that of two separated monolayers close to the Dirac point[115], and its infrared conductivity can be approximated by $2\sigma_{monolayer}$. The AB-stacked bilayer graphene, on the other hand, has an infrared conductivity of sbilayer. The optical conductivities of both monolayer and AB-stacked bilayer graphene have been well established in the literature[116]. At the infrared wavelength of 6.1 mm, the value of $2\sigma_{monolayer}$ is about 20% higher than that of $\sigma_{bilayer}$, which can qualitatively explain the bright infrared contrast of the domain walls observed in our studies.

5.4 Near Field Nanoscopic Imaging of Monolayer and Trilayer Graphene

To confirm that the bright lines within the BLG are layer stacking domain walls, we systematically examined near-field IR images of exfoliated graphene flakes of different layer thicknesses. Figure 5.4a, 5.4b, and 5.5a show IR nanoscopy images of representative monolayer, bilayer, and trilayer graphene flakes, respectively. The IR images of monolayers, like that in Fig. 5.4a, always show homogenous responses within the flake, although bright features can be observed parallel to the edges due to excitation of graphene plasmons. The

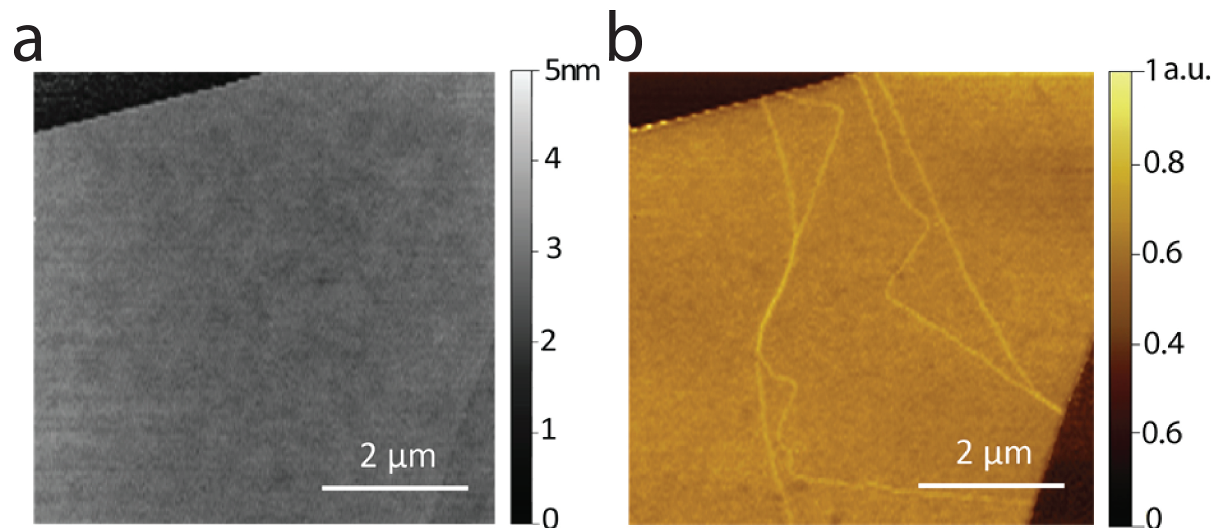

Figure 5.3: IR nanoscopy imaging of AB-BA domain walls in exfoliated bilayer graphene. a, AFM topography map of a BLG sample on a SiO_2/Si substrate showing no surface wrinkles or defects. (The small triangle area at the bottom right corner corresponds to a graphene monolayer.) b, Near-field infrared (IR) nanoscopy image of the same BLG sample as in a. Bright line features across the BLG flakes are observed, which are absent in the topography image. These bright lines arise from AB-BA domain walls in BLG because the domain walls have different local electronic structure and IR responses.

absence of any structural domain boundary in monolayers is consistent with the high quality of exfoliated samples. In bilayer graphene, about 30 % of the exfoliated flakes show bright lines across the interior region of graphene like those in Fig. 5.4b, and areas between these lines have the same contrast. We identify these bright lines as AB-BA domain walls because they are the only 1D structure that exists in bilayer but not monolayer graphene. This identification is further bolstered by the IR images of graphene trilayers as that shown in Fig. 5.5a. Bright lines extending through the graphene flakes are also observed, but unlike graphene bilayers, the domains separated by the bright lines can have different IR contrast. This is because more domain stacking orders can exist in the trilayer, such as ABA, BAB, or ABC stacking. Although ABA and BAB domains are inversion symmetric to each other and have the same electronic structure, ABC domains have distinctively different bandstructures[8], IR responses[117], and Raman spectra[118]. Therefore a domain wall between ABA- and ABC-stacked trilayers will separate two domains with different IR contrast in the near-field IR image, as seen in domain I and II in Fig. 5.5a. In addition, we performed micro-Raman measurements on domains I and II, and show the corresponding spectra in Fig. 5.5b. It is apparent that the 2D Raman features in domain I and II are different, and they have

been shown to correspond to ABC- and ABA-stacked trilayer graphene[118], respectively. It demonstrates unambiguously that the bright line features in trilayers are layer stacking domain walls, and supports our assignment for bilayers.

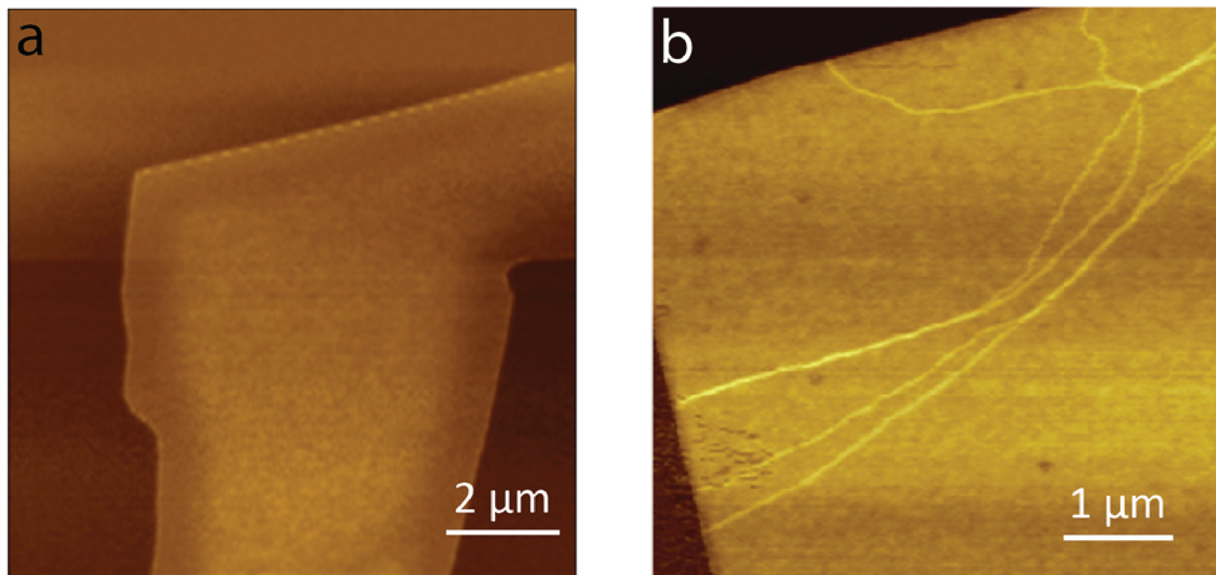

Figure 5.4: IR nanoscopy imaging of exfoliated monolayer and bilayer graphene. a. IR image of a graphene monolayer. The darker region corresponds to the SiO_2/Si substrate. Monolayer graphene shows homogeneous contrast across the whole sample with no bright lines in the interior area. (The bright lines parallel to the edge arise from plasmon excitations.) The same behavior is observed in all exfoliated monolayers. b. IR image of a graphene bilayer, which shows bright line features across the flake. Such bright lines arise from AB-BA domain walls in BLG and they are observed in ~ 30 % of exfoliated BLG samples. The bulk AB and BA domains have the same electronic structure and IR contrast.

5.5 Fabrication of Dual-gated Field-Effect-Transistor Devices on Bilayer Domain Walls

After identifying the layer stacking domain walls in BLG on SiO_2/Si substrate, we fabricated dual-gated bilayer FET devices[9][10] across the domain walls. As references, we also fabricated dual-gated devices without domain walls using the same device configuration on the same BLG flakes. Figure 5.6a displays the optical microscopy image of a representative device. The white dashed line outlines the BLG flake, and the green line denotes the position of the AB-BA domain wall in the BLG. Source and drain electrodes (electrodes 1 through

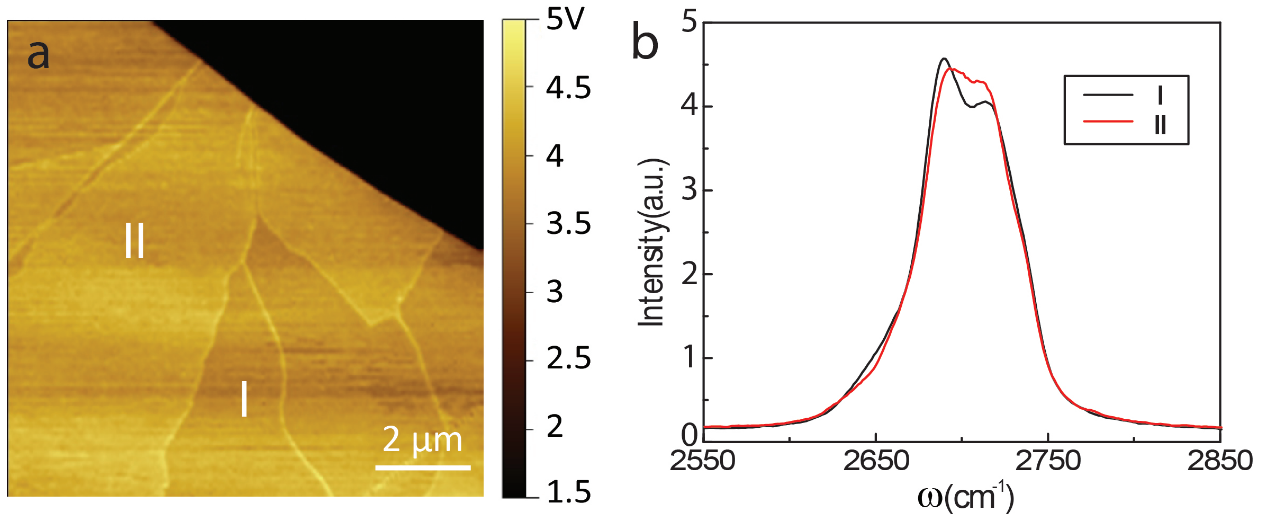

Figure 5.5: IR nanoscopy imaging of exfoliated trilayer graphene and its Raman spectrum. a. IR image of a graphene trilayer, which exhibits domains with different IR contrast as well as bright lines between domains. Different stacking orders, such as ABA and ABC stacking, can lead to different electronic structure and IR contrast in trilayers. b, Raman spectra taken at domain I and II in a. The 2D peak of domain I (black curve) and domain II (red curve) are characteristic of ABC and ABA stacking, respectively. It confirms that the bright and dark trilayer regions in c correspond to different layer stacking orders, and the bright line features arise from layer stacking domain walls.

5) composed of 40 nm Au and 0.5 nm Cr layers were defined by electron-beam lithography. Electrodes 1-2 are connected by a layer stacking domain wall, as are electrodes 2-3. Electrodes 3-4 and 4-5, on the other hand, are within a single BLG domain and act as reference devices. On top of the BLG flake, a 35 nm thick Al_2O_3 dielectric layer was grown using atomic layer deposition. Lastly the top gate electrodes of 1 μm width (TG1 and TG2) were patterned using electron-beam lithography and metal deposition. Figure 5.6b illustrates the side view of the device between electrodes 2 and 4, with a domain wall (green line) between electrode 2-3 and single-domain BLG between 3-4. Here the doped silicon substrate acts as a bottom gate. By varying the top gate voltage V_{tg} and the bottom gate voltage V_{bg}, we can control independently the electric field above and below the BLG to generate a tunable semiconductor bandgap[10].

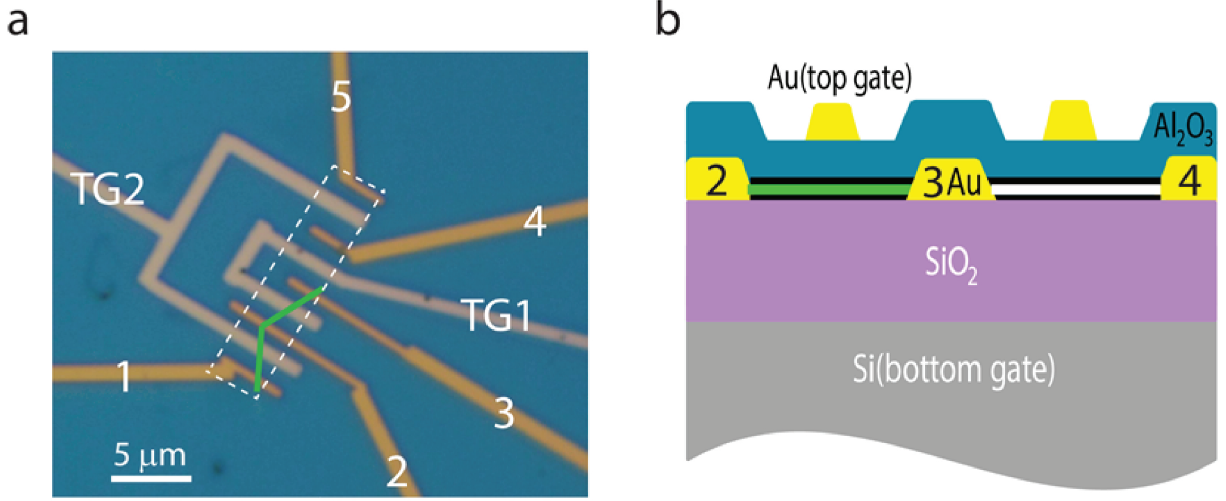

Figure 5.6: Dual-gated field effect transistor (FET) devices on bilayer graphene with AB-BA domain walls. a, Optical micrograph of a dual-gated bilayer device. The white dashed line outlines the BLG flake, and the green line denotes the AB-BA domain wall. Source and drain electrodes are labeled from 1 to 5. Electrodes 1-2 are connected by a layer stacking domain wall, as are electrodes 2-3. Electrodes 3-4 and 4-5, on the other hand, are within a single BLG domain and act as reference devices. TG1 and TG2 denote top gate electrodes. b, Side view of the dual-gated bilayer device between electrodes 2-4 in a.

5.6 Electric Transport Measurement of the One Dimensional Conducting Channels at Bilayer Domain Walls

Figure 5.7a displays the electrical transport at 4 K in a reference BLG device without a domain wall. Each trace shows the gate-dependent resistance as a function of V_{tg} at a fixed bottom gate voltage V_{bg}. V_{bg} was varied in steps of 10 V to produce the different traces. The resistance peak in each trace corresponds to a charge neutral point (CNP), at which the Fermi level resides within the semiconductor bandgap. CNPs can be realized with different combinations of V_{tg} and V_{bg}, but each with a different vertical electrical field and induced semiconductor bandgap in BLG. The zero bandgap state is realized at V_{bg0} = 0 V and V_{tg0} = 1.8 V, which has the lowest peak resistance. The average displacement field[10] across BLG is described by

$$D = 1/2(D_b + D_t) \tag{5.1}$$

where

$$D_b = \epsilon_{SiO_2} \left| V_{bg} - V_{bg0} \right| / d_{SiO_2} \tag{5.2}$$

and

$$D_t = \epsilon_{Al_2O_3} \left| V_{tg} - V_{tg0} \right| / d_{Al_2O_3} \tag{5.3}$$

ϵ and d are the dielectric constant and thickness of the respective oxide dielectric layers. The bandgap increases monotonically with the average vertical displacement field D, which results in a larger peak resistance at the CNP. The experimental values of the peak resistances are lower than that expected from the semiconductor bandgap in ideal BLG, presumably due to impurities and defects in our devices. Nevertheless, the resistance can reach $\sim 90\ k\Omega$, similar to that observed in previous dual-gated BLG devices on SiO_2/Si substrates[9].

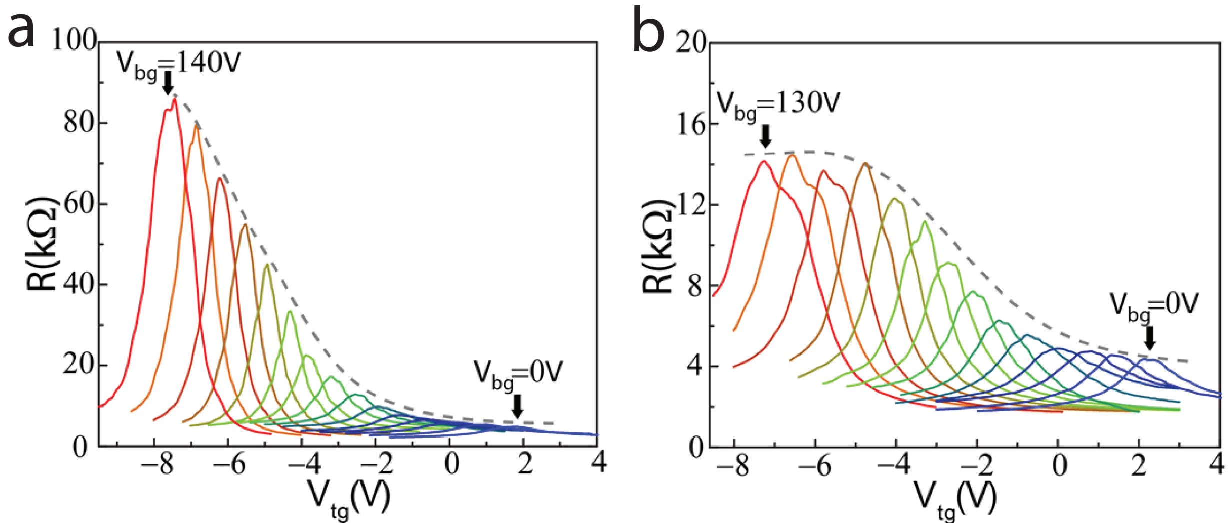

Figure 5.7: Electric transport behaviours of dual-gated FET devices on bilayer graphene with AB-BA domain walls. a, Gate-dependent resistance for BLG without a domain boundary (electrodes 3 and 4). The backgate voltage V_{bg} is varied from 0 to 140 V with a 10 V step, and the top gate voltage V_{tg} is swept continuously. The resistance peak in each trace corresponds to a charge neutral point (CNP). The resistance at the CNP increases continuously (dashed grey line) to over 80 kΩ at high V_{bg} due to the opening of a bandgap. b, Gate-dependent resistance across BLG with a domain boundary (electrodes 2 and 3). The resistance at the CNP first increases and then saturates at $\sim$ 14 kΩ although the BLG bandgap keeps increasing with increasing V_{bg}. This much lower resistance signifies the presence of a 1D conducting channel at the AB-BA domain wall.

Electrical transport through BLG with an AB-BA domain wall exhibits a distinctly different behavior, as shown in Fig. 5.7b. When the BLG bandgap is small (purple traces),

the gate-dependent resistance curves are similar to those in single-domain BLG devices because bulk current flowing through the domain dominates. With higher displacement fields and larger BLG bandgaps, the peak resistance in each curve first increases and then saturates at $\sim 14\ k\Omega$ (red traces in Fig. 5.7b), in striking contrast to the monotonically increasing resistance to over 80 $k\Omega$ in the reference device without a domain wall (Fig. 5.7a). Figure 5.8a plots the comparison of BLG peak resistances in the device with a domain wall (red circles) and without a domain wall (black squares) as a function of the vertical displacement field D, showing explicitly the saturation of the peak resistances at a much lower value due to the presence of the domain wall.

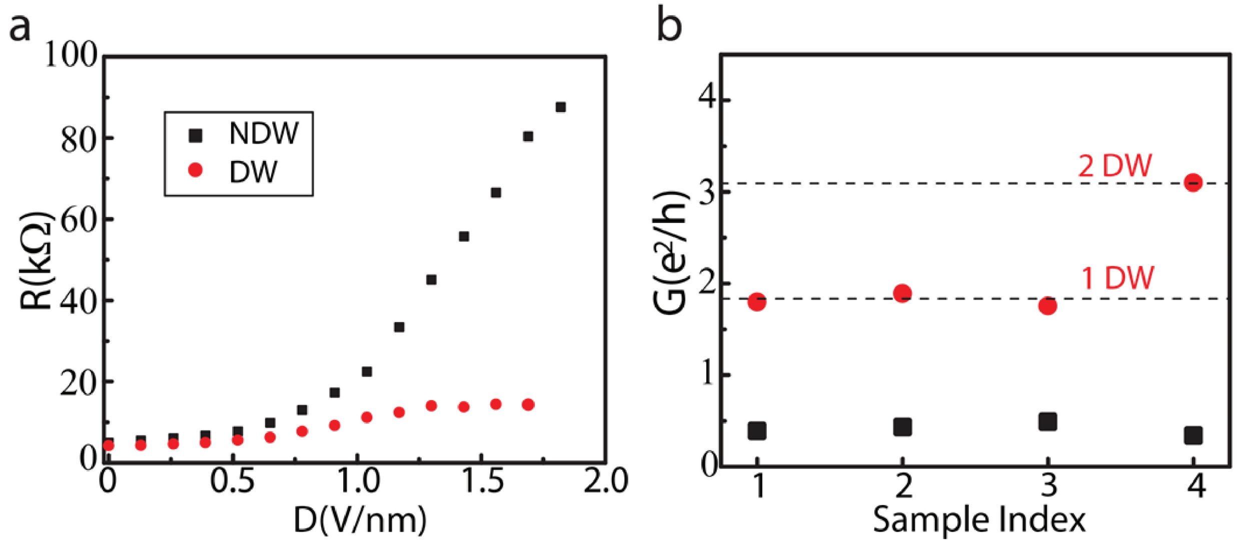

Figure 5.8: Conductance of topologically protected chiral modes at AB-BA domain walls. a, CNP resistances as a function of displacement field D for BLG with no domain wall (NDW, black squares) and for BLG with a domain wall (DW, red circles) obtained from Fig. 5.7. The saturation of the resistance at a much lower value at high D originates from 1D conducting channels at the domain wall. b, CNP conductance for four different BLG devices with domain walls (red circles) and corresponding reference devices without a domain wall (black squares) at D =1.56 V/nm. Devices 1 to 3 have a single domain wall connecting the source and drain electrodes, and device 4 has two parallel domain walls. Each domain wall contributes a conductance increase of $\sim 1.5\ e^2/h$. This conductance is similar to that of metallic carbon nanotubes, which can be described by four 1D ballistic channels.

The distinctly different transport behaviors in BLG with and without AB-BA domain walls were observed in all 5 pairs of BLG devices that were studied (see supplementary information for details). Figure 5.8b shows the conductance of 3 BLG devices with one domain wall each (red circles 1-3) and one BLG device with two domain walls (red circle 4)

and their corresponding reference devices fabricated on the same BLG flakes (black squares). The conductance values were taken in charge neutral BLG at $D = 1.56$ V/nm, where the bulk domain are rather insulating. It is apparent that the conductance is always much higher in BLG devices with AB-BA domain walls, increasing by ~ 1.5 e^2/h for one domain wall and by ~ 3 e^2/h for two domain walls. Our results demonstrate unambiguously 1D conducting channels are present at the AB-BA domain walls, and they dominate the electrical transport when bulk BLG domains become insulating.

The observed 1D conducting channels correspond to the chiral edge modes at AB-BA domain walls recently predicted by theory[98][96][99][100]. Figure 5.9a shows the electronic bandstructure around the K and K$'$ points for BLG with an AB-BA domain wall. In gapped BLG, the AB- and BA-stacked domains represent two different quantum valley Hall insulators. Consequently a domain wall separating insulating AB and BA domains will confine a pair of 1D conducting channels along the boundary for each valley. The conducting electrons in different valleys have opposite energy dispersions, and therefore propagate with opposite velocities. Such counter-propagating, valley-projected chiral electrons along the AB-BA domain walls are illustrated in Fig. 5.9b in real space. These conducting chiral modes are topologically protected within a single valley. Inter-valley scatterings can potentially mix the forward and backward moving electrons and eliminate the chiral modes, analogous to magnetic impurities that flip spins and eliminate chiral modes in quantum spin Hall insulators. However, at smooth varying AB-BA domain walls free of atomic defects, such inter-valley scattering will be absent because it requires a large momentum change of $4\pi/(3\sqrt{3}a_{c-c})$, where a_{c-c} is the carbon-carbon bond length of 1.42 $\mathring{A}$.

To better understand the conducting channels through the BLG domain walls, we investigated systematically BLG devices with varying channel length (defined by the top gate width) along the same BLG domain wall. Figure 5.10 displays measured conductance of the two sets of BLG domain wall channels with 200, 400, 600, and 800 nm lengths, respectively and the 1000 nm long BLG domain wall channels in Fig. 5.8b. All the conductance values are in the order of the quantum conductance 2 e^2/h, and one of the shortest channels exhibits a conductance approaching 4 e^2/h.

We can compare quantitatively the observed 1D conductance along the AB-BA domain wall with theoretical predictions. As illustrated in Fig. 5.9b, two conducting chiral modes are present at the domain wall for a given current flow direction. In addition, each chiral mode is doubly degenerate due to electron spin. Therefore, four 1D conducting channels exist at the domain wall, giving an ideal conductance of 4 e^2/h, i.e. two conductance quanta. Experimentally, we observed conductance in the order of the conductance quanta in all devices, and one 200 nm long domain wall channel exhibits conductance close to the value of 4 e^2/h (Fig. 5.10). We found that overall the 1D channel conductance becomes lower with increasing channel length. The observed length-dependent conductance through BLG

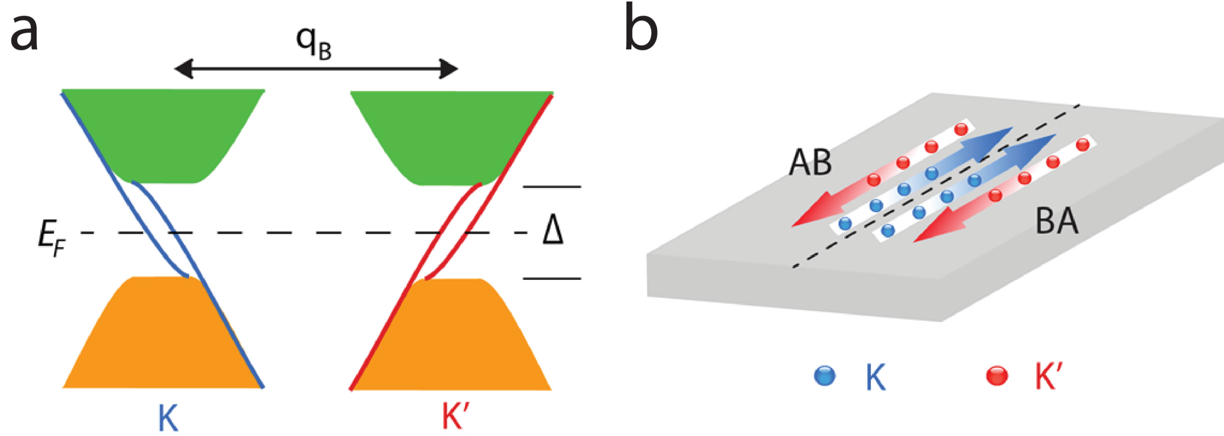

Figure 5.9: Electronic band structure of stacking domain walls and the valley polarized electrical current. a. Electronic band structure of BLG with an AB-BA domain wall. q_B indicates the momentum direction along the domain wall. Solid green and orange region represent states of the bulk bilayer with a bandgap of Δ and the blue (red) lines represent topologically protected K-valley (K′-valley) chiral electron modes at the domain wall. Each chiral electron mode is doubly spin degenerate, leading to four valley-polarized 1D conducting channels at the AB-BA domain wall of a gapped BLG. b. Illustration of valley-polarized electrical current at the BLG AB-BA domain wall. Boundary states in the K and K valley move in opposite one-way channels, leading to ballistic charge and valley current along the domain wall.

domain walls can be described by the Landauer-Buttiker formula[119] with a finite electron mean free path: $G = (R_c + R_0(1 + L/L_0))^{-1}$, where L is the channel length, $R_0 = h/(4e^2)$, the contact resistance R_c= 0 , and the mean free path L_0 = 420 nm (solid line in Fig. 5.10). The electron mean free path of 420 nm can arise from a finite inter-valley scattering along the BLG domain walls, and previous transport studies have reported a comparable inter-valley scattering length of 300-800 nm in BLG on SiO_2/Si substrates[120]. Nevertheless, this electron mean free path along BLG domain wall is orders of magnitude longer than that in the BLG domain, which has a mobility $\sim$ 2000 cm^2/V.s and a mean free path of only $\sim$ 8 nm in our samples. Generally, scattering and localization effects tend to be more important in 1D. The much longer mean free path at the AB-BA domain walls therefore highlights the topological protection of chiral electron modes, where the electron velocity-valley locking forbids intra-valley backscattering. Because inter-valley scattering along the smooth domain walls is negligible, the chiral valley channels at AB-BA domain walls are very robust even for BLG devices on SiO_2/Si substrates. One can envision that encapsulation in boron nitride layers[121] can potentially lead to chiral electrons at AB-BA domain wall with very long coherent lengths.

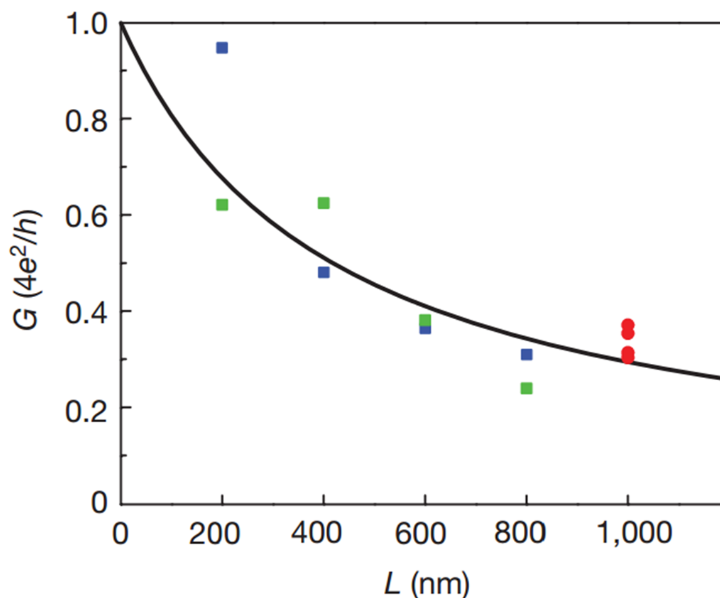

Figure 5.10: Length dependence of the bilayer graphene domain wall conductance. Green and blue symbols represent two sets of devices, each fabricated on one single domain wall in the same BLG flake. Red symbols represent the 1000 nm long BLG single domain wall channels in Fig. 5.8b. All devices exhibit conductance in the order of the quantum conductance, with lower conductance in longer channels and a maximum conductance approaching 4 e^2/h. This length dependent 1D conductance can be described by 4 conducting channels with a mean free path of 420nm using the Landauer-Buttiker formula (solid line).

5.7 Temperature Dependence of Electrical Transport of AB-BA Domain Walls

We investigated the temperature dependence of electrical transport both through AB-stacked bilayer graphene and through AB-BA domain walls. Figure 5.11 displays representative data for CNP resistance at $V_{bg} = -140\ V$ for a bilayer graphene device without a domain wall (black line) and a device with a domain wall (red line). For the bilayer graphene bulk device without a domain wall, the CNP resistance increases by over 300 $k\Omega$ (~2.5 times) as the temperature is varied from 50 K to 1.8 K. This large increase of resistance at lower temperatures is characteristic of insulating behaviour. In comparison, the CNP resistance of device with a domain wall (red line) has much weaker temperature dependence: the resistance increase is only 5 $k\Omega$ ($\sim 50\%$), and part of the increase is due to the contribution from bulk bilayer graphene channel in parallel with the one-dimensional domain wall channel. The weak temperature dependence of conductance along the domain wall is characteristic of a metallic system.

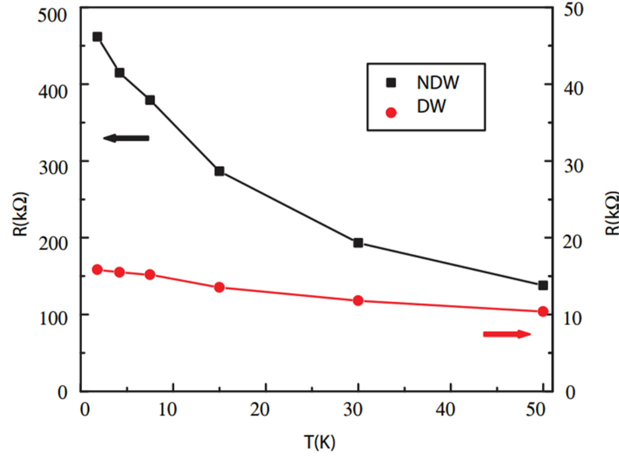

Figure 5.11: Temperature-dependent electrical transport through bulk bilayer graphene and through the AB-BA domain wall. The CNP resistance ($V_{bg} = -140\ V$) of a bilayer graphene device without a domain wall (NDW, black line) increases by over 300 $k\Omega$ ($\sim$ 2.5 times) as the temperature is decreased from 50 K to 1.8 K. In contrast, the CNP resistance ($V_{bg} = -140\ V$) of a bilayer graphene device with domain wall increases by only 5 $k\Omega$ ($\sim$ 50%) at the same temperature. The much weaker temperature dependence of the domain wall resistance arises from a metallic one-dimensional conducting channel.

5.8 Topological Understanding of The 1D Boundary States at Bilayer Domain Walls

In recent years, topological insulator[122][123] is introduced to condensed matter physics as a new concept which allows physicists to classify insulators by the topological properties of their electronic bands in momentum spaces. Topological insulators feature a group of materials that have insulating bulk states but can host gapless edge/surface states. These surface states are protected by the time reversal symmetry. The concept of topological phases has been generalized later to include protection by different symmetries[107]. In this respect, gapped bilayer graphene is a symmetry protected Z-type topological insulating phase, as examined in detail in Ref. [99]. Although the total Chern number is zero for the whole Brillouin zone, an integer Chern number with opposite sign is present for each valley in gapped bilayer graphene, as shown by ref. [96][95]. This valley-dependent Chern number gives rise to valley-polarized edge states, and they are topologically protected by the symmetry that forbids the inter-valley scattering. Based on the generalized notation of topological phases, Ref. [99] showed explicitly that the quantum valley Hall state can be categorized as a Z-type symmetry protected topological insulating phase by no-valley mixing symmetry.

In the case of Z2 topological insulators protected by time-reversal symmetry, magnetic impurities can localize the edges states because they break the time reversal symmetry[124]. But as long as the time-reversal symmetry is respected, the protection is topological. Similarly, intervalley scattering localizes the valley-polarized chiral states because it breaks the no-valley mixing symmetry. But these chiral states are topologically protected as long as the no-valley mixing symmetry is present. At bilayer AB-BA domain boundaries no-valley mixing is a good approximation, and therefore the valley-polarized chiral states along the boundary is well protected.

The topological protection of such chiral edge states are more robust than the edge states of single domain bilayer graphene. The edge states in single domain bilayer graphene are sensitive to the bilayer graphene edge termination, and they are gapped out with armchair termination[125]. However, the 1D conducting channel of domain walls studied in our manuscript does not depend so sensitively on specific boundaries. In particular, a theoretical study by Jung et al [125] showed that the 1D chiral states can exist in domain boundaries of any crystallographic orientations, including the armchair directions, as long as the domain wall is extended over nanometer size as in our case.

5.9 Summary

Our observation of topologically protected 1D conducting channels at BLG domain walls opens up exciting opportunities to explore tunable topological phases and valley physics in graphene. Due to the velocity-valley locking, the 1D chiral modes at the AB-BA domain walls lead to not only ballistic charge transport, but also ballistic valley transport. It can enable novel ways to control the valley degree of freedom for graphene-based valleytronic devices.

Bibliography

[1] K. Novoselov, A. K. Geim, S. Morozov, D. Jiang, M. K. I. Grigorieva, S. Dubonos, and A. Firsov, "Two-dimensional gas of massless dirac fermions in graphene", nature **438**, 197 (2005).

[2] Y. Zhang, Y.-W. Tan, H. L. Stormer, and P. Kim, "Experimental observation of the quantum hall effect and berry's phase in graphene", Nature **438**, 201 (2005).

[3] P. R. Wallace, "The band theory of graphite", Physical Review **71**, 622 (1947).

[4] A. C. Neto, F Guinea, N. Peres, K. S. Novoselov, and A. K. Geim, "The electronic properties of graphene", Reviews of modern physics **81**, 109 (2009).

[5] Y. Zhang, "Electronic transport in graphene", PhD thesis (Columbia University, 2006).

[6] E. V. Castro, K. Novoselov, S. Morozov, N. Peres, J. L. Dos Santos, J. Nilsson, F Guinea, A. Geim, and A. C. Neto, "Biased bilayer graphene: semiconductor with a gap tunable by the electric field effect", Physical Review Letters **99**, 216802 (2007).

[7] E. McCann, "Asymmetry gap in the electronic band structure of bilayer graphene", Physical Review B **74**, 161403 (2006).

[8] H. Min, B. Sahu, S. K. Banerjee, and A. MacDonald, "Ab initio theory of gate induced gaps in graphene bilayers", Physical Review B **75**, 155115 (2007).

[9] J. B. Oostinga, H. B. Heersche, X. Liu, A. F. Morpurgo, and L. M. Vandersypen, "Gate-induced insulating state in bilayer graphene devices", Nature materials **7**, 151 (2008).

[10] Y. Zhang, T.-T. Tang, C. Girit, Z. Hao, M. C. Martin, A. Zettl, M. F. Crommie, Y. R. Shen, and F. Wang, "Direct observation of a widely tunable bandgap in bilayer graphene", Nature **459**, 820 (2009).

[11] T. Ando, Y. Zheng, and H. Suzuura, "Dynamical conductivity and zero-mode anomaly in honeycomb lattices", Journal of the Physical Society of Japan **71**, 1318 (2002).

[12] V. Gusynin, S. Sharapov, and J. Carbotte, "Unusual microwave response of dirac quasiparticles in graphene", Physical review letters **96**, 256802 (2006).

[13] N. Peres, F Guinea, and A. C. Neto, "Electronic properties of disordered two-dimensional carbon", Physical Review B **73**, 125411 (2006).

[14] N. Peres, "Colloquium: the transport properties of graphene: an introduction", Reviews of Modern Physics **82**, 2673 (2010).

[15] S. D. Sarma, S. Adam, E. Hwang, and E. Rossi, "Electronic transport in two-dimensional graphene", Reviews of Modern Physics **83**, 407 (2011).

[16] J. Horng, C.-F. Chen, B. Geng, C. Girit, Y. Zhang, Z. Hao, H. A. Bechtel, M. Martin, A. Zettl, M. F. Crommie, et al., "Drude conductivity of dirac fermions in graphene", Physical Review B **83**, 165113 (2011).

[17] T.-J. Yen, W. Padilla, N. Fang, D. Vier, D. Smith, J. Pendry, D. Basov, and X. Zhang, "Terahertz magnetic response from artificial materials", Science **303**, 1494 (2004).

[18] J. Pendry, A. Holden, W. Stewart, and I Youngs, "Extremely low frequency plasmons in metallic mesostructures", Physical review letters **76**, 4773 (1996).

[19] H.-T. Chen, W. J. Padilla, J. M. Zide, A. C. Gossard, A. J. Taylor, and R. D. Averitt, "Active terahertz metamaterial devices", Nature **444**, 597 (2006).

[20] B Wunsch, T Stauber, F Sols, and F Guinea, "Dynamical polarization of graphene at finite doping", New Journal of Physics **8**, 318 (2006).

[21] M. Polini, A. H. MacDonald, and G. Vignale, "Drude weight, plasmon dispersion, and pseudospin response in doped graphene sheets", arXiv preprint arXiv:0901.4528 (2009).

[22] E. Hwang and S. D. Sarma, "Dielectric function, screening, and plasmons in two-dimensional graphene", Physical Review B **75**, 205418 (2007).

[23] L. Brey and H. Fertig, "Elementary electronic excitations in graphene nanoribbons", Physical Review B **75**, 125434 (2007).

[24] A. Vakil and N. Engheta, "One-atom-thick ir metamaterials and transformation optics using graphene", arXiv preprint arXiv:1101.3585 (2011).

[25] M. Jablan, H. Buljan, and M. Soljačić, "Plasmonics in graphene at infrared frequencies", Physical review B **80**, 245435 (2009).

[26] F. H. Koppens, D. E. Chang, and F. J. Garcia de Abajo, "Graphene plasmonics: a platform for strong light–matter interactions", Nano letters **11**, 3370 (2011).

[27] F. Rana, "Graphene terahertz plasmon oscillators", Nanotechnology, IEEE Transactions on **7**, 91 (2008).

[28] M. Ryzhii and V. Ryzhii, "Injection and population inversion in electrically induced p–n junction in graphene with split gates", Japanese journal of applied physics **46**, L151 (2007).

[29] S. Allen Jr, D. Tsui, and R. Logan, "Observation of the two-dimensional plasmon in silicon inversion layers", Physical Review Letters **38**, 980 (1977).

[30] E Batke, D Heitmann, and C. Tu, "Plasmon and magnetoplasmon excitation in two-dimensional electron space-charge layers on gaas", Physical Review B **34**, 6951 (1986).

[31] L. Ju, B. Geng, J. Horng, C. Girit, M. Martin, Z. Hao, H. A. Bechtel, X. Liang, A. Zettl, Y. R. Shen, et al., "Graphene plasmonics for tunable terahertz metamaterials", Nature nanotechnology **6**, 630 (2011).

[32] J. H. Cho, J. Lee, Y. Xia, B. Kim, Y. He, M. J. Renn, T. P. Lodge, and C. D. Frisbie, "Printable ion-gel gate dielectrics for low-voltage polymer thin-film transistors on plastic", Nature materials **7**, 900 (2008).

[33] Z. Li, E. A. Henriksen, Z Jiang, Z. Hao, M. C. Martin, P Kim, H. Stormer, and D. N. Basov, "Dirac charge dynamics in graphene by infrared spectroscopy", Nature Physics **4**, 532 (2008).

[34] F. Wang, Y. Zhang, C. Tian, C. Girit, A. Zettl, M. Crommie, and Y. R. Shen, "Gate-variable optical transitions in graphene", Science **320**, 206 (2008).

[35] K. Yamamoto, M. Tani, and M. Hangyo, "Terahertz time-domain spectroscopy of imidazolium ionic liquids", The Journal of Physical Chemistry B **111**, 4854 (2007).

[36] E. D. Palik, *Handbook of optical constants of solids*, Vol. 3 (Academic press, 1998).

[37] D. K. Efetov and P. Kim, "Controlling electron-phonon interactions in graphene at ultrahigh carrier densities", Physical review letters **105**, 256805 (2010).

[38] A. Geim and I. Grigorieva, "Van der waals heterostructures", Nature **499**, 419 (2013).

[39] G. Li, A Luican, J. L. Dos Santos, A. C. Neto, A Reina, J Kong, and E. Andrei, "Observation of van hove singularities in twisted graphene layers", Nature Physics **6**, 109 (2009).

[40] J. Xue, J. Sanchez-Yamagishi, D. Bulmash, P. Jacquod, A. Deshpande, K Watanabe, T Taniguchi, P. Jarillo-Herrero, and B. J. LeRoy, "Scanning tunnelling microscopy and spectroscopy of ultra-flat graphene on hexagonal boron nitride", Nature materials **10**, 282 (2011).

[41] R. Decker, Y. Wang, V. W. Brar, W. Regan, H.-Z. Tsai, Q. Wu, W. Gannett, A. Zettl, and M. F. Crommie, "Local electronic properties of graphene on a bn substrate via scanning tunneling microscopy", Nano letters **11**, 2291 (2011).

[42] M. Yankowitz, J. Xue, D. Cormode, J. D. Sanchez-Yamagishi, K Watanabe, T Taniguchi, P. Jarillo-Herrero, P. Jacquod, and B. J. LeRoy, "Emergence of superlattice dirac points in graphene on hexagonal boron nitride", Nature Physics **8**, 382 (2012).

[43] L. Ponomarenko, R. Gorbachev, G. Yu, D. Elias, R Jalil, A. Patel, A Mishchenko, A. Mayorov, C. Woods, J. Wallbank, et al., "Cloning of dirac fermions in graphene superlattices", Nature **497**, 594 (2013).

[44] C. Dean, L Wang, P Maher, C Forsythe, F Ghahari, Y Gao, J Katoch, M Ishigami, P Moon, M Koshino, et al., "Hofstadter's butterfly and the fractal quantum hall effect in moire superlattices", Nature **497**, 598 (2013).

[45] B Hunt, J. Sanchez-Yamagishi, A. Young, M Yankowitz, B. J. LeRoy, K Watanabe, T Taniguchi, P Moon, M Koshino, P Jarillo-Herrero, et al., "Massive dirac fermions and hofstadter butterfly in a van der waals heterostructure", Science **340**, 1427 (2013).

[46] L Ju, J Velasco Jr, E Huang, S Kahn, C Nosiglia, H.-Z. Tsai, W Yang, T Taniguchi, K Watanabe, Y Zhang, et al., "Photoinduced doping in heterostructures of graphene and boron nitride", Nature nanotechnology **9**, 348 (2014).

[47] L Museur, G Brasse, A Pierret, S Maine, B Attal-Tretout, F Ducastelle, A Loiseau, J Barjon, K Watanabe, T Taniguchi, et al., "Exciton optical transitions in a hexagonal boron nitride single crystal", physica status solidi (RRL)-Rapid Research Letters **5**, 214 (2011).

[48] C. Dean, A. Young, I Meric, C Lee, L Wang, S Sorgenfrei, K Watanabe, T Taniguchi, P Kim, K. Shepard, et al., "Boron nitride substrates for high-quality graphene electronics", Nature nanotechnology **5**, 722 (2010).

[49] L. Britnell, R. Ribeiro, A Eckmann, R Jalil, B. Belle, A Mishchenko, Y.-J. Kim, R. Gorbachev, T Georgiou, S. Morozov, et al., "Strong light-matter interactions in heterostructures of atomically thin films", Science **340**, 1311 (2013).

[50] P. Zomer, S. Dash, N Tombros, and B. Van Wees, "A transfer technique for high mobility graphene devices on commercially available hexagonal boron nitride", Applied Physics Letters **99**, 232104 (2011).

[51] W. Yang, G. Chen, Z. Shi, C.-C. Liu, L. Zhang, G. Xie, M. Cheng, D. Wang, R. Yang, D. Shi, et al., "Epitaxial growth of single-domain graphene on hexagonal boron nitride", Nature materials **12**, 792 (2013).

[52] Y. D. Kim, M.-H. Bae, J.-T. Seo, Y. S. Kim, H. Kim, J. H. Lee, J. R. Ahn, S. W. Lee, S.-H. Chun, and Y. D. Park, "Focused-laser-enabled p–n junctions in graphene field-effect transistors", ACS nano **7**, 5850 (2013).

[53] A. Tiberj, M. Rubio-Roy, M. Paillet, J.-R. Huntzinger, P. Landois, M. Mikolasek, S. Contreras, J.-L. Sauvajol, E. Dujardin, and A.-A. Zahab, "Reversible optical doping of graphene", Scientific reports **3** (2013).

[54] E. Hwang, S Adam, and S. D. Sarma, "Carrier transport in two-dimensional graphene layers", Physical Review Letters **98**, 186806 (2007).

[55] J. Yan and M. S. Fuhrer, "Correlated charged impurity scattering in graphene", Physical review letters **107**, 206601 (2011).

[56] C. Attaccalite, M. Bockstedte, A. Marini, A Rubio, and L. Wirtz, "Coupling of excitons and defect states in boron-nitride nanostructures", Physical Review B **83**, 144115 (2011).

[57] F Schedin, A. Geim, S. Morozov, E. Hill, P Blake, M. Katsnelson, and K. Novoselov, "Detection of individual gas molecules adsorbed on graphene", Nature materials **6**, 652 (2007).

[58] J.-H. Chen, C Jang, S Adam, M. Fuhrer, E. Williams, and M Ishigami, "Charged-impurity scattering in graphene", Nature Physics **4**, 377 (2008).

[59] K Pi, K. McCreary, W Bao, W. Han, Y. Chiang, Y. Li, S.-W. Tsai, C. Lau, and R. Kawakami, "Electronic doping and scattering by transition metals on graphene", Physical Review B **80**, 075406 (2009).

[60] R Dingle, H. Störmer, A. Gossard, and W Wiegmann, "Electron mobilities in modulation-doped semiconductor heterojunction superlattices", Applied Physics Letters **33**, 665 (1978).

[61] L. Pfeiffer, K. West, H. Stormer, and K. Baldwin, "Electron mobilities exceeding 107 cm2/v s in modulation-doped gaas", Applied Physics Letters **55**, 1888 (1989).

[62] B Huard, J. Sulpizio, N Stander, K Todd, B Yang, and D Goldhaber-Gordon, "Transport measurements across a tunable potential barrier in graphene", Physical Review Letters **98**, 236803 (2007).

[63] J. Williams, L DiCarlo, and C. Marcus, "Quantum hall effect in a gate-controlled pn junction of graphene", Science **317**, 638 (2007).

[64] B. Özyilmaz, P. Jarillo-Herrero, D. Efetov, D. A. Abanin, L. S. Levitov, and P. Kim, "Electronic transport and quantum hall effect in bipolar graphene p-n-p junctions", Physical review letters **99**, 166804 (2007).

[65] T. Lohmann, K. von Klitzing, and J. H. Smet, "Four-terminal magneto-transport in graphene pn junctions created by spatially selective doping", Nano letters **9**, 1973 (2009).

[66] G. Binnig, H. Rohrer, C. Gerber, and E. Weibel, "Surface studies by scanning tunneling microscopy", Phys. Rev. Lett. **49**, 57 (1982).

[67] V. W. Brar, "Scanning tunneling spectroscopy of graphene and magnetic nanostructures", (2010).

[68] G. Binnig and H. Rohrer, "Scanning tunneling microscopy from birth to adolescence", Reviews of Modern Physics **59**, 615 (1987).

[69] V Madhavan, W Chen, T Jamneala, M. Crommie, and N. Wingreen, "Tunneling into a single magnetic atom: spectroscopic evidence of the kondo resonance", Science **280**, 567 (1998).

[70] R. Feenstra, J. Woodall, and G. Pettit, "Observation of bulk defects by scanning tunneling microscopy and spectroscopy: arsenic antisite defects in gaas", Physical review letters **71**, 1176 (1993).

[71] J. Zheng, X Liu, N Newman, E. Weber, D. Ogletree, and M Salmeron, "Scanning tunneling microscopy studies of si donors (si ga) in gaas", Physical review letters **72**, 1490 (1994).

[72] K Teichmann, M. Wenderoth, S Loth, R. Ulbrich, J. Garleff, A. Wijnheijmer, and P. Koenraad, “Controlled charge switching on a single donor with a scanning tunneling microscope”, Physical review letters **101**, 076103 (2008).

[73] A. Wijnheijmer, J. Garleff, K Teichmann, M. Wenderoth, S Loth, R. Ulbrich, P. Maksym, M. Roy, and P. Koenraad, “Enhanced donor binding energy close to a semiconductor surface”, Physical review letters **102**, 166101 (2009).

[74] D. Lee and J. Gupta, “Tunable field control over the binding energy of single dopants by a charged vacancy in gaas”, Science **330**, 1807 (2010).

[75] D. Kitchen, A. Richardella, J.-M. Tang, M. E. Flatté, and A. Yazdani, “Atom-by-atom substitution of mn in gaas and visualization of their hole-mediated interactions”, Nature **442**, 436 (2006).

[76] J. Repp, G. Meyer, F. E. Olsson, and M. Persson, “Controlling the charge state of individual gold adatoms”, Science **305**, 493 (2004).

[77] Y. Wang, V. W. Brar, A. V. Shytov, Q. Wu, W. Regan, H.-Z. Tsai, A. Zettl, L. S. Levitov, and M. F. Crommie, “Mapping dirac quasiparticles near a single coulomb impurity on graphene”, Nature Physics **8**, 653 (2012).

[78] V. W. Brar, R. Decker, H.-M. Solowan, Y. Wang, L. Maserati, K. T. Chan, H. Lee, Ç. O. Girit, A. Zettl, S. G. Louie, et al., “Gate-controlled ionization and screening of cobalt adatoms on a graphene surface”, Nature Physics **7**, 43 (2011).

[79] J. E. Johns and M. C. Hersam, “Atomic covalent functionalization of graphene”, Accounts of chemical research **46**, 77 (2012).

[80] M. Scheffler, D. Haberer, L. Petaccia, M. Farjam, R. Schlegel, D. Baumann, T. Hanke, A. Gruneis, M. Knupfer, C. Hess, et al., “Probing local hydrogen impurities in quasi-free-standing graphene”, ACS nano **6**, 10590 (2012).

[81] J. S. Bunch, S. S. Verbridge, J. S. Alden, A. M. van der Zande, J. M. Parpia, H. G. Craighead, and P. L. McEuen, “Impermeable atomic membranes from graphene sheets”, Nano letters **8**, 2458 (2008).

[82] M Fanciulli and T. Moustakas, “Study of defects in wide band gap semiconductors by electron paramagnetic resonance”, Physica B: Condensed Matter **185**, 228 (1993).

[83] A Katzir, J. Suss, A Zunger, and A Halperin, “Point defects in hexagonal boron nitride. i. epr, thermoluminescence, and thermally-stimulated-current measurements”, Physical Review B **11**, 2370 (1975).

[84] E. Andrei, A Katzir, and J. Suss, “Point defects in hexagonal boron nitride. iii. epr in electron-irradiated bn”, Physical Review B **13**, 2831 (1976).

[85] A Zunger and A Katzir, “Point defects in hexagonal boron nitride. ii. theoretical studies”, Physical review B **11**, 2378 (1975).

[86] Z. Remes, M. Nesladek, K. Haenen, K Watanabe, and T Taniguchi, "The optical absorption and photoconductivity spectra of hexagonal boron nitride single crystals", physica status solidi (a) **202**, 2229 (2005).

[87] T Taniguchi and K Watanabe, "Synthesis of high-purity boron nitride single crystals under high pressure by using ba–bn solvent", Journal of crystal growth **303**, 525 (2007).

[88] Y. Zhang, V. W. Brar, F. Wang, C. Girit, Y. Yayon, M. Panlasigui, A. Zettl, and M. F. Crommie, "Giant phonon-induced conductance in scanning tunnelling spectroscopy of gate-tunable graphene", Nature Physics **4**, 627 (2008).

[89] Y. Wang, D. Wong, A. V. Shytov, V. W. Brar, S. Choi, Q. Wu, H.-Z. Tsai, W. Regan, A. Zettl, R. K. Kawakami, et al., "Observing atomic collapse resonances in artificial nuclei on graphene", Science **340**, 734 (2013).

[90] M. T. Woodside and P. L. McEuen, "Scanned probe imaging of single-electron charge states in nanotube quantum dots", Science **296**, 1098 (2002).

[91] J. Zhu, M. Brink, and P. L. McEuen, "Single-electron force readout of nanoparticle electrometers attached to carbon nanotubes", Nano letters **8**, 2399 (2008).

[92] N. Pradhan, N Liu, C Silien, and W Ho, "Atomic scale conductance induced by single impurity charging", Physical review letters **94**, 076801 (2005).

[93] N. Kharche and S. K. Nayak, "Quasiparticle band gap engineering of graphene and graphone on hexagonal boron nitride substrate", Nano letters **11**, 5274 (2011).

[94] J. Garleff, A. Wijnheijmer, C. vd Enden, and P. Koenraad, "Bistable behavior of silicon atoms in the (110) surface of gallium arsenide", Physical Review B **84**, 075459 (2011).

[95] F. Zhang, J. Jung, G. A. Fiete, Q. Niu, and A. H. MacDonald, "Spontaneous quantum hall states in chirally stacked few-layer graphene systems", Phys. Rev. Lett. **106**, 156801 (2011).

[96] F. Zhang, A. H. MacDonald, and E. J. Mele, "Valley chern numbers and boundary modes in gapped bilayer graphene", Proceedings of the National Academy of Sciences **110**, 10546 (2013).

[97] J. Yan and M. S. Fuhrer, "Charge transport in dual gated bilayer graphene with corbino geometry", Nano Letters **10**, PMID: 20919729, 4521 (2010).

[98] I. Martin, Y. M. Blanter, and A. F. Morpurgo, "Topological confinement in bilayer graphene", Phys. Rev. Lett. **100**, 036804 (2008).

[99] A. Vaezi, Y. Liang, D. H. Ngai, L. Yang, and E.-A. Kim, "Topological edge states at a tilt boundary in gated multilayer graphene", Phys. Rev. X **3**, 021018 (2013).

[100] A. R. Wright and T. Hyart, "Robust one-dimensional wires in lattice mismatched bilayer graphene", Applied Physics Letters **98**, 251902, – (2011).

[101] F. Keilmann and R. Hillenbrand, "Near-field microscopy by elastic light scattering from a tip", PHILOSOPHICAL TRANSACTIONS-ROYAL SOCIETY OF LONDON SERIES A MATHEMATICAL PHYSICAL AND ENGINEERING SCIENCES, 787 (2004).

[102] J. Chen, M. Badioli, P. Alonso-Gonzalez, S. Thongrattanasiri, F. Huth, J. Osmond, M. Spasenovic, A. Centeno, A. Pesquera, P. Godignon, A. Zurutuza Elorza, N. Camara, F. Javier Garcia de Abajo, R. Hillenbrand, and F. H. L. Koppens, "Optical nano-imaging of gate-tunable graphene plasmons", NATURE **487**, 77 (2012).

[103] Z. Fei, A. S. Rodin, G. O. Andreev, W. Bao, A. S. McLeod, M. Wagner, L. M. Zhang, Z. Zhao, M. Thiemens, G. Dominguez, M. M. Fogler, A. H. Castro Neto, C. N. Lau, F. Keilmann, and D. N. Basov, "Gate-tuning of graphene plasmons revealed by infrared nano-imaging", NATURE **487**, 82 (2012).

[104] K. Novoselov, E McCann, S. Morozov, V. Fal'ko, M. Katsnelson, U Zeitler, D Jiang, F Schedin, and A. Geim, "Unconventional quantum Hall effect and Berry's phase of 2 pi in bilayer graphene", NATURE PHYSICS **2**, 177 (2006).

[105] C. L. Kane and E. J. Mele, "Quantum spin hall effect in graphene", Phys. Rev. Lett. **95**, 226801 (2005).

[106] M. Koenig, S. Wiedmann, C. Bruene, A. Roth, H. Buhmann, L. W. Molenkamp, X.-L. Qi, and S.-C. Zhang, "Quantum spin hall insulator state in HgTe quantum wells", SCIENCE **318**, 766 (2007).

[107] X.-G. Wen, "Symmetry-protected topological phases in noninteracting fermion systems", Phys. Rev. B **85**, 085103 (2012).

[108] W. Yao, S. A. Yang, and Q. Niu, "Edge states in graphene: from gapped flat-band to gapless chiral modes", Phys. Rev. Lett. **102**, 096801 (2009).

[109] R. T. Weitz, M. T. Allen, B. E. Feldman, J. Martin, and A. Yacoby, "Broken-Symmetry States in Doubly Gated Suspended Bilayer Graphene", SCIENCE **330**, 812 (2010).

[110] J. Velasco, Jr., L. Jing, W. Bao, Y. Lee, P. Kratz, V. Aji, M. Bockrath, C. N. Lau, C. Varma, R. Stillwell, D. Smirnov, F. Zhang, J. Jung, and A. H. MacDonald, "Transport spectroscopy of symmetry-broken insulating states in bilayer graphene", NATURE NANOTECHNOLOGY **7**, 156 (2012).

[111] P. Maher, C. R. Dean, A. F. Young, T. Taniguchi, K. Watanabe, K. L. Shepard, J. Hone, and P. Kim, "Evidence for a spin phase transition at charge neutrality in bilayer graphene", NATURE PHYSICS **9**, 154 (2013).

[112] J. S. Alden, A. W. Tsen, P. Y. Huang, R. Hovden, L. Brown, J. Park, D. A. Muller, and P. L. McEuen, "Strain solitons and topological defects in bilayer graphene", Proceedings of the National Academy of Sciences **110**, 11256 (2013).

[113] B. Butz, C. Dolle, F. Niekiel, K. Weber, D. Waldmann, H. B. Weber, B. Meyer, and E. Spiecker, "Dislocations in bilayer graphene", NATURE **505**, 533+ (2014).

[114] K. S. Novoselov, A. K. Geim, S. Morozov, D Jiang, Y. Zhang, S. Dubonos, I. Grigorieva, and A. Firsov, "Electric field effect in atomically thin carbon films", science **306**, 666 (2004).

[115] J. L. Dos Santos, N. Peres, and A. C. Neto, "Graphene bilayer with a twist: electronic structure", Physical review letters **99**, 256802 (2007).

[116] K. F. Mak, M. Y. Sfeir, J. A. Misewich, and T. F. Heinz, "The evolution of electronic structure in few-layer graphene revealed by optical spectroscopy", Proceedings of the National Academy of Sciences **107**, 14999 (2010).

[117] C. H. Lui, Z. Li, K. F. Mak, E. Cappelluti, and T. F. Heinz, "Observation of an electrically tunable band gap in trilayer graphene", NATURE PHYSICS **7**, 944 (2011).

[118] C. H. Lui, Z. Li, Z. Chen, P. V. Klimov, L. E. Brus, and T. F. Heinz, "Imaging stacking order in few-layer graphene", Nano Letters **11**, PMID: 21121668, 164 (2011).

[119] S. Datta, *Electronic transport in mesoscopic systems* (Cambridge university press, 1997).

[120] R. Gorbachev, F. Tikhonenko, A. Mayorov, D. Horsell, and A. Savchenko, "Weak localization in bilayer graphene", Physical review letters **98**, 176805 (2007).

[121] L. Wang, I. Meric, P. Y. Huang, Q. Gao, Y. Gao, H. Tran, T. Taniguchi, K. Watanabe, L. M. Campos, D. A. Muller, J. Guo, P. Kim, J. Hone, K. L. Shepard, and C. R. Dean, "One-dimensional electrical contact to a two-dimensional material", Science **342**, 614 (2013).

[122] M. Z. Hasan and C. L. Kane, "Colloquium: topological insulators", Reviews of Modern Physics **82**, 3045 (2010).

[123] X.-L. Qi and S.-C. Zhang, "Topological insulators and superconductors", Reviews of Modern Physics **83**, 1057 (2011).

[124] Y. Chen, J.-H. Chu, J. Analytis, Z. Liu, K. Igarashi, H.-H. Kuo, X. Qi, S.-K. Mo, R. Moore, D. Lu, et al., "Massive dirac fermion on the surface of a magnetically doped topological insulator", Science **329**, 659 (2010).

[125] J. Jung, F. Zhang, Z. Qiao, and A. H. MacDonald, "Valley-hall kink and edge states in multilayer graphene", Physical Review B **84**, 075418 (2011).